Vorentwicklung eines unbetätigt geöffneten Ventils für eine Anwendung im Bereich Raumfahrtantriebe

Pre-development of a normally open valve for a space propulsion application

Master thesis work of
cand. aer. Markus Carsten Müller
IRS-20-S-043

Supervisors internal:
Prof. Dr.-Ing. Stefan Schlechtriem
Marius Wilhelm M. Sc.

Supervisors external:
Dipl.-Ing. Stephan Kraus
Pilar Valles M. Sc.

Institute of Space Systems, University of Stuttgart
January 2021

UNIVERSITÄT STUTTGART
INSTITUTE OF SPACE SYSTEMS

Pfaffenwaldring 29 · 70569 Stuttgart · Phone +49 (0) 711 685-62375 · Fax: +49 (0) 711 685-63596 · www.irs.uni-stuttgart.de

Master Thesis Work

of Mr. Markus Müller

Vorentwicklung eines unbetätigt geöffneten Ventils für eine Anwendung im Bereich Raumfahrtantriebe

Pre-development of a normally open valve for a space propulsion application

Motivation:

Ariane Group's competence center for orbital propulsion systems at Lampoldshausen develops, manufactures, tests and integrates orbital propulsion systems and their components. This includes valves for isolation purposes such as opening and closing of fluid circuits for chemical and electrical propulsion systems. Considering the prolongations of space missions' time, current frequently used pyrotechnical valves have some major drawbacks, especially regarding their limited lifetime. The usage of different actuator principles (Bimetallic, shape memory alloys, expandable-materials) which are not or slightly subject to ageing and degradation due to the harsh space environment, constitutes a potential alternative. In the course of this thesis a potential valve design based on the actuation principle of shape memory alloys should be developed and investigated. Key factors to be considered are a cost-efficient production, a lightweight design, the absence of leakage post actuation and reliability.

Task description of the Master thesis work:

- WP1 – Requirements engineering (10%)
  - In the course of familiarization with the subject, a novel assessment of the requirements for a normally open valve shall be conducted. Criterions for verification of the elaborated requirements shall be defined. The valve's sheet of specifications shall be revised.
- WP2 – Modeling and design (20%)
  - Based on an existing first valve design proposal, the valve shall be optimized considering the hydraulic resistance, mechanical strengths and an analysis of internal forces. Requirements developed in the course of WP1 shall be applied here. Analytical or numerical methods shall be utilized if required.
- WP3 – Detailed construction (20%)
  - The best evaluated design from the design study within WP2 shall be implemented in CAD. Associated engineering drawings shall include a detailed analysis of manufacturing tolerances and fittings. A mass analysis and an estimation of manufacturing costs shall be conducted as well.
- WP4 – Investigations on and optimization on the seal (30%)
  - Key element of a normally open valve constitutes its leakage free seal seat. Thus, former experimental investigations on the seal seat shall be continued. Based on experimental results, the seal seat shall be optimized if necessary. As previous tests have demonstrated the insufficiency of the current test jig, a new and optimized jig has to be developed in advance.
- WP5 – Investigations on hydrazine compatibility (10%)
  - As heating a fluid line carrying explosive propellants comes with some risks, a literature research on the compatibility and potential threats shall be conducted. This research shall be accompanied by the analysis of valve activation tests on the normally closed SMA valve conveying hydrazine.
- WP6 – Documentation (10%)
  - The work shall be fully and comprehensibly documented within an internal report. The final master thesis can be derived from this report. All acquired results need to be presented at Ariane Group.

The thesis will be accomplished at Ariane Group GmbH at Lampoldshausen.

Internal supervisor: Marius Wilhelm, M. Sc.
External supervisor: Dipl.-Ing. Stephan Kraus
Starting date: 01.06.2020
Submission until: 01.12.2020

Prof. Dr. S. Schlechtriem
(Responsible Professor)

External Supervisor

Acknowledgement of receipt:
I hereby confirm that I read and understood the task of the master thesis, the juridical regulations as well as the study- and exam regulations.

Signature of the student

Declaration

I, ***Müller, Markus*** hereby certify that I have written this ***Master thesis*** independently with the support of the supervisor, and I did not use any resources apart from those specified. The thesis, or substantial components of it, has not been submitted as part of graded course work at this or any other educational institution.

I also declare that during the preparation of this thesis I have followed the appropriate regulations regarding copyright for the use of external content, according to the rules of good scientific and academic practice[1]. I have included unambiguous references for any external content (such as images, drawings, text passages etc.), and in cases for which approval is required for the use of this material, I have obtained the approval of the owner for the use of this content in my thesis. I am aware that I am responsible in the case of conscious negligence of these responsibilities.

Stuttgart, 10.01.2021 M. Müller

Place, Date, Sign

I hereby agree that my ***Master thesis*** with the following title:

Enter title

is archived and publicly available in the library of the Institute of Space Systems of the University of Stuttgart ***without blocking period*** and that the thesis is available on the website of the institute as well as in the online catalogue of the library of the University of Stuttgart. The latter means that bibliographic data of the thesis (title, author, year of publication, etc.) is permanently and worldwide available.

After finishing the work, I will, for this purpose, deliver a further copy of the thesis along with the examination copy, as well as a digital version.

I transfer the proprietary of these additional copies to the University of Stuttgart. I concede that the thesis and the results generated within the scope of this work can be used free of cost and of temporal and geographical restrictions for the purpose of research and teaching to the institute of Space Systems. If there exist utilization right agreements related to the thesis from the institute or third parties, then these agreements also apply for the results developed in the scope of this thesis.

Stuttgart, 10.01.2021 M. Müller

Place, Date, Sign

[1] Stated in the DFG recommendations for „Assurance of Good Scientific Practice" or in the statute of the University of Stuttgart for „Ensuring the Integrity of Scientific Practice and the Handling of Misconduct in Science"

III. Abstract

Pursuing the objective to fully replace today's state of the art pyrotechnical valves for orbital single shot applications, this thesis subjects the pre-development of a normally open shape memory alloy valve. To obtain a competitive valve, previous concepts as well as the sheet of specifications including all requirements is reassessed and revised.

Based on the revised criteria, a valve's prototype design is elaborated. This design is optimized regarding its pressure drop, its shock load generation upon closing and occurring stress peaks. A hydraulic resistance study is implemented by utilizing computational fluid dynamics and a finite volume method. Fluids under investigation herein are Helium, Xenon and water as a representative for hydrazine. By optimizing the valve's geometry and proposing a parallel valve solution, the pressure drop can be reduced by 18%, respectively by 57% per 150 g/s water. Determining the shock load at closing, an oscillating model of all relevant masses is established. The finally proposed valve design provides a self-induced shock load of less than ¼ of a pyro valve's shock. The correct operating point of the shape memory actuator is ensured by determining the stiffness of relevant components. Results obtained by a finite element calculation are validated by comparing them to former simulations and test results. This way, the elongation at break of the valve's notched tube can be determined.

The valve's internal seal is subject of experimental investigations utilizing a Helium mass spectrometry. Two seal concepts are optimized and four final seal variants are tested eventually. The most promising seal combination consisting of a spherical hard-metal poppet and a soft-metal coated seat provides a gas tight leakage rate at ambient temperature throughout the entire operational pressure domain. Tests at thermal extrema are implemented ensuring the seal's functionality within the qualification temperature range. Investigating the novel requirement of a reverse pressurization case and reducing the effect of O-ring permeation which would falsify measurements, a novel leak testing device is developed and experimentally verified in advance.

Finally, a risk assessment on the operation of a shape memory alloy valve within an environment consisting of liquid and gaseous hydrazine is conducted. Major potential threats during operation are identified and evaluated by an extensive literature research. Accompanied by experimental investigations on the actuation of the normally closed shape memory alloy valve, a final evaluation on the operational hazards is postulated.

IV. Kurzfassung

Mit dem Ziel pyrotechnische Ventile in orbitalen Antriebssystemen zu ersetzen, beschäftigt sich diese Arbeit mit der Vorentwicklung eines einmalig verwendbaren unbetätigt-geöffneten Ventils basierend auf einem Formgedächtnis Aktuator. Um ein konkurrenzfähiges Ventil zu entwickeln, werden zunächst bestehende Konzepte und insbesondere sämtliche Anforderungen an das Ventil überarbeitet und neu bewertet. Dies umfasst sowohl Funktions- und Leistungsparameter wie auch Testprozeduren.

Basierend auf diesen Anforderungen wird ein Prototyp Ventil entwickelt, dessen Geometrie hinsichtlich des Druckverlustes, den selbst-induzierten Schocklasten sowie Spannungsspitzen optimiert ist. Die Parameterstudie zur Druckverlustoptimierung mittels numerischer Simulation basierend auf der Finiten Volumen Methode wird dabei für die Arbeitsmedien Helium, Xenon sowie Wasser durchgeführt. Die Ähnlichkeit von Wasser zu Hydrazin wird nachgewiesen. Durch entsprechende Optimierungen und eine vorgeschlagene Parallel-Ventil-Lösung kann der Druckverlust für 150 g/s Wasser um 18%, bzw. um 57% reduziert werden. Die auftretenden Schock Lasten bei der Schließung des Ventils werden analytisch durch ein geeignetes Schwingungsmodell ermittelt, bewertet und optimiert. Der maximale Schock verursacht durch die vorgespannte Druckfeder sowie den Riss des Kerbrohrs resultiert zu weniger als ¼ eines Pyroventil Schocks. Der korrekte Arbeitspunkt des Formgedächtnis Aktuators wird validiert, indem die Steifigkeit relevanter Komponenten mittels Simulationen basierend auf der Finiten Elementen Methode bestimmt und evaluiert wird. Auf diese Weise kann die Dehnung bei Riss des Kerbrohrs bestimmt werden.

Die interne Dichtung bestehend aus Dichtsitz und Stempel ist Gegenstand von experimentellen Untersuchungen mittels Helium-Massenspektrometrie. Hierbei werden zwei verschiedene Dichtungskonzepte hinsichtlich der Leckagerate und Dichtkraft optimiert und schließlich 4 Varianten untersucht. Die vielversprechendste Variante, bestehend aus einem kugelförmigen Metall-Stempel und Weichmetall-beschichtetem Dichtsitz, bietet bei Raumtemperatur eine gasdichte Leckagerate. Tests unter thermischen Extrembedingungen sowie bei einer Rückwärtsbedrückung werden ebenfalls durchgeführt. Zur Umsetzung neuer Anforderungskriterien und zur Reduzierung von Messungenauigkeiten, wird eine neue Test Apparatur entwickelt und in Betrieb genommen.

Abschließend wird eine Risikobewertung hinsichtlich des Betriebs von beheizt aktivierten Ventilen in Hydrazin führenden Treibstoffleitungen durchgeführt. Potentielle Risiken werden identifiziert und bewertet. Begleitet und validiert werden die gefundenen Ergebnisse durch Aktivierungstests des unbetätigt-geschlossenen Formgedächtnis-Ventils. Die Übertragbarkeit der Risikobewertung für das unbetätigt-geöffnete Ventil wird abschließend geprüft und postuliert.

V. Table of contents

VI. List of figures

VII. List of tables

VIII. List of symbols

Latin symbol	Description	Dimension
a	Acceleration	$L \cdot T^{-2}$
$\hat{A}$	Amplitude	L
A	Area	L^2
c_F	Thrust coefficient	-
d	Diameter	L
e	Inner energy	$M \cdot L^{-1} \cdot T^{-2}$
E	Energy	$M \cdot L^2 \cdot T^{-2}$
F	Force	$M \cdot L \cdot T^{-2}$
$\underline{F^C}$	Convective flux vector (2D – case)	$[ML^{-2}T^{-1}\ ML^{-1}T^{-2}\ ML^{-1}T^{-2}\ MT^{-3}]^T$
$\underline{F^D}$	Viscose flux vector (2D – case)	$[-\ ML^{-1}T^{-2}\ ML^{-1}T^{-2}\ MT^{-3}]^T$
G	Shear modulus	$M \cdot L^{-1} \cdot T^{-2}$
i_{eff}	Number of effective windings	-
k	Turbulent energy (chapter 4.1)	$L^2 \cdot T^{-2}$
k	Spring stiffness (chapter 4.2)	$M \cdot T^{-2}$
k	Component stiffness (chapter 4.3)	$M \cdot T^{-2}$
l	Length	L
m	Mass	M
$\dot{m}$	Mass flow rate	$M \cdot T^{-1}$
M	Momentum	$M \cdot L \cdot T^{-1}$
Ma	Mach number	-
n	Number	-
p	Pressure	$M \cdot L^{-1} \cdot T^{-2}$
P	Pitch	M
q	Thermal conduction	$M \cdot T^{-3}$
r	Radius	M
R_a	Arithmetic average of roughness profile	L
Re	Reynold's number	-
R_m	Tensile strength	$M \cdot L^{-1} \cdot T^{-2}$
$R_{p0.2}$	Yield strength	$M \cdot L^{-1} \cdot T^{-2}$
R_s	Specific gas constant	$L^2 \cdot T^{-2} \cdot \Theta^{-1}$
s	Line course	L
S	Shock load	$L \cdot T^{-2}$
t	Time	T
T	Temperature	Θ
$\underline{U}$	Fluid state vector (2D – case)	$[ML^{-3}\ ML^2T^{-1}\ ML^2T^{-1}\ ML^{-1}T^{-2}]^T$
v	Velocity	$L \cdot T^{-1}$
w	Width	L
W	Work	$M \cdot L^2 \cdot T^{-2}$
W_{polar}	Polar section modulus	L^3
x	X-direction (chapter 4)	L
x	Substitution parameter (chapter 5)	-
x	Mass fraction (chapter 6)	-

Greek symbol	Description	Dimension
α	Angle	-
γ	Isentropic exponent	-
δ	Layer thickness	L
Δ	Change between two states	-
ε	Turbulent dissipation rate	$L^2 \cdot T^{-3}$
η	Dynamic viscosity	$M \cdot L^{-1} \cdot T^{-1}$
λ	Darcy friction factor	-
μ	Safety factor	-
ρ	Density	$M \cdot L^{-3}$
σ	Stress	$M \cdot L^{-1} \cdot T^{-2}$
τ	Shear stress	$M \cdot L^{-1} \cdot T^{-2}$
ϕ	Phase shift	-
Φ	Leakage rate	$M \cdot L^2 \cdot T^{-3}$
ω	Oscillating frequency	T^{-1}
$\widetilde{\omega}$	Specified oscillating frequency	T^{-1}

Index	Description
A	Axial direction
Act	Actuator
b	Block
B	Bushing
c	Combustion chamber
crit	Critical
eff	Effective
g	Gaseous state
GHe	Gaseous Helium
GXe	Gaseous Xenon
H	Hydraulic
i	Inner
I/F	Interface
k	Spring
kin	Kinetic
m	Mass
M	Mandrel
n	Nominal
N	Normal direction
l	Liquid state
r	Compressive
s	Sealing
t	Time
T	Torsion
o	Outer
Op	Operating
p	Pressure
P	Poppet
pot	Potential
Q	Qualification
r	Compressive
req	Requirement
rev	Reverse pressurization case
rupt	Average point of rupture
w	Wire
x	X-direction
y	Y-direction
ϕ	Tensile
0	Unloaded condition
1	Spring number 1 of spring trade-off
II.B	Material II.B
′	Iterated value
*	Throat
∞	Free jet condition

IX. Abbreviations

Abbreviation	Description
(A)	Actuation
AIAA	American Institute of Aeronautics and Astronautics
AOCS	Attitude and orbit control system
AWG	American wire gauge
CFD	Computational fluid dynamics
C-J	Chapman-Jouget
ECSS	European cooperation for space standardization
EoL	End of life
ESA	European Space Agency
FEM	Finite element method
GHe	Gaseous Helium
HV	High vacuum
I/F	Interface
L	Lot
LAM	Liquid apogee motor
MEOP	Maximum expected operating pressure
MEROP	Maximum expected reverse operating pressure
MMH	Monomethyl hydrazine
MON	Mixed oxides of Nitrogen
NASA	National Aeronautics and Space Administration
NC	Normally closed
NO	Normally open
NTO	Dinitrogen tetroxide
OHFC	Oxygen free high thermal conductivity
OP	Operating temperature
(PA)	Post actuation
PV	Pyrotechnical valve
QT	Qualification temperature
RTD	Resistance temperature detector
SMA	Shape memory alloy
SMAV	Shape memory alloy valve
SME	Shape memory effect
SN	Serial number
SWACER	Shock wave amplification of coherent energy release
Ti	Titanium
TRL	Technology readiness level
UHV	Ultra-high vacuum
WSTF	White Sands Test Facility

1. Introduction

Valves are one of the most crucial components of today's electrical and chemical propulsion subsystems for spacecraft. They are one of the actively controlled components for initializing orbital maneuvers. A broad range of variants for different application purposes exist today. Examples of those objectives are such as the control of the mass flow rate of propellants, the isolation of fluid circuits or the fill and drain of propellants and pressurant [1]. All these valves distinguish primarily in terms of their actuation and functional principals, as well as their reusability and complexity. Currently, valves driven by an explosive event caused by firing a pyrotechnical squib are the most common valves for single use applications. Other than flow control valves, single use valves are used to entirely open or close fluid circuits of the feed line system. A possible mission scenario for a normally closed (NC) valve is the passivation of satellites after their end of life (EoL). Respectively, a normally open (NO) valve is used for example to isolate the liquid apogee motor (LAM) after its burn out.

Since the beginning of aerospace, pyrotechnical valves (PV) established for most single-shot applications as they provide a very high reliability and excellent leak tightness accompanied by low complexity [1]. A picture of a PV by Ariane Group can be seen in figure 1. Besides the stated advantages of PVs, they also have some major drawbacks:

Complex electronics and software

To enable precise and safe actuation and to prevent unintended actuation of a PV, complex onboard controlling electronics such as a pyro driver are necessary. These costs exceed the expenditure on the actual hardware valve by orders of magnitude.

Legal restrictions

By nature, pyrotechnical charges come with high hazards, especially for human life during testing, production and integration. Therefore, the ground handling of PVs underlie high safety regulations and legal constrains. E.g., the authorization of handling explosives is always reserved to certified specialists. This has a strong impact on supply chains, development processes and component integrations. While increasing the costs drastically, it reduces the flexibility [2].

Shocks and water hammers

After actuation a PV responses within a fraction of a second (≤ 7 ms) [1][3]. Utilizing the high energy discharge the fluid circuit gets closed by cold welding the driven wedge with the feed line tubes or respectively opened by rupturing a blocking element out of the flow path. Both events generate high shock loads up to 6200 g [1][3] on the propulsion system, the entire satellite and its fragile payloads. Considering the worst case scenario, this may also result in inaccuracies of navigation and AOCS (Attitude and Orbit Control) systems and lead to entire mission failures. Furthermore, the rapid actuation of PVs can generate a critical water hammer on components both upstream and downstream the feed line [2].

Figure 1: Ariane Group's pyrotechnical isolation valve [1]

Limited lifetime

A further major drawback of PVs is the limited lifetime of the pyrotechnical squib between 6 to 8 years [3]. The stabilizer of the explosive underlies severe ageing and degradation effects, especially in a harsh space environment. This especially gains importance considering longer lifetimes of state of the art spacecraft than decades ago. Regarding

valve storage, long duration and interplanetary missions and furthermore the European Space Agency's (ESA) clean space initiative on space debris mitigation from 2011 this holds true especially. The functionality of propulsion system components after decades in orbit to perform a final disposal or passivation maneuver has become a driving key factor today [4].

Explosive events and adiabatic compression

Firing an explosive charge just next to a feed line conveying high explosive liquids and vapor implies an inherent risk. If hot gases from the explosion blow by the membrane which is supposed to separate the PV's combustion chamber from the working fluids, fatal and satellite destructive events can occur. This failure mode has been identified in the past for some mission losses such as Mars Observer, Landsat 6 or Telstar 402 [5][6]. Even if no combustion gases get in direct contact with the working media, the fast opening or closing of valves can initiate an explosive detonation of hydrazine vapor due to rapid adiabatic compression [5][6][7].

To overcome all these drawbacks, Ariane Group at its site for orbital propulsion systems at Lampoldshausen has successfully developed a NC valve based on a different actuation principal, the shape memory effect (SME). This effect is a characteristic material property of some Nickel (Ni) and Titanium (Ti) based metal alloys, so-called shape memory alloys (SMA) and can be utilized by simply heating it until a certain transformation temperature. This technology enables the usage of single shot valves without any stored and rapid released chemical energy. While reducing the resulting shock at actuation drastically, all before mentioned hazards of PV aboard spacecraft and on ground can be eliminated. Furthermore, such SMA actuators have a nearly unlimited lifetime and don't underlie ageing and degradation effects, neither during storage nor due to space environments. All these aspects lead to the high potential of SMA valves to replace all PVs for orbital propulsion purposes in the future. The first flight NC SMAV (SMA valve) is already integrated into the propulsion system of the Heinrich Hertz communication satellite which will be launched in 2021 with the Ariane 5. The valve will serve to passivate the satellite's bi-propellant propulsion system after its EoL [1]. Figure 2 shows the NC SMAV.

Pursuing the aim to fully replace all PVs on spacecraft, the pre-development phase of the NC SMAV's counterpart, the NO SMAV is currently ongoing at Ariane Group and is the objective of this work. The NO variant faces some additional challenges, as to seal the fluid path by creating a so-called zero-leakage material closure without the use of high chemical energy.

Within previous students' works at Ariane Group, already a first proposal of the valve's design exists. The current state of development, as well as its corresponding working principles are summarized and outlined in the beginning of this thesis.

Figure 2: Ariane Group's NC SMA isolation valve [1]

To ensure the development of a competitive valve, one of the objectives of this thesis is to elaborate a novel sheet of specifications. Therefore, a pre-existing version of this specification based on the NC SMAV is fully revised and adapted to the NO variant. This especially comprises likewise performance and safety issues, as well as the definition of test procedures for a successful and reliable qualification campaign. These acquired criteria constitute the basis of all further investigations of the NO valve.

After defining these boundary conditions, the development of a prototype valve is aspired. This includes two major aspects. Firstly, the existing valve's design proposal is analyzed in greater

detail, evaluated and optimized regarding its overall feasibility, functionality and performance parameter. To meet all defined requirements, extensive investigations utilizing analytical and numerical methods are conducted to present a prototype valve eventually. The second aspect which is focused on within this thesis is the experimental investigation on and optimization of the valve's seal. These investigations mainly comprise the determination of leakage rates throughout the valve's entire pressure and temperature domain. Due to the revised specifications, a novel aperture enabling these investigations is developed too.

As outlined above, the safe operation of a valve within an environment consisting of explosive propellants constitutes a challenging key factor. Therefore, a risk study is conducted on the compatibility of the valve with liquid and gaseous phase hydrazine. In order to gain reliable and far-reaching results, an extensive literature research on the topic is sustained by actuation tests of the NO valve's counterpart, the NC SMAV. These tests are conducted within a hydrazine environment and determine the risks of explosive threats due the operation of a SMAV.

2. Functional principles and state of development

After outlining the motivation and contents of this thesis within the introduction, this chapter now aims to give a brief overview on the functional principles of the NO SMAV. Additionally, a summary on the development progress elaborated within previous theses is presented. The outlined principles constitute the basis of this work.

2.1 Shape memory effect

By providing the potential to work as a solid state actuator with the absence of stored chemical energy, shape memory actuators have gained importance in the aerospace and automotive industries within the past years. A shape memory alloy can be characterized by the phenomenon of the material's ability to recover its original shape upon heating after a previous mechanical deforming. This behavior can be utilized as the material is able to perform this transformation against a certain force [8]. The process bases on the reversible transformation of the crystalline structure of certain materials. One common material, which provides this transformation behavior is the alloy of Nickel and Titanium. Popularly, this material is referred to as NiTiNol.

The following two figures 3 and 4 illustrate the principle of the SME. At room temperature the material provides a crystalline structure of twinned martensite (A). This martensitic structure comprises out of multiple twin related lattice correspondence variants (red and blue). By applying external stress onto the metallic structure, the twinned martensite detwinns and reorientates. The novel formed martensite provides a single lattice correspondence variant and results in a macroscopic form change (B). If the former loaded stress now is unloaded, the deformation remains (C) [8]. This process (A) to (C) especially describes the compressing treatment of the SMAV's actuator in advance of implementation. As shown in both figures, the detwinned martensite now is capable to transform into an austenitic structure under the influence of heat. Macroscopically considered, this austenite provides the same form as the twinned martensite, hence the original shape is restored. According to the Clausius-Clapeyron relationship, the so-called transformation temperature, or more detailed the *austenite finish temperature*, need to be reached to enable this process. When the temperature decreases again and eventually reached the *martensite finish temperature*, it can be seen, that the austenitic structure again changes into its original twinned martensite structure (E) and the entire process could be repeated again [8]. This process (A) to (E) constitutes the so-called one-way shape memory effect which is utilized by the Ariane Group's SMAVs.

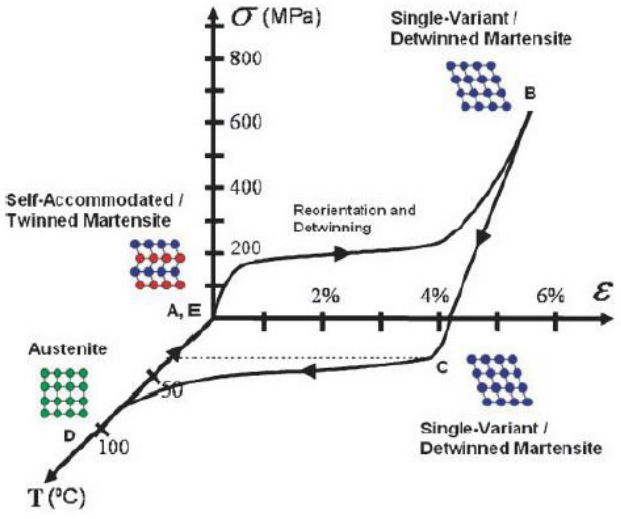

Figure 3: One-way shape memory effect [8]

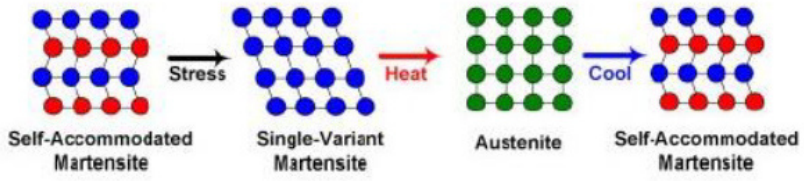

Figure 4: Crystal structures occurring during the phase transformations of SMAs [8]

2.2 Valve concept

In the course of previous theses, students at Ariane Group have already conducted investigations on the design of the SMA NO valve. The general concept bases on the principle of an expanding SMA actuator breaking a notched tube. By breaking this tube purposely, a preloaded spring is intended to close the seal of the valve. Lux [9] therefore performed a design study of the notched tube, mainly based on criteria as complexity, costs, hydraulic resistance and installable spring volume. Concluding his thesis, he proposed the following prototype design seen and marked in figure 5:

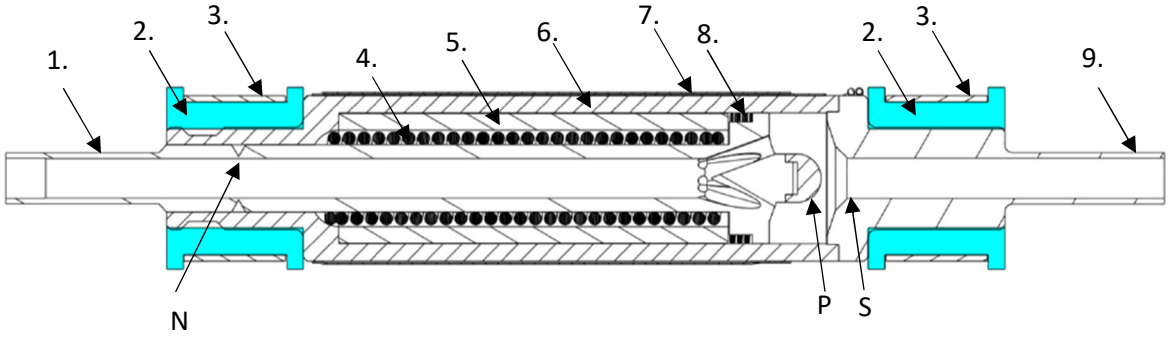

Figure 5: NO SMAV prototype design by Lux [9]

As indicated in the figure, the valve consists of 9 different components, no. 2 and 3 twice. The actuation principle of the valve is adopted from the NC SMAV. The actuator 5 gets heated by the electrical heater 7 until the transformation temperature is reached. The abrupt expansion of the actuator pushes against the front housing 6 and the flange of the notched tube 1. As the housing is fixated with the clamps 3 and elastomeric inserts 2, the notched tube is forced to expand too. Thereby, the notch N gets ruptured purposely. The compressed and preloaded spring 4 now pushes the broken part of the notched tube, including the poppet P into the seal seat S. The seat is integrated into the rear and smaller housing 9. Component 8 is proposed as a PTFE ring to feature an improved glide behavior.

2.3 Sealing principle

Similar to Lux' valve design study, Radermacher [10] and Wollner [11] conducted assessments and experimental investigations on various concepts on the NO seal. Out of a wide variety of possible sealing solutions, soon a mechanism of closing a poppet onto a seat was evaluated the most suitable option for the SMA valve. This decision is mainly based on aspects as manufacturability, simplicity and potential sealing capability. A seal consisting of a poppet and a seat still provides an enormous number of possible designs and material combinations, each with its very respective advantageous and disadvantageous. During the development process soon complex geometries like a labyrinth sealing solution as shown in figure 6 have been rejected. Those concepts with flexible lips could cause contamination of the working fluids due to scraped material particles.

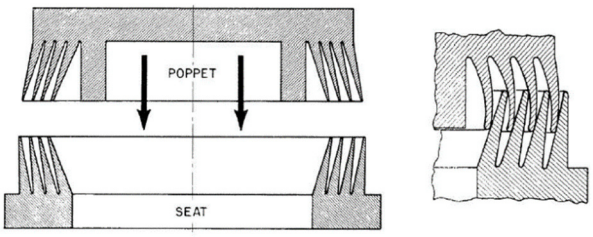

Figure 6: Labyrinth sealing [12]

The development focused on simple geometries like ball valves, conical plugs or disks with knife edges. Examples of those concepts are presented in figure 7 a.) – c.). One special variant of a ball valve constitutes the Tri-Point seat – see figure 8. This seat consists of two spherical surfaces with different diameters. The upper sphere's diameter is about 20-30 % larger than the lower sphere's diameter. Closing down a spherical poppet with a diameter between those spheres, a perfectly circular sealing line results. According to literature this seal provides an excellent sealing capability [13]. However, the spherical surface areas and its corresponding tight tolerances increase the manufacturing effort and consequently the costs extensively. Hence, a concept trade off led to the focus mainly on ball and conical poppets [10]. Disk poppets with a knife edge seat have also been investigated but rejected due to insufficient leakage results [11].

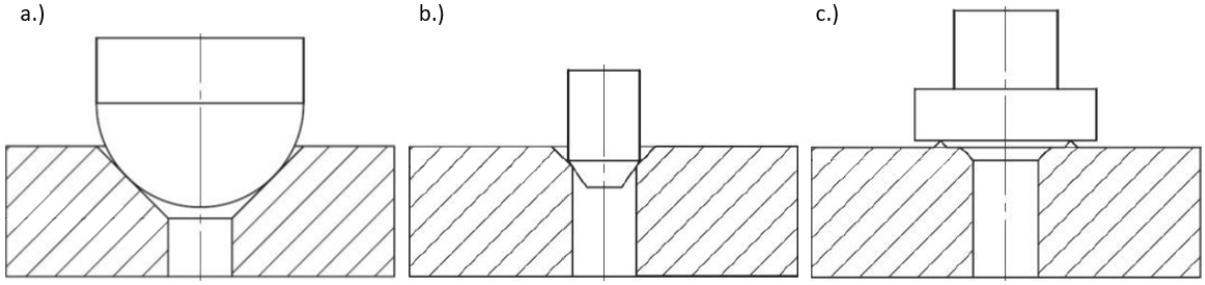

Figure 7: Seals consisting of poppet and seat: a.) Ball poppet; b.) Conical plug poppet; c.) Disk poppet with knife edge seat [11]

After identifying spherical and conical poppet geometries as the most promising option for the SMA valve, the question about the materials to use is not fully answered yet. A seal consisting of a poppet and a seat always requires two different materials for these components. The principle to close the fluid path mainly bases on creating a leak tight form closure by the plastic deformation of either the poppet or the seat by pressing it onto the other with a certain force. To reach sufficient leakage rates, this requires one material to be softer than the other. "Softer" specifies, that one material should provide a lower yield strength, which constitutes the threshold value for a plastic deformation, than the other material. Considering this, combinations of soft elastomeric materials with hard metals are very common. However, a combination of one soft and one hard metal states also conceivable.

Based on a media compatibility research, previous investigations have eventually led to three material combinations. The first combination is presented in figure 9. This seal consists of a conical metal poppet and a metal seat, but integrates a PTFE ring (grey). The softer PTFE material is supposed to provide a high sealing capability at comparable low sealing forces. However, tests have shown, that the intended sealing lip largely deforms under high pressures and even tends to shear off entirely. This would result in a critical failure of the seal. Furthermore, elastomeric materials are subject of diffusion processes when they are exposed to gas at high pressures. This so-called permeation behavior is further discussed within chapter 5.2.1. Considering these aspects, this variant has finally been rejected too [10].

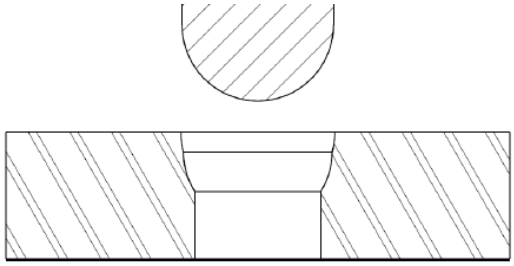

Figure 8: Tri-Point seal seat and spherical poppet [9]

The two other concepts of the identified three variants provide a metal-metal solution and geometrical equality. Their shapes are similar to ball valves but further modified to create a narrower sealing line at the inner edge of the seat. This way a circular sealing line similar to the Tri-Point seat results. These variants have demonstrated the most promising results so far. That is why, these seals are subject of the investigations and optimizations in the course of this thesis. Both variants are depicted and described in greater detail within section 5.1.

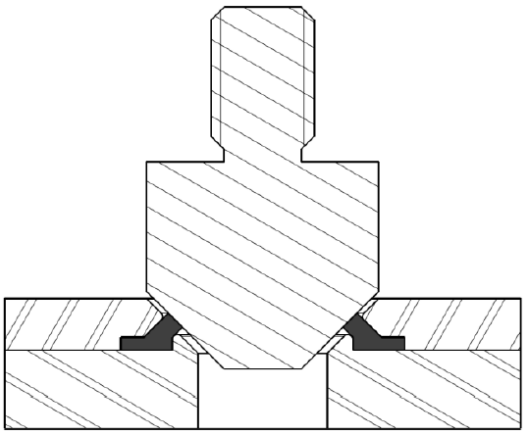

Figure 9: Conical plug seal with PTFE lip [10]

3. Requirements engineering

In advance to a further development of the valve and its seal, it is useful to define all requirements the final valve should meet. One of the valve's major requirements is the similarity in design and functional principle to its related NC counterpart. As the NC version already passed a full qualification campaign, a great share of time and cost can be spared during the development process of the NO valve. This is intended to be achieved by utilizing great commonality between the analogs. In detail the features which are decided to be adopted from the NC variant and the resulting advantageous are stated in the following table 1.

Table 1: Geometric similarity between NC SMAV and NO SMAV – derived from [14]

Geometric commonality	Affected parts	Benefits
Mounting interface	Mounting brackets Elastomeric inserts	Enables the use of the same mounting procedures and interfaces
Notch – Actuator combination	Notched tube Actuator Heater	Using the same geometry of the notch accompanied with the same actuator, no expensive mechanical validation on the actuator's ability to rupture the notch is necessary. Same actuator enables use of same heater
Weld seams and position	Notched tube Housing	Applying the same weld geometry and positions, no expensive weld seam qualification is required. Furthermore, weld parameters and weld jig from the NC variant can be used and are not needed to be redeveloped
Outside diameter	Housing Heater circuitry Thermal indicator	By maintaining the outside geometry of the NC valve, equivalent thermal sensors, as well as the heater can be used

As the NC and NO variants demonstrate such great commonality and operate under similar conditions, the first proposal for the NO specification sheet was derived from the NC specification. In a further step, this specification was subject of a novel assessment and fully revised. In the following, some of the newly developed requirements are stated, selected by consideration of relevance for this thesis.

3.1 Functional and performance requirements

3.1.1 Fluids and media compatibility

In a first step, it is necessary to define all fluids and gases which should be compatible with the valve, its single components and materials. The definition of a material's compatibility is standardized by the ECSS (European Cooperation for Space Standardization). This sheet defines the compatibility as the "absence of unacceptable performance or reliability loss due to chemical reactions and physical changes in material or substances during the compatibility life" [15]. Furthermore, a media compatibility includes the compatibility to the valve's working principle, thus the ability of the SMA actuator and its heater to operate reliably without creating threats by heating or shocking explosive propellants. Table 2 provides an overview over all fluids and gases relevant for the valve's operation and testing procedures. Considering the results from the literature research on hydrazine compatibility stated in chapter 6, the inclusion of the vapor phases of oxidizers and fuels constitutes one important adaption of this table.

3.1.2 Temperature domain

One important key requirement of the valve is the assurance of reliable operation within a certain worst case temperature domain. This temperature domain varies with the valve's application case, whether it is used for inert gas or liquid propellant application. Therefore, the operating range of those two cases is distinguished:

- Operating temperature domain for liquid propellant application: $T_{Op,l,min}$ & $T_{Op,l,max}$
- Operating temperature domain for inert gas application: $T_{Op,g,min}$ & $T_{Op,g,max}$

An operating temperature domain constitutes the range within the valve should be able to be activated and to close the flow path leakage free. The stated temperatures are derived from specifications on propulsion subsystem level for usual temperature domains within a thermally controlled environment onboard a satellite. However, for qualification of the valve, a broader temperature range including a certain margin needs to be applied. This way, the following qualification temperatures are defined:

- Qualification temperature domain for liquid propellant application: $T_{Q,l,min}$ & $T_{Q,l,max}$
- Qualification temperature domain for inert gas application: $T_{Q,g,min}$ & $T_{Q,g,max}$

The qualification temperature domain for inert gas application is identified as worst case domain ($T_{Q,g,min} < T_{Q,l,min}$ & $T_{Q,g,max} > T_{Q,l,max}$) and thus applied for all following investigations. Within this temperature range, no unintended actuation at the maximum temperature or respectively the ability for actuation at minimum temperature must be ensured.

3.1.3 Pressure domain

Besides the temperature domain, another important environmental parameter is the pressure at which the valve must be able to operate adequately. Within this domain, the valve must fulfil its intended purpose of closing the flow circuit reliably, as well as no tension driven damage, e.g. a permanent deformation or rupture, should occur. The maximum operating pressure for space propulsion systems occurs at the pressurization of propellants using non-liquefiable inert gases such as Helium. Thus, for Ariane Group's propulsion systems, the maximum expected operating pressure (MEOP) in flow direction is defined accordingly.

As firstly stated by Radermacher [10] and now concretized internally at Ariane Group, an additional pressurization case has to be considered. With the valve integrated between a Helium pressurization system and the propellant system, a venting of the Helium tank for passivation at the satellite's EoL could result in a pressure gradient against the nominal flow direction, if the propellant tank is not vented beforehand. As this scenario would generate a pressure gradient between the nominal pressure of a propellant tank and the vacuum of space, a maximum expected reverse operating pressure (MEROP) against flow direction is specified.

Table 2: Media compatibility

Substance	Application
MMH (liquid & vapor)	Bipropellant
NTO (liquid & vapor)	Bipropellant
Hydrazine (liquid & vapor)	Monopropellant
Helium	Pressurization, Test
Deionized water	Water propulsion
Xenon	Electrical propulsion
Krypton	Electrical propulsion
Nitrogen	Test
Argon	Test
HFE 7100	Test, cleaning
Isopropyl alcohol	Test, cleaning

3.1.4 Internal forward leakage rate

As stated at the introduction, one of the major characteristics of the newly developed SMA NO valve shall be the so-called "zero-leakage" at its activated state. This zero leakage needs to be specified clearly and related to a measureable threshold value. As previous leakage rate measurements conducted by Radermacher have proven a tough challenge to reach a constant low leakage rate of the seal over the entire qualification temperature range from 3.1.2, this requirement is reconsidered. Within the frame of this work, it was decided that there is no need to demand a constant low leakage rate over the qualification temperature range, as a satellite is always thermally controlled. Only if the thermal control system fails its task, the satellite's temperatures would exceed the above stated operating temperatures. As this case however, constitutes a mission critical malfunction of the satellite, either its functionality needs to be restored immediately or the satellite has to be passivated. Thus, a slightly increased leakage rate outside the operating temperature domain would not represent a critical system threat. Therefore, a temperature dependent internal leakage rate is defined and can be seen in figure 10. The figure shows that within the operational temperature range for liquid propellant applications, hence under nominal conditions the valve's allowable leakage rate is restricted to be less than $\Phi_{req,Op}$. Outside this range within the qualification domain, a slightly higher leakage rate $\Phi_{req,Q}$. is acceptable. Worth mentioning, this leakage rate profile is applicable throughout the entire defined pressure domain, but only for liquid propulsion applications. For inert gas applications a similar profile (blue graph) applies considering the larger operational and qualification temperature domain as stated above.

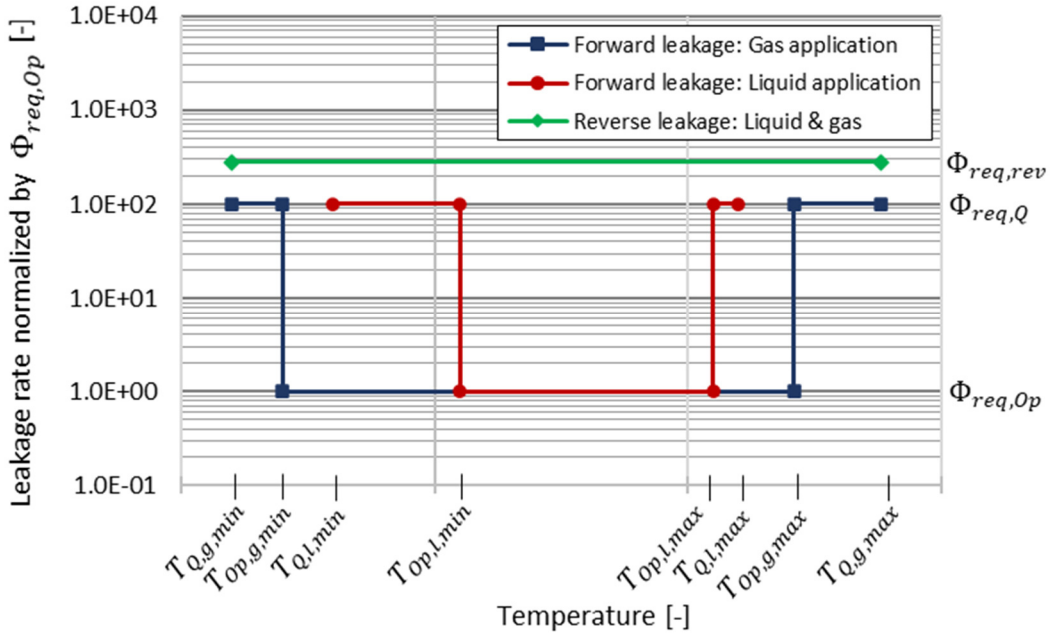

Figure 10: Leakage rate requirement over temperature domain

3.1.5 Internal reverse leakage rate

The novel requirement of the valve's functionality at a pressurization reverse to the nominal flow direction as described under 3.1.3 demands an additional definition of an acceptable leakage rate for this case. An evident definition for this leakage rate is the same leakage rate as for commonly used check valves. These valves specify an internal reverse leakage rate requirement which value constitutes the experimentally determined threshold value for liquid leak tightness: $\Phi_{req,rev}$. This value particularly constitutes the experimentally determined threshold value for liquid leak tightness. Hence, the NO SMAV should provide a leakage rate of less than $\Phi_{req,rev}$ GHe throughout the reverse pressure domain up to a differential pressure of MEROP. This should be applicable at all temperatures within the qualification temperature range. The reverse leakage rate is illustrated by the green graph in the figure 10 above.

3.1.6 Pressure drop

One of the potential application cases of the NO valve is the isolation of the LAM after its burnout. During the orbital transfer by firing the LAM, mission dependent around 70% of the propellant mass onboard the satellite is burned [16]. Thus, this maneuver constitutes the maneuver with the highest propellant mass consumption. This again, results in a great importance of the performance parameters of the LAM itself and its connected feed system. The thrust F of a chemical engine is directly proportional to its combustion chamber pressure p_c:

$$F = c_F \cdot p_c \cdot A_* \tag{3.1}$$

A_* constitutes the nozzle throat cross section area, c_F is the thrust coefficient. The combustion chamber pressure again result directly from the tank pressure reduced by the sum of the pressure drops over all components of the feed and injection system. This exemplifies the importance of a low hydraulic resistance of each component of the feed system, thus of the SMA NO valve as well.

To define a maximum acceptable pressure drop for the SMA NO valve, three application cases have to be distinguished. As listed in table 3, the inert gas application is represented by stating a pressure drop for a mass flow rate of 0.6 g/s gaseous Helium. Likewise, the Ariane Group's electrical propulsion applications are represented by a defined mass flow of 0.0012 g/s gaseous Xenon. To represent the chemical liquid propulsion applications, it is common to use water as a well investigated representative fluid. Water and e.g. Hydrazine have quite similar physical properties which enables a comparison of their dynamic flow behavior. Characterizing a flow through a pipe, the Reynolds number constitutes an important non-dimensional parameter to prove flow similarity. With the properties of Water at 20 °C and 1 bar [17]:

$$\begin{aligned} \rho_{Water} &= 998.2\ \frac{kg}{dm^3} \\ \eta_{Water} &= 1.001\ mPa \cdot s \end{aligned} \tag{3.2}$$

And the analog properties of pure hydrazine [18]:

$$\begin{aligned} \rho_{Hydrazine} &= 1008.5\ \frac{kg}{dm^3} \\ \eta_{Hydrazine} &= 0.9736\ mPa \cdot s \end{aligned} \tag{3.3}$$

The ratio of Reynolds numbers for a certain geometry and velocity follows:

$$\frac{Re_{Water}}{Re_{Hydrazine}} = \frac{\rho_{Water} \cdot \eta_{Hydrazine}}{\rho_{Hydrazine} \cdot \eta_{Water}} = 0.963 \tag{3.4}$$

The Reynolds similarity proves the applicability of water instead of hydrazine for further pressure drop considerations.

Table 3: Pressure drop requirement

Media	Mass flow rate [g/s]	Maximal pressure drop [-]	Condition
Gaseous Helium	0.6	$\Delta p_{GHe,req}$	• 20 ± 3°C • MEOP at inlet
Gaseous Xenon	0.0012	$\Delta p_{GXe,req}$	• 20 ± 3°C • 150 bar at inlet
Liquid water	150	$\Delta p_{water,req}$	• 20 ± 3°C • Ambient pressure at outlet

According to table 3, the highest mass flow rate occurs for liquid propellant. The allowable pressure drops can be ordered as follows: $\Delta p_{water,req} > \Delta p_{GHe,req} > \Delta p_{GXe,req}$. The corresponding maximal allowable pressure drop $\Delta p_{water,req}$ results from a comparison to the ¼" NO PV. If the performance parameters of the NO SMAV would not meet the performance parameters of the analog NO PV, this would probably outweigh the other remaining advantageous of the SMA valve. Thus, a design iteration to match these parameters is conducted later within this thesis at chapter 4.1.

3.1.7 Shock load generation

As described within the introduction of this thesis, one drawback of PVs is the high shock load they generate by abruptly closing the flow path within milliseconds. The SMA valve is not based on an actuation by a pyrotechnical squib and thus generates a lower shock, but rupturing the notch and releasing the energy stored by the preloaded spring generates a shock onto in the SMA valve, which is transported to the valve's mounting and tubing connection interfaces. Further, the impact of the poppet onto the seal seat creates another shock peak just milliseconds after the notch rupture. To relate this behavior to a measurable value, a comparison with the shock loads generated by PVs and especially the already qualified NC SMAV is conducted. An experimental investigation on the shock loads at opening the NC SMAV is therefore conducted within chapter 6.2 in further detail. Herein, the acceptable shock loads created by the NO SMAV are defined as $S_{req,valve}$ less than half of the PVs measured at the valve itself and $S_{req,I/F}$ measured at the valve's mechanical interfaces.

These maximum values are valid throughout the entire pressure domain from ambient to MEOP. This is important especially for the NC SMA valve, as the applied pressure gradient between inlet and outlet at closed state causes an additional shock load at opening. As for the NO valve no pressure gradient between inlet and outlet is applied prior to closing, its importance for shock load generation decreases, but is still needed to be considered.

At the detailed calculation of spring forces and poppet accelerations at chapter 4.2, it will be seen, that this shock requirement results in a further restriction of a maximal sealing force.

3.2 Test methods

In the course of revising the specification sheet, various test procedures for the NO SMAV have been reworked or added e.g., the burst pressure test or the vibration test. However, considering the relevance for this thesis, only two leakage tests are presented herein. As a proof of concept, those methods are applied for conducting the investigations on the leakage capability of the valve's internal seal as further described in chapter 5.

3.2.1 Internal leakage test

Considering the new requirements of reverse pressurization and the definition of a reverse leakage rate, an appropriate test procedure for later qualification and acceptance tests has to be defined. Therefore, the internal leakage test is divided into different pressurization cases as shown in the following table 4. Previous tests by Radermacher [10] have shown, that the highest leakage rate does not always occur at the maximum operating pressure MEOP, but at lower pressures at which the effect of higher diffusion at higher pressures dominates the additional closing force provided by the applied pressure. This is the reason, that during the leakage test, the pressure level with the resulting highest leakage rate has to be determined and subsequently tested. The three described pressurization cases can be seen in the following table. The stated test durations are defined according to ECSS standards, see [19].

Table 4: Pressure levels during qualification and acceptance tests on internal leakage

Parameter	Qualification test	Acceptance test
Duration at defined pressure level	30 min	5 min
Internal pressure levels	MEOP at inlet port	
	Level with highest leakage rate	
	MEROP at outlet port	

3.2.2 Thermal cycling sealing performance test

During its lifecycle a satellite and all its components undergo many phases of different environmental conditions, especially numerous temperature cycles as e.g., at entrance and exit of orbital eclipse phases. The functionality of all components must be guaranteed for all these cycles. Therefore, a component specific test profile also used for the NC variant of the SMAV should be applied to all NO valves post actuation during the qualification campaign. This profile constitutes out of 12 full thermal cycles as indicated in figure 11. During the first cycle the maximum and minimum qualification temperatures from 3.1.2 shall be applied. Afterwards, the remaining 11 cycles can be tested at the minimum and maximum operating temperatures. To be noted, that a maximum temperature gradient of 5 K/min shall not be exceeded (nominal: 2 K/min) and a dwell time of ≥ 2 hours has to be complied. The red rhombs in figure 11 indicate the points for leakage rate measurements. Respectively two measurements shall be conducted during the first the 12th cycle. Furthermore, two measurements at ambient temperature, one measurement prior and one measurement post the thermal cycling shall prove the full and not influenced functionality of the seal after the applied thermal loads. Besides the qualification tests, the technical feasibility of the sealing concept will be thermal cycle tested with this profile as part of the experimental investigations for development in the course of this thesis.

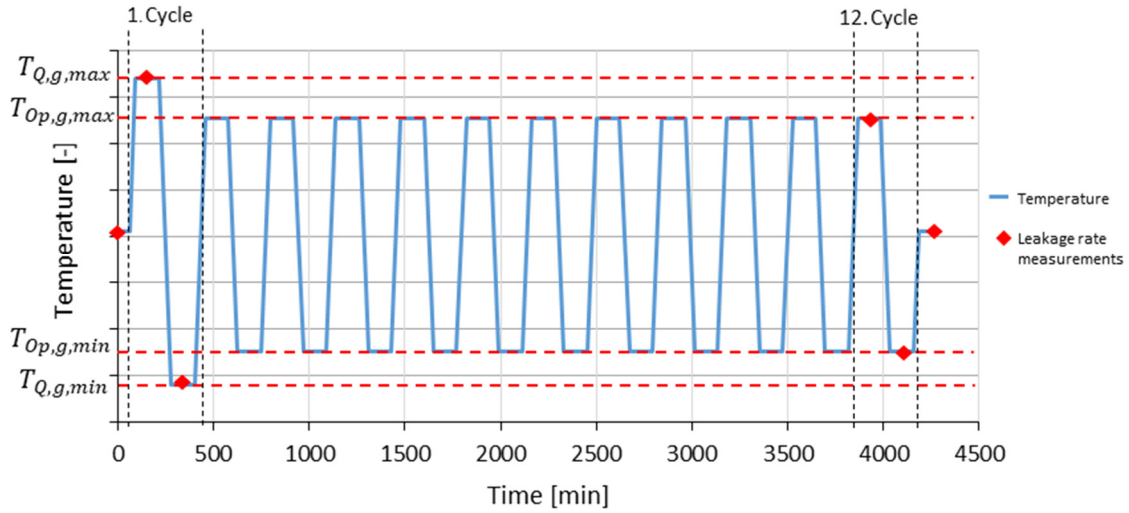

Figure 11: Thermal cycling profile for sealing performance test

4. Valve design

The prior chapters provided an overview over the previously proposed valve design, as well as its novel revised requirements. The objective of this chapter is to present the optimization of the valve's design conducted to comply with all stated requirements. As mentioned before, the occurring pressure drop of the valve is one crucial performance parameter evaluating its competitiveness. Therefore, the first part of this chapter focuses on a design iteration to minimize the valve's hydraulic resistance. Referring to the shock load generation requirement, an analytical calculation of the resulting shock is presented further. This includes especially the evaluation of a suitable spring for implementation. To verify the conducted changes on the valve's design, finally a numerical mechanical strength analysis is conducted. This especially comprises the determination of the notched tube's elongation at break to ensure the suitability of the NC valve's actuator. Concluding this chapter, the verified valve design is proposed by presenting a prototype.

4.1 Hydraulic resistance study

The basis for this hydraulic resistance study is represented by the pressure drop requirement 3.1.6. Within the following subsection, a computational fluid dynamic (CFD) simulation of the stated three representative fluids Xenon, Helium and water is conducted. Resting upon a detailed analysis of the occurring flow phenomena, design iterations of the valve's flow path are made and presented. Firstly however, a research on the theoretical principles of CFD and especially on the utilized algorithms by Solid Works' implemented *Flow Simulation Tool* is conducted.

4.1.1 Theoretical principles

CFD tools usually aim for approximating the Navier-Stokes equations as accurate, as fast and as robust as possible. The Navier-Stokes equations are partial differential equations of hyperbolic-parabolic character and describe the conservation laws of fluid dynamics. The mass, momentum and energy conservation laws are given by [20][21]:

$$\begin{aligned} \rho_t + \nabla \cdot \left(\rho \underline{v}\right) &= 0 \\ (\rho \underline{v})_t + \nabla \cdot \left(\left(\rho \underline{v}\right) \circ \underline{v}\right) + \nabla p &= \nabla \cdot \underline{\underline{\tau}} \\ e_t + \nabla \cdot \left(\underline{v}(e+p)\right) &= \nabla \cdot \left(\underline{\underline{\tau}}\, \underline{v}\right) - \nabla \cdot \underline{q} \end{aligned} \tag{4.1}$$

Wherein $\underline{v}$ constitutes the velocity in all three spatial direction, while $\underline{\underline{\tau}}$ is the tensor of friction and $\underline{q}$ describes thermal conduction. For further definitions see [20]. By formulating the fluid state vector $\underline{U}$ and the convective and viscose flux vectors $\underline{F}^C$ and $\underline{F}^D$, these laws can be summarized by:

$$\underline{U}_t + \nabla \cdot \underline{F}^C\left(\underline{U}\right) = \nabla \cdot \underline{F}^D\left(\underline{U}, \nabla \underline{U}\right) \tag{4.2}$$

The diverse effect of $\underline{F}^C$ and $\underline{F}^D$ on the solution's propagation is pictured by figure 12, where c constitutes the characteristic velocity. The dissipative character of the viscose flux can clearly be identified. This property is the mathematical description of the resulting pressure drop by dissipation. By implementing and solving these flux vectors a finite volume method (FVM) is utilized. This method is based on the separate treatment of spatial and time discretization, the so-called method of lines. The spatial discretization is implemented by calculating the integral values of finite control volumes with defined structures. By connecting them adequately, the numerical fluxes across the cells' borders can be determined [20][21]. Today various methods exist to approximate the flux functions numerically. The CFD solver of Solid Works therefore utilizes a SIMPLE-approach (semi-implicit for pressure linked equations) to prevent the pressure-velocity decoupling occurring for incompressible Navier-Stokes

equations [22]. Further information on the FVM and the SIMPLE approach can be found at [20] and [22].

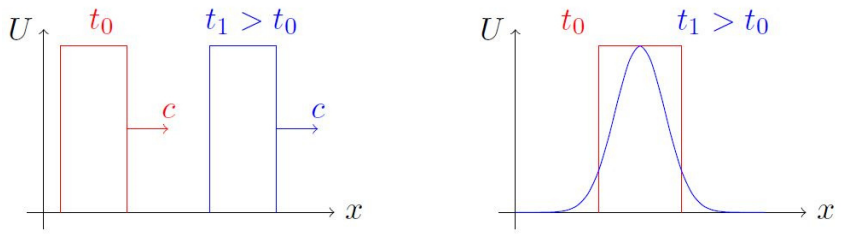

Figure 12: Influence of convective (left) and viscose (right) fluxes on solution state vector [21]

Boundary layer

As described and pictured above, the viscose fluxes of the Navier-Stokes equations take into account the dissipative character of the fluid flow caused by friction. Besides the negligible dissipation between fluid particles themselves, this results in a formation of a boundary layer at a solid and quiescent boundary. Hence, at a wall, fluid particles underlie the no-slip condition – the fluid velocity is zero. A boundary layer is defined as following, wherein δ describes the layer's thickness [23].

$$v_x(y = 0) = 0$$
$$v_x(y = \delta) = 0.99 \cdot v_\infty \tag{4.3}$$

The knowledge of the flow phenomena within the boundary layer is of overall importance for a determination of a hydraulic resistance. According to the Newton's law of friction the shear stresses occurring inside the boundary layer result directly in the skin friction drag and hence the hydraulic resistance [24][23]. Furthermore, a turbulent boundary layer increases the impulse exchange between fluid particles and a solid wall drastically. This again increases the hydraulic resistance. Boundary layers can be described by Prandtl's boundary layer equations [23]. The Solid Works CFD tool approaches to solve these very equations and therefore utilizes an adaptable code which distinguishes between a thin and thick boundary layer. Thin and thick is defined in terms of the ratio between the boundary layer thickness and the number of cells across this layer [22]. The analysis of the boundary layer will be a valuable method during the later presented pressure drop optimization.

Turbulence model

Not only the boundary layers of laminar flows can provide turbulent characteristics, but so can the main flow itself too. If the Reynold's number of a flow exceeds a critical value, the entire main flow experiences a change from laminar to turbulent. This critical Reynold's number holds:

$$Re_{crit} = \frac{\rho v_\infty d}{\eta}\bigg|_{crit} = 2300 \tag{4.4}$$

With the occurrence of a turbulent flow within a tube, the law of Hagen-Poiseuille, which relates the volume flow rate to the pressure difference between inlet and outlet, loses its validity as it yields a too low pressure drop. Therefore, turbulent models need to be implemented to calculate the resulting higher pressure drop caused by an increased impulse exchange. A common empirical and analytical model for a flow inside a hydraulically smooth pipe was introduced by Heinrich Blasius. According to this correlation, the Darcy friction factor follows to:

$$\lambda = 0.3164 \cdot Re^{-\frac{1}{4}} \text{ for } Re < 10^5 \tag{4.5}$$

A numerical approach to approximate turbulences, is the so-called k-ε model. This model describes turbulences by utilizing two transport equations in form of substantial differentiations for the turbulent energy k and the dissipation ε. Both equations exist of three terms which describe the production, the dissipation and the diffusion of turbulences. This common turbulence model is implemented within the Solid Works CFD tool. By visualizing the time averaged turbulent mean values, the analysis of the

turbulent energy k constitutes a valuable method to evaluate and assess the later presented design iteration.

4.1.2 Flow characterization

In order to implement the correct set-up for the numerical simulation it is of overall importance to characterize the occurring flow types in advance. The Solid Works wizard enables the distinction between incompressible and compressible flows, as well as laminar and turbulent flows. Depending on these distinctions the implemented codes differ in terms of quickness, robustness and accuracy. If in reality a turbulent flow occurs but is not considered by the CFD solver due to a wrong set-up, falsified results are obtained. Hence, these phenomena need to be characterized in advance.

For the following calculation the valve's inner hydraulic diameter and length is set to d and l respectively.

Liquid water:

The properties of water at 20°C are already stated within the previous chapter (ref. 3.1.6). With a defined mass flow rate of 150 g/s from table 3, the flow velocity follows to:

$$v_{water} = \frac{\dot{m}_{water}}{\rho_{water} \cdot \frac{\pi}{4} d^2} = 7.7 \, \frac{m}{s} \tag{4.6}$$

The Reynold's number then yields:

$$Re_{water} = \frac{\rho_{water} \cdot v_{water} \cdot d}{\eta_{Water}} = 38312.3$$
$$10^5 > Re_{water} > Re_{crit} \tag{4.7}$$

This shows that 150 g/s of water running through a ¼" tube demonstrate a fully turbulent flow at both the main flow and the boundary layer. As described above, the empirical Blasius correlation from equation (4.6) now applies for this flow. According to this correlation for λ, the pressure drop of a ¼" tube results from Darcy's equation (4.10) to:

$$\lambda_{water} = 0.3164 \cdot Re_{water}^{-\frac{1}{4}} = 0.0226 \tag{4.8}$$

$$\Delta p = \frac{\rho_{water} \cdot v^2}{2} \cdot \left(\lambda_{water} \cdot \frac{l}{d} \right) = 1.78 \cdot \Delta p_{water,req} \tag{4.9}$$

A comparison between the calculated Darcy friction coefficient according to Blasius and the reading from a Moody diagram, demonstrates good compliance. For this consideration a roughness of $R_a = 1.6$ µm is estimated. The analytical determination of the pressure drop of a straight tube results in two important conclusions: From equation (4.9) and figure 13 it can be seen, that the pressure drop is proportional to the flow velocity squared and hence, by applying the mass conservation law, proportional to the reciprocal of the hydraulic diameter to the power of five. This means a change of the mass flow rate and especially the hydraulic diameter provides a huge impact on the resulting pressure drop. Secondly, the obtained value of $\Delta p = 1.78 \cdot \Delta p_{water,req}$ constitutes the lowest possible pressure drop of a straight ¼" tubing with the length corresponding to the SMAV and a water mass flow rate of 150 g/s. Hence, this will be the hypothetical lowest possible pressure drop of the SMAV. In fact this means, that the pressure drop requirement is impossible to meet with the current dimensions of the SMAV NO. The pressure drop's dependency on the mass flow rate and the tube's diameter is depicted in figure 13 below.

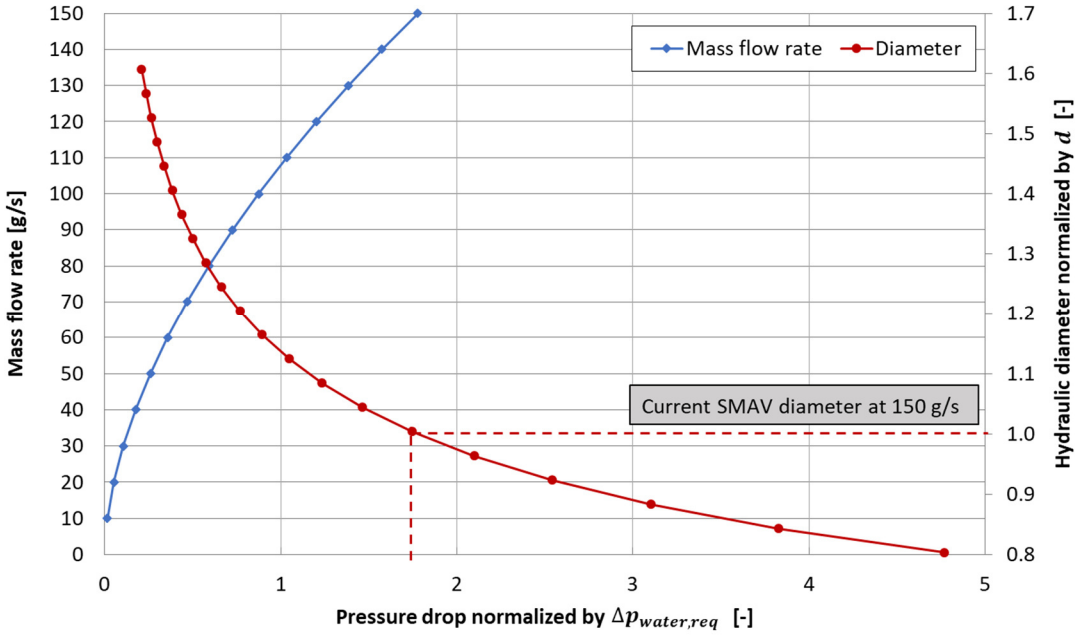

Figure 13: Pressure drop dependency of straight tube with length l and $R_a = 1.6\ \mu m$

Gaseous Helium and Xenon:

A similar consideration needs to be conducted in advance of implementing the numerical simulation of the gaseous flows of Helium and Xenon. While applying the mass flow rates and environmental conditions such as pressure and temperature from table 3, the values for density, velocity and the resulting Reynold's and Mach numbers can be calculated as stated in the following table 5. Regarding the Reynold's numbers, two different flow types for the considered gases can be identified. Due to its very low mass flow rate, the Xenon flow provides laminar characteristics. As the Reynold's number for Helium exceeds the above stated critical Reynolds number, this flow needs to be handled as fully turbulent. However, considering the low Mach numbers both gases can be considered incompressible (Ma < 0.3). This states an important distinction to obtain correct results while saving computational time implementing the CFD simulation within Solid Works.

Table 5: Flow characterization of gaseous Helium and Xenon - gas properties from [24]

Gas	Isentropic exponent γ [-]	Specific gas constant R_S [J/(kg·K)]	Dynamic viscosity η [µPa·s]	Density ρ [kg/m³]	Velocity v [m/s]	Reynolds number	Mach number
Helium	1.63	2078	18.7	56.6	0.544	8203	$5 \cdot 10^{-4}$
Xenon	1.67	63	21.1	812.2	$7.6 \cdot 10^{-5}$	15	$4 \cdot 10^{-7}$

4.1.3 Implementation

In advance of implementing a CFD simulation, a most important aspect worth considering is the set-up of a mesh geometry, boundary and initial conditions appropriate for the regarded problem. As Solid Works *Flow Simulation Tool* is embedded in its CAD environment, the tool directly uses the CAD model's geometry to generate a computational domain. Therefore, the model's surfaces are considered as solid no-slip walls with a defined surface roughness of R_a = 1.6 µm in this case. The inlet and the outlet port of the valve are assigned to subsonic inflow and outflow boundary conditions. Furthermore, the pressures and temperatures from table 3 are applied to the respective ports. Considering the intended application of the SMAV NO within a space environment, the simulation is conducted with neglecting the influence of gravity. In order to keep the model straight forward, heat transfers between fluid particles and solid walls are neglected by defining adiabatic wall conditions.

A main aspect of the set-up constitutes the mesh generation. Commonly, unstructured triangle meshes as depict in figure 14 a.) are implemented for complex geometries. Simpler geometries are often simulated by utilizing a structured mesh as shown in figure 14 b.). However, those body-fitted meshes come with some significant drawbacks such as over-refinement considering a mesh generation directly sourcing from a CAD model [22]. This states the reason, why Solid Works CFD solver implements a structured Cartesian immersed-body mesh as seen in figure 14 c.). These meshes provide decisive advantageous in terms of error minimization and ease and robustness of implementation [22]. At the model's boundaries, Cartesian-based meshes result in divided cells. The cells are distinct in solid-, fluid- and partial cells. Partial cells basically are divided again in various solid and fluid control volumes. This makes a refinement of partial cells particularly crucial, especially at small scale geometric features. As a result, a mesh with adequately refined partial cells is implemented. A detail view from the resulting mesh is presented in figure 15.

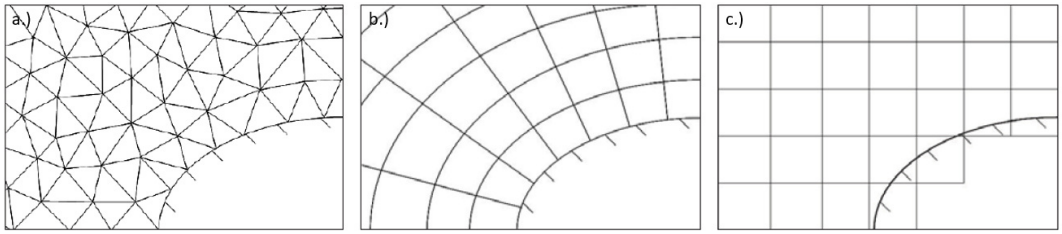

Figure 14: Mesh variants for CFD FVM: a.) body-fitted unstructured mesh; b.) body-fitted structured mesh; c.) immersed-body Cartesian mesh [22]

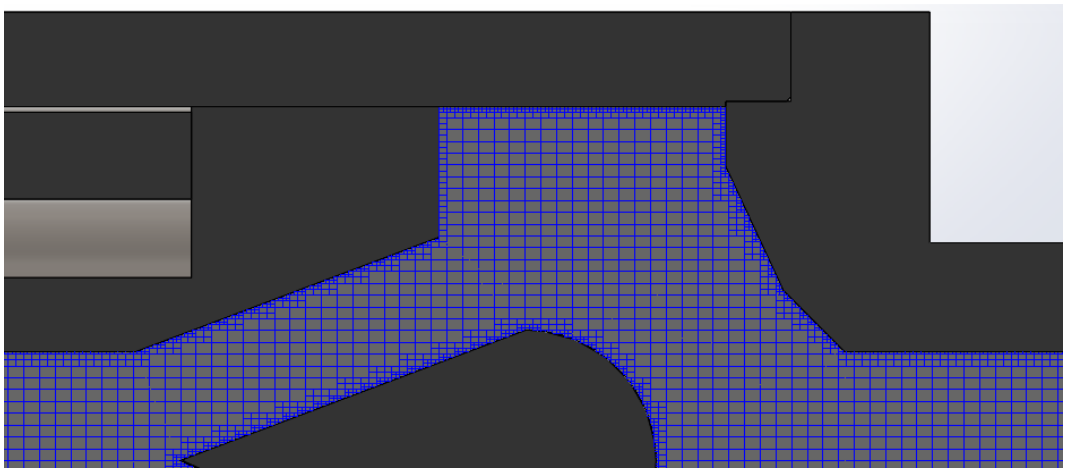

Figure 15: Detail of generated Cartesian mesh

4.1.4 Water-based parameter study results

Within this subsection, the results from the parameter study regarding the optimization on the valve's pressure loss are presented. Due to reasons of clarity, 8 designs are selected and outlined in the following. The design iteration is conducted evaluating the results for a water-based simulation. The final evaluated design is then simulated with Helium and Xenon gas as well. All design iterations are evaluated and limited considering aspects of manufacturing effort and costs.

Design I: Basic

For a first quantification of the pressure loss, a similar variant of the valve design as proposed by Lux is investigated. The design is already pictured by figure 5. It mainly provides a poppet with a diameter slightly larger than the seat's inner edge on which it is pressed onto. In In open and non-activated condition, the flow is guided around the poppet trough drilled holes as pictured in figure 16. The holes provide no circular geometry but are widened to provide a larger flow path area. The CFD results are visualized at figure 17. Figure 17 a.) presents time averaged streamlines of the turbulent flow. Additionally, the colored contour plot represents the water's velocity. Figure 17 b.) illustrates the above discussed turbulent energy k.

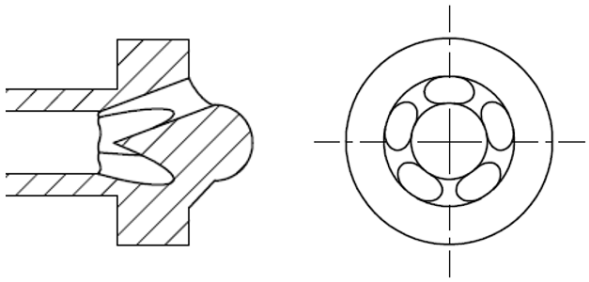

Figure 16: Poppet of design variant I

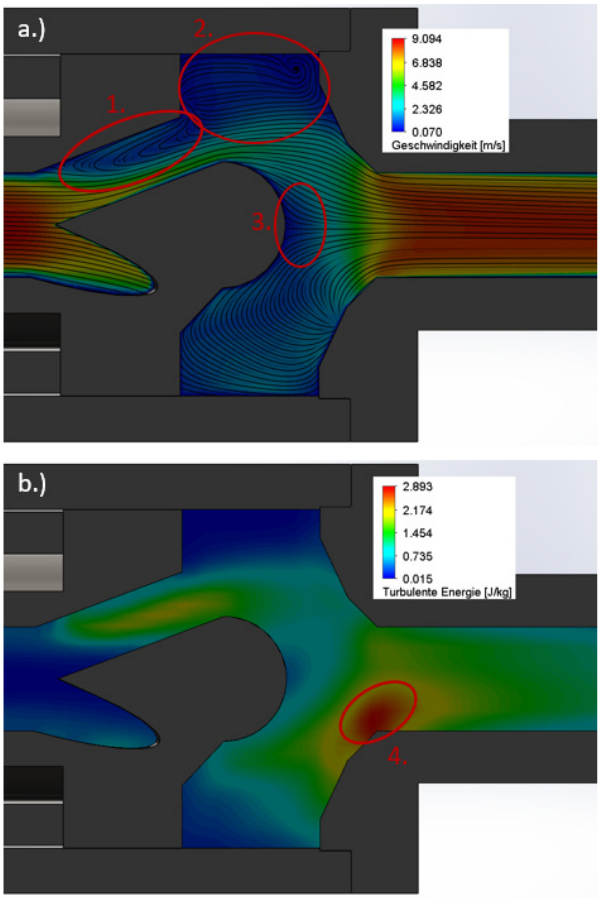

Figure 17: CFD results of design I: a.) Velocity with streamlines; b.) Turbulent energy

As indicated in the figure on the right, 4 areas of special interest can be identified. Area (1) and (2) basically constitute wake spaces and return flow areas. Different than area (2), which provides a minor influence on the main flow as it only constricts it, area (1) strongly affects the flow inside the drilled ducts. By enlarging the boundary layer at this section, it reduces the effective flow path's cross-sectional area drastically and thus results in a higher pressure loss due to increased turbulence. This large turbulent enhanced area can also be identified in subplot b.). Area (3) constitutes another wake space, caused by the detachment of the turbulent flow passing the rear side of a sphere. Considering the high velocity gradient in x-direction at the seat's inner edge, accompanied by the strong turbulent area (4), the conclusion is evident, that the sharp edge and the strong acceleration at the seat result in a high hydraulic resistance. All in all, this design variant provides a pressure loss pressure loss of $\Delta p_1 = 3.4 \cdot \Delta p_{water,req}$.

Design II: Switch of seat and poppet arrangement

From the above outlined design it is identifiable, that the high pressure loss is caused by a design which does not enable an adequate following of the fluid streamlines along its contour. On the first sight and from literature, it is evident, that the droplet form of the poppet and its junction is attacked by the fluid flow from the *wrong* direction. A flow impinging onto the sphere side of the poppet followed by the flow around a tapered cone would allow a good streamline following along its contour. Hence, the first idea is to simply switch the inflow and outflow port of the valve by changing the flow direction. However, this would include, that the spring would need to work against an applied MEOP at the other side to close the seal. A way stronger spring would be necessary in consequence. This however, would violate the shock load generating requirement entirely. Furthermore, a stronger spring provides larger dimensions and thus would require a larger space for installation which cannot be provided between the valve's actuator and the notched tube. Thus, a second variant is investigated and simulated which keeps the original flow direction, while implementing the poppet at the rear housing and the seat at the notched tube inversely. This especially allows a widening of the inner hydraulic diameter of the notched tube. The CAD model with its corresponding CFD results can be seen in figure 18.

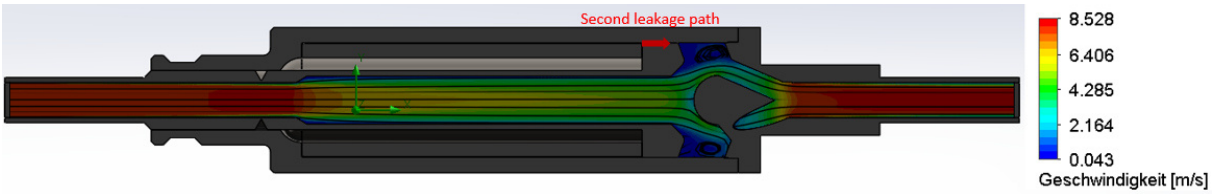

Figure 18: CFD results of design II: Velocity with streamlines

Figure 18 clearly shows, that the resulting streamlines cover the new poppet's geometry more smoothly. In detail, the areas (1), (3) and (4) identified at design I can be eliminated entirely with this design. Furthermore, as the hydraulic diameter affects the resulting pressure drop significantly as shown in section 4.1.1, the enlarged hydraulic diameter of the notched tube further decreases the resulting pressure loss. Thus, a pressure loss of $\Delta p_2 = 2.1 \cdot \Delta p_{water,req}$ can be reached. This constitutes an only 17 % higher pressure drop than for a straight ¼" pipe.

However, this design provides a major drawback which cannot be identified from the CFD simulation. In activated condition, when the notched tube is ruptured, the area around the spring and the actuator fills with fluid. To provide a sufficient glide behavior of the notched tube at the housing wall, this gap is not leak tight. Hence, when the valve would be activated, the fluid would easily follow the second leakage path along the housing and through the poppet's junction ducts as indicated in figure 18. Obviously, this would result in an entire failure of the valve's functionality. As the addition of flexible seals for this path, as e.g., a metal membrane bellow is rejected due to too high manufacturing and developing efforts, this design II is rejected at this point.

Design III: Basic with small poppet

As shown within the previous section a switch of the poppet and seat arrangement is not possible. Thus, this design III again investigates an arrangement similar to design I. To reduce the sealing forces, which will be discussed in detail within chapter 5.1.1, Radermacher proposed a smaller poppet diameter while maintaining the seat's hydraulic diameter. Along with the evaluation of the sealing force, a novel and smaller poppet diameter is chosen for this implementation. The CAD model and the resulting flow phenomena are presented in figure 19. The previously identified areas (1) to (4) are indicated again. It can be seen that area (2) and (3) remain quite similar compared to design I.

However, the smaller poppet diameter results in a decreased angle of direction change for the fluid. As indicated by the significant smaller area (1), this results in a decreased turbulent back flow area and does not enhance the boundary layer as strong as design I. This also clarifies, as area (1) disappears almost entirely at the plot of turbulent energy. However, the decreased deflection also results in a higher flow velocity around the poppet and at the impingement onto the valve seat's inner edge. This subsequently induces strong turbulences at this area (4), which can be seen in figure 19 b.). Comparing the scales of the turbulent energy between design I and III however, the maximal occurring turbulences remain lower than at design I. This directly contributes to a saving of dissipation due to turbulences and thus yields a lower overall pressure drop. This design provides a loss of pressure to ambient pressure of $\Delta p_3 = 3.1 \cdot \Delta p_{water,req}$.

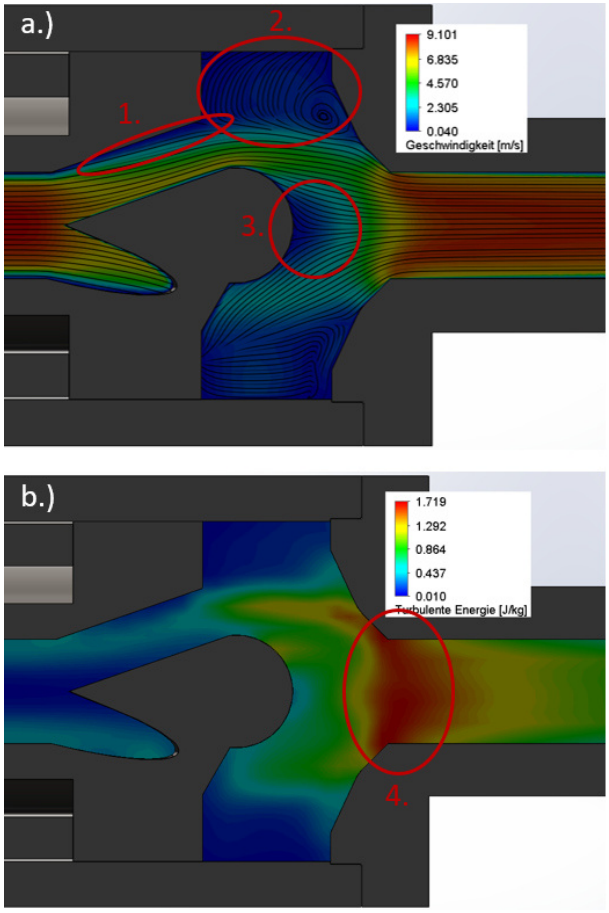

Figure 19: CFD results of design III: a.) Velocity with streamlines; b.) Turbulent energy

Design IV: Basic with large seat

Previous design iterations have demonstrated that the seat's inner edge constitutes critical for inducing turbulences and contributing to a high hydraulic resistance. Thus, this design IV aims to reduce these very turbulences and seat induced pressure losses by optimizing its geometry. Considering the results from figure 13, the hydraulic diameter provides the main impact onto the pressure drop. Applying this principle to the valve design, it is evident to increase the seat's inner diameter. However, as the valve is supposed to provide an ¼" interface, the enlarged diameter needs to be decreased again within the length of the rear housing. The resulting geometry can be seen at the CAD model from figure 20. Enlarging the seat's inner edge includes an increase of the circumference of the sealing line and hence would increase the sealing force. However, within chapter 5.1.1 it is shown, that maintain the original poppet diameter while increasing the seat's diameter in fact, decreases this sealing force. Thus, this simulation implements a seat diameter enlarged by 14 % compared to design I, while maintain the poppet's diameter constant. As this design provides a poppet to seat diameter ratio of 108 % similar to the previous design with 105 %, the flow regimes (1), (2) and (3) picture quite similar as well. However, figure 20 b.) shows, that the newly enlarged seat's diameter drastically decreases the induced turbulences (4). This mainly is caused by a lower flow velocity at the seat's edge and the entire rear housing. Further it can be seen that the downstream constriction of the hydraulic diameter does not cause additional turbulences but only accelerates the fluid slightly. All in all, this design iteration provides a further saving of pressure losses which results to $\Delta p_4 = 2.8 \cdot \Delta p_{water,req}$.

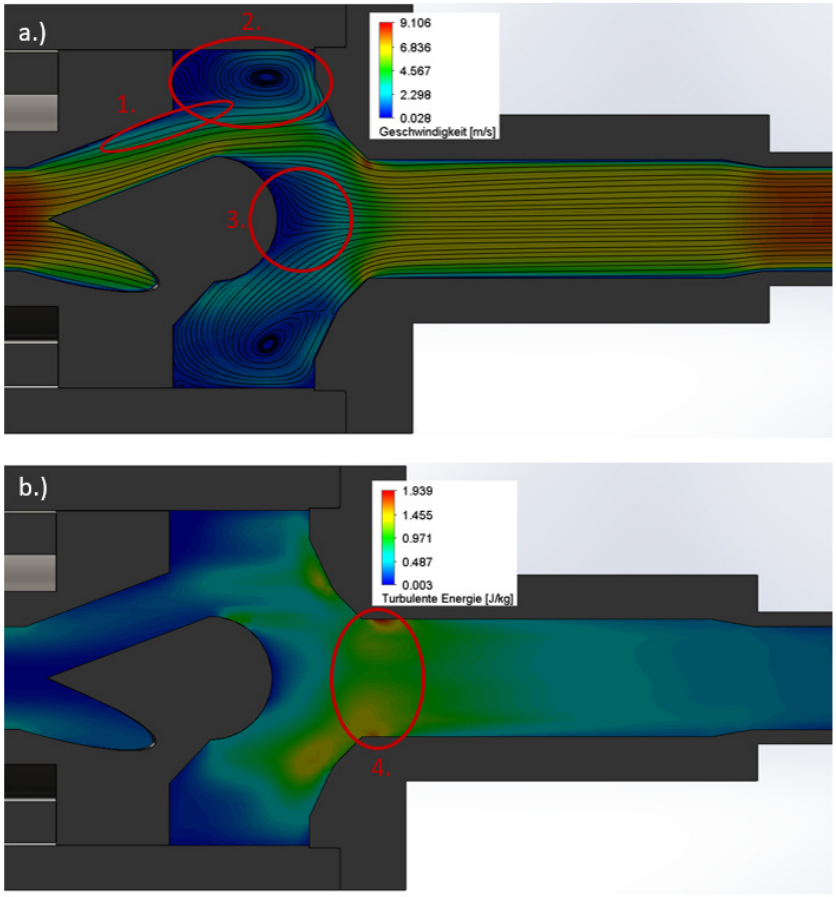

Figure 20: CFD results of variant IV: a.) Velocity with streamlines; b.) Turbulent energy

Design V: Dimples and tabulators with large seat

At design I, III and IV, always a large wake space at the trailing side of spherical poppet, area (3), could be identified. An early flow detachment around a sphere results in a low pressure area (3) and thus in a higher hydraulic resistance [23]. To delay this detachment, so that the flow adhere to the sphere's surface longer, a common technique is the purposed disturbance of the boundary layer. A turbulent boundary layer keeps the flow attached to the surface longer than a laminar boundary layer [23]. Therefore, the principle bases on inducing a change from a laminar to a turbulent boundary layer. A popular example for this principle is a golf ball with its so-called dimples all around its surface. A similar design approach is applied to the spherical poppet of the SMAV. Figure 21 a.) illustrates the implemented three rows of dimples. However, due to manufacturing aspects and as the poppet still needs to provide a smooth sealing surface, the dimples can only be applied at the transition area from conical junction to spherical poppet.

At the seat's side, the previously gained improvement by an enlargement of its inner diameter is applied for this design variant as well. Furthermore, to reduce the flow's velocity at the seat's inner edge and to induce turbulences on purpose likewise the dimples, turbulators are implemented at the seat's outer edge. In order to keep those turbulators as simple as possible considering manufacturing aspects again, simple triangle shapes with rounded edges are implemented. A sketch of the integrated seat into the rear housing can be found in figure 21 b.).

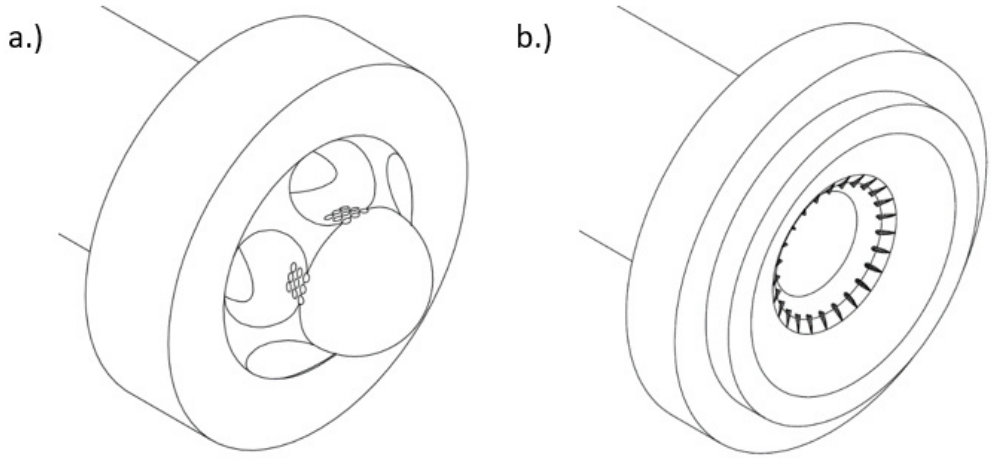

Figure 21: Design variant V: a.) Poppet with dimples; b.) Seat with turbulators

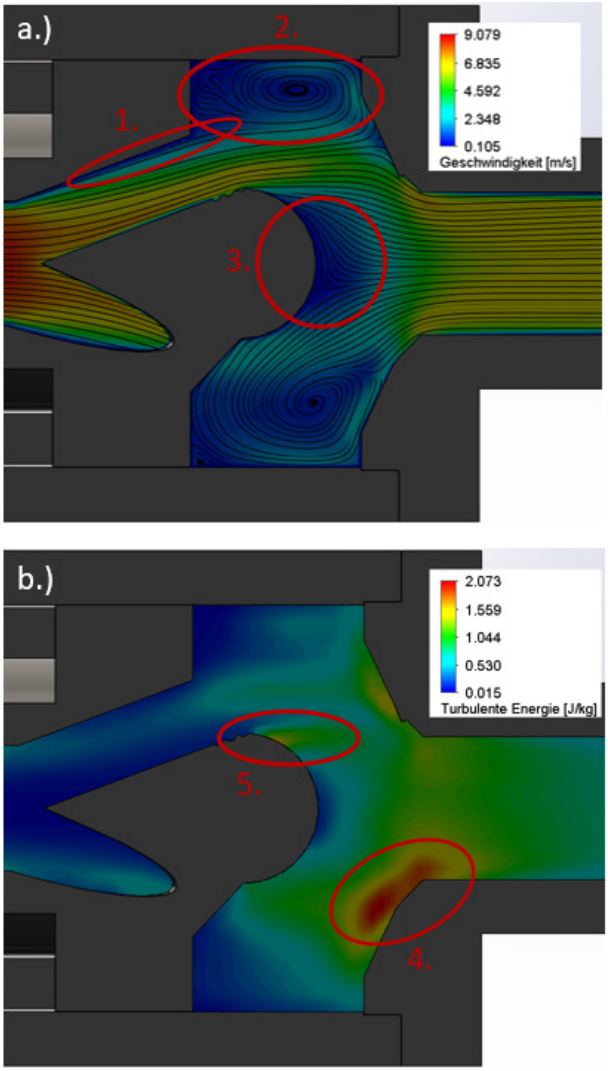

Figure 22: CFD results of design V: a.) Velocity with streamlines; b.) Turbulent energy

The corresponding results from the CFD simulation can likewise be found in figure 22 on the left. It can clearly be seen, that the implemented dimples did not lead to the desired reduction of the wake space (3). This is assumed to be caused by an already turbulent boundary layer when the flow hits the dimples, which results from the turbulent inflow onto the conical junction. This way, the dimples are unable to fulfil its purpose of changing the boundary layer's state of turbulence. However, regarding area (5) it can be stated, that the turbulent energy after the dimples did in fact increase slightly compared to the similar area from design IV. Plot b.), picturing the turbulent energy, reveals another setback of this design. The dimples seem to induce a less rotational symmetric flow and to cause high turbulences and pressure losses at the valve's seat again – compare area (4). An influence of the turbulators at this area can be excluded, as the simulation was conducted twice with and without the turbulators. Both simulations presented the same turbulent area. Design V therefore provides an overall pressure drop of $\Delta p_5 = 3.0 \cdot \Delta p_{water,req}$ for 150 g/s of liquid water and ambient pressure at the outlet. Thus, this design needs to be ranked between design III and IV.

Design VI: Rhombic poppet and large seat

As the previous design iteration failed to reduce the resistance inducing wake space downstream the poppet, another variant is developed which should fulfil this purpose. This variant bases on the results from design II, that a tapered cone provides a more streamlined contour than the rear side of a sphere. Based on this finding, the poppet is redesigned, now constituting out of two tapered cones – hence a sort of rhombus. At the area of the sealing line the poppet still provides a spherical shape which merges tangential into the rear cone. At the rear housing and its integrated seat, the enlarged hydraulic diameter is applied again. The CAD model and its CFD results are displayed in figure 23.

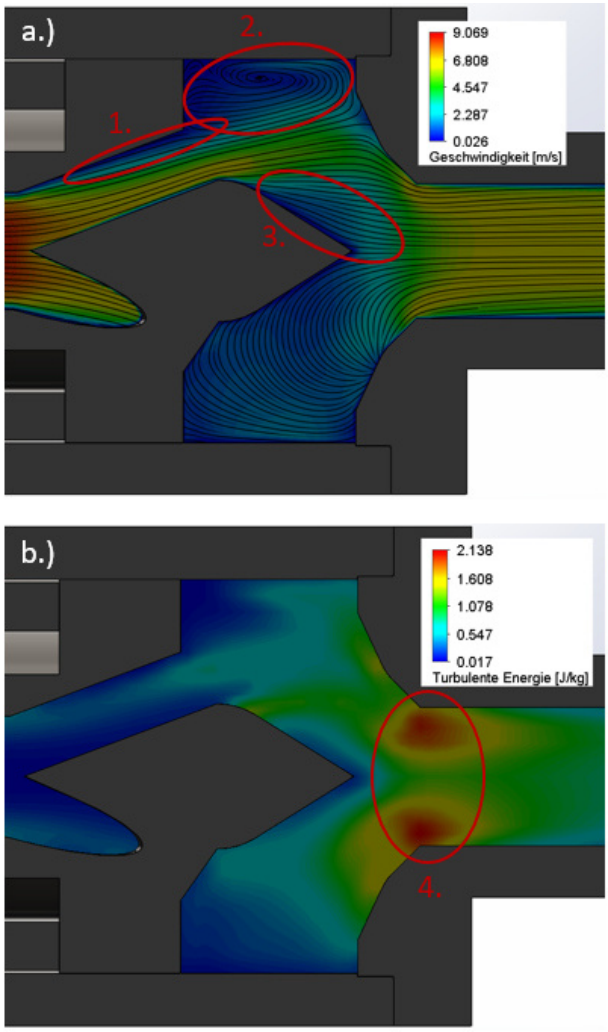

Figure 23: CFD results of design VI: a.) Velocity with streamlines; b.) Turbulent energy

Again, the flow regimes (1) to (4) can be clearly identified and are marked accordingly. It can be seen that the rhombic shape of the poppet provides a significant influence on the former wake space at area (3). The area of very low velocity (dark blue) decreases to a more like boundary layer shape and the streamlines are more aligned to the body's contour. However, the higher velocity of the fluid at this region results in a greater deflection of the fluid layers above and causes a decrease of area (2) especially at the rear housing's surface. This particularly results in a large required direction change towards the seat's port of fluid particles at high speed between area (2) and (3). The turbulences which are induced this way are clearly identifiable at area (4). Compared to design IV, much greater turbulent energy occurs at this area. This again results in an increase of the pressure drop compared to design variant IV. Design VI provides an overall pressure drop of $\Delta p_6 = 3.0 \cdot \Delta p_{water,req}$ with ambient conditions at the outlet port. Hence this design ranks second so far in terms of a lowest possible pressure drop.

Design VII: Reduced wake space and large seat

The two previous designs intended to reduce the wake space at the poppet, at area (3). They demonstrated that a decrease of this area, induces high turbulences at the seat's inner edge which in fact increases the hydraulic resistance instead of reducing it. This design VII therefore aims to reduce the wake space at area (2). The reduction of this area is designed by orientating at the SMAV NO's counterpart the NC valve. This valve utilizes an elastomeric O-ring for improvements of glide behavior and absorbance of shock loads. Hence, the implementation of an additional O-ring constitutes a familiar design and would not increase the development and qualification process enormously. Herein, the idea of this design is adapted to the NO valve. As it can be seen in figure 24, the O-ring is implemented between the rear housing which now reaches far inside the valve's front housing. Inside a groove the O-ring is fixated and is enabled to glide over the surface of the notched tube. Obviously, the notched tube still needs to provide a connection to the actuator to ensure a rupture. As this way, the way of travel is restricted, the poppet is required to be integrated further downstream and more closely to the valve seat. This results in a smaller flow path between poppet and seat.

The CFD results from figure 24 reveal a different flow behavior compared to the previously outlined designs. However, the flow regions (1) to (3) are identifiable again as marked. It shows, that the wake space area (2) indeed constitutes smaller than at previous designs which was the purpose of this iteration. However, it can further be seen, that the back flow from (2) influences region (1) again and enhances its boundary layer drastically. The most important change on the flow behavior is identified by region (4). This area constitutes space of heavy turbulences. From plot b.) it can be seen, that the scale of the turbulent energy exceeds the previous scales and that a large area of turbulences up to 2.4 J/kg exists all around the poppet. Thus it is concluding, that a smaller hydraulic cross-sectional area around the poppet significantly increases the resistance inducing turbulences at this area. Not surprisingly, this design provides a high pressure drop of $\Delta p_7 = 3.2 \cdot \Delta p_{water,req}$ with ambient conditions at the outlet.

Design VIII: Rhombic poppet, reduced wake space and large seat

For a last design iteration, a combination of design IV, VI and VII is investigated. This is intended to combine the advantageous each design provides while eliminating their respective disadvantageous. The resulting CAD model as well as the CFD results are presented in figure 25. The velocity contour plot reveals, that this design indeed leads to an almost entire dispersion of the wake space area (3). However, as the flow cross sectional area around the poppet is further reduced by the additional cone compared to the previous design, even heavier turbulences occur at the seat's port again. In fact, this design results in the highest occurring pressure drop compared to all outlined designs. The pressure drop yields: $\Delta p_8 = 3.4 \cdot \Delta p_{water,req}$.

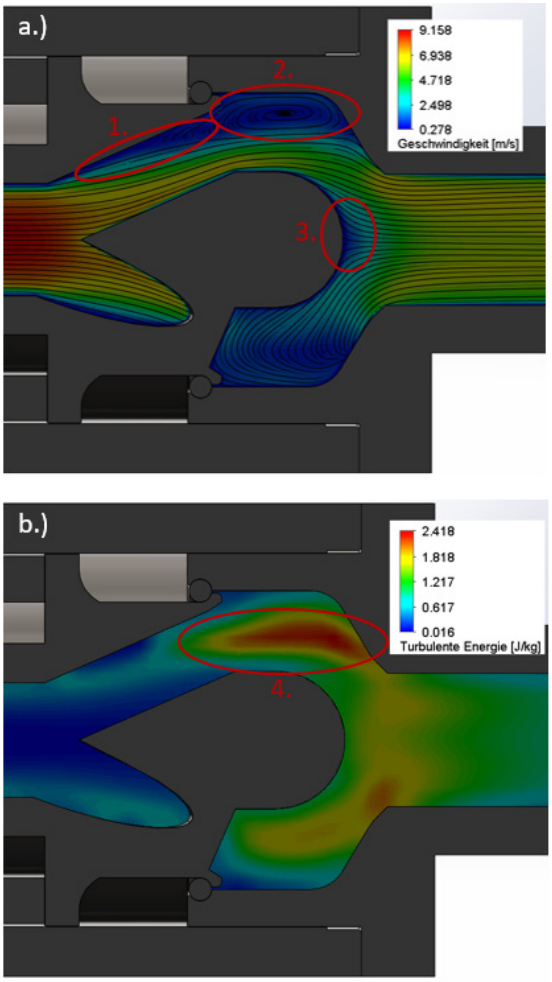

Figure 24: CFD results of variant VII: a.) Velocity with streamlines; b.) Turbulent energy

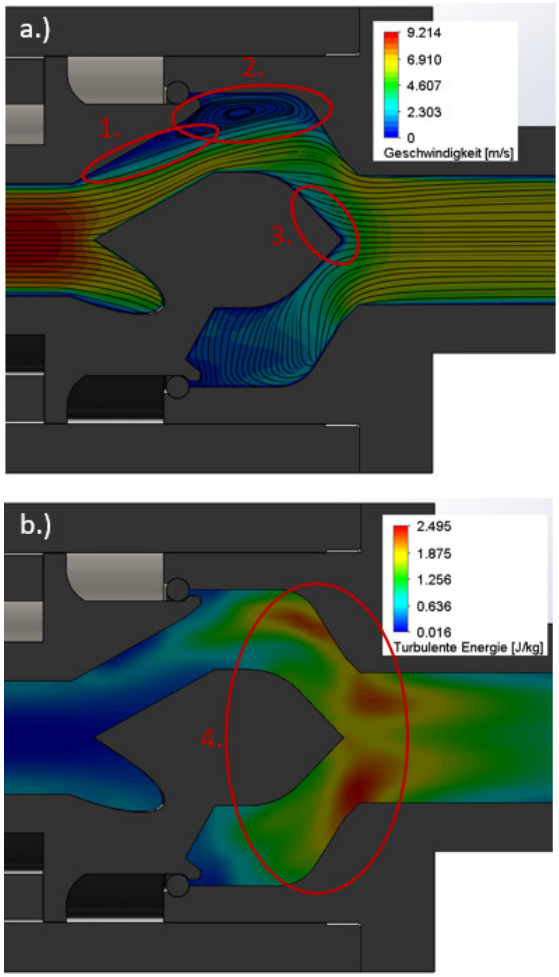

Figure 25: CFD results of variant VIII: a.) Velocity with streamlines; b.) Turbulent energy

Conclusion

Concluding the parameter study on the valve design with the aim to reduce its hydraulic resistance, the following table 6 provides an overview of the results. It is shown that design variant II provides the lowest pressure drop by far but disqualifies for further investigations by its lag of functionality as discussed above. The second lowest pressure drop is yielded by design IV with $\Delta p_4 = 2.8 \cdot \Delta p_{water,req}$. However, even this design does not meet the pressure drop requirement by a factor of 2.8. Furthermore, within subsection 4.1.1 it is shown, that even a straight tube with an ¼" interface and a mass flow rate of 150 g/s water is unable to fulfil this requirement and provides a higher pressure drop by the factor of 1.78. To reach the important pressure drop requirement, an unconventional solution is proposed by collaboration with experts from Ariane Group. As the costs for the SMAV's hardware and easier electronics will largely stay below the equivalent costs for PVs, an implementation of two parallel connected SMAVs each with half of the mass flow rate, would still provide great expenditure savings. As demonstrated above, the pressure drop is proportional to the mass flow rate to the power of 2. Hence, halving the mass flow rate through the valve of design IV would reduce the pressure drop for one valve roughly about to one quarter. Applying the half mass flow rate of water, 75 g/s, another CFD simulation approximates the resulting pressure drop of one valve indeed to $\Delta p_{\dot{m}/2} = 0.75 \cdot \Delta p_{water,req}$. Accounting both valves, this pressure drop again needs to be doubled to yield the entire hydraulic resistance of this solution: $\Delta p_{parallel\ valves} = 1.47 \cdot \Delta p_{water,req}$. This still does not meet the pressure drop requirement entirely but ends up near within an acceptable range of factor 1.47 and simultaneously lower than a straight tube. These are the reasons design variant IV qualifies for the further investigation course of this thesis.

Table 6: Summary of CFD results of design iterations regarding pressure drop optimization

#	Design	Pressure drop [normalized by $\Delta p_{water,req}$]
I	Basic	3.4
II	Switch of seat and poppet arrangement	2.1
III	Basic with small poppet	3.1
IV	Basic with large seat	2.8
V	Dimples and tabulators with large seat	3.0
VI	Rhombic poppet and large seat	3.0
VII	Reduced wake space and large seat	3.2
VIII	Rhombic poppet, reduced wake space and large seat	3.4
--	Two parallel valves	1.5

4.1.5 Gaseous Helium and Xenon results

The numerical simulation of gaseous Helium and Xenon can be implemented a similar way as for water. However, to save computational effort, the Xenon simulation can be conducted utilizing laminar calculation methods as shown previously. A difference to the implementation of water is given by the port at which the pressure boundary condition needs to be applied, presented by table 3. For Helium and Xenon, the respective pressures are applied from the inlet port. By implementing this, the defined criterions for convergence of the CFD wizard need to be adjusted likewise. The results for both simulations are stated in table 7. Due to their much lower mass flow rates and resulting lower flow velocities, the pressure drop for both gases yields much lower than for water. For a Helium flow of 0.6 g/s the SMAV NO provides a pressure drop of $0.4 \cdot \Delta p_{GHe,req}$ which fulfils the pressure drop requirement. Also the occurring peak turbulences remain two orders of magnitude lower than for water. The corresponding pressure drop for a 0.0012 g/s Xenon flow yields even lower and almost negligible to $8 \cdot 10^{-6} \cdot \Delta p_{GXe,req}$. As the entire Xenon flow provides laminar characteristics, no turbulences exist.

Within this subsection the valve has been optimized regarding its pressure drop by utilizing analytical and numerical CFD methods. While the final evaluated design meets the pressure drop requirement for

Helium and Xenon, the similar requirement for water is still slightly missed by the proposed parallel implementation of two optimized valves. Nevertheless, this design IV is chosen for a further mechanical analysis in the following.

Table 7: CFD results of Helium and Xenon simulations

Gas	Pressure drop [-]	Mean velocity [m/s]	Peak turbulent energy [J/kg]
Helium	$0.4 \cdot \Delta p_{GHe,req}$	0.547	0.02
Xenon	$8 \cdot 10^{-6} \cdot \Delta p_{GXe,req}$	$7.95 \cdot 10^{5}$	laminar

4.2 Spring and shock calculation

An adequate spring design of the SMAV NO is a crucial aspect regarding its functionality, reliability and also its hazardous influences on other subsystems due to induced shocks. Therefore, this chapter focusses on the calculation of the shock loads occurring on closing of the valve by preloaded spring. Enabling this calculation, firstly an analytical model of the oscillating spring-notched tube-poppet system is presented. To evaluate potential springs from external suppliers in terms of their suitability, secondly the geometric circumstances at the valve are determined. Within the last subsection, the best suitable spring is evaluated and proposed for the final prototype design.

4.2.1 Oscillation principles

For the indented investigation of shock loads and sealing forces, a model needs to be developed which enables an exact calculation while keeping the model simple. Therefore, two assumption need to be postulated in advance. At actuation and rupture of the notch, the preloaded spring expands rapidly pushing the poppet onto the valve's seat. Hereby, the spring changes from a high state of potential energy into a lower state of potential energy. In reality, the released kinetic energy cannot be absorbed entirely on the first hit. In fact, the poppet bounces back and forth, until the entire spare energy is dissipated. Herein it is estimated that the first impact of the poppet provides the highest kinetic energy and thus generates the peak shock load. That is why, only the first impact of the poppet onto the seat is considered in the following. Secondly, as the spring does not expand until its neutral position, it does not fulfil half of a full oscillation. Therefore, potential occurring damping effects can be neglected. This also includes the effects due to friction of the poppet's junction at the housing's inner wall.

With the rupture of the notch, the spring expands and pushes both, the poppet and the broken part of the notched tube onto the seal seat. As the force on both these masses is induced at the same area of attack, the second spring end, both masses can be cumulated to one oscillating mass m. On release, this mass can oscillate harmonically and undamped in x-direction. Contrary, the second end of the spring is fixated at the valve's housing. The model of this situation is given by figure 26.

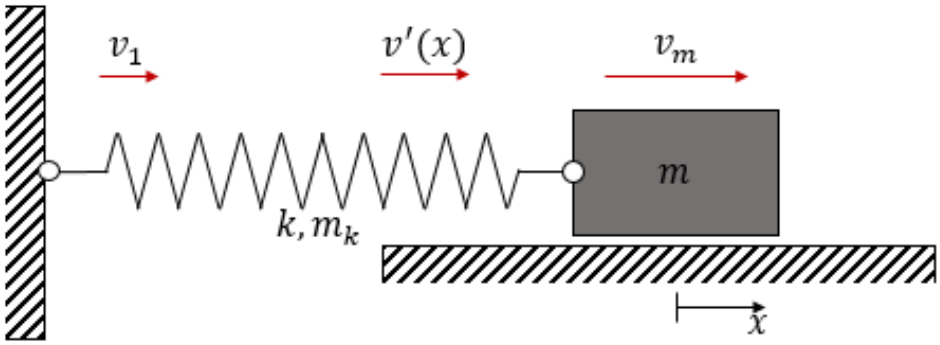

Figure 26: Oscillating model of spring-mass system

The spring stiffness is indicated by k and the spring mass by m_k, coordinate x is accounted from the neutral position of the spring. From Newton's second law and Hooke's law the resetting force onto the attached mass is given by:

$$F = m \cdot \frac{d^2x}{dt^2} = -kx \tag{4.10}$$

By introducing the oscillating frequency $\omega = \sqrt{\frac{k}{m}}$ and equating the coefficients, equation (4.11) can be formulated as:

$$\frac{d^2x}{dt^2} + \omega^2 x = 0 \tag{4.11}$$

This equation constitutes a linearly and homogeneous differential equation of second order and describes the motion of a harmonic oscillating mass in x-direction. A solution of this equation is given by [25][26]:

$$x(t) = \hat{A} \cdot \cos(\omega t + \phi) \tag{4.12}$$

Within this equation, $\hat{A}$ constitutes the amplitude and ϕ defines the phase shift. Considering the given problem herein, the phase shift can be set to zero.

However, only the oscillating mass m has been considered so far, but the oscillating spring mass m_k was neglected. Regarding the mass relations at the SMAV NO, the mass of poppet and broken notched tube is of the same dimension as the spring mass itself. Botch masses will range within a few grams. Therefore, it is essential to take into account the spring mass as well. This however, state's not trivial, as the spring exists of various spring elements which have not the same velocity during an oscillation. Especially, the fixated spring element always remains at rest, while the element attached to the main mass m provides its velocity v_m. All elements in between provide a velocity $v'(x)$ between 0 and v_m. This principle is also indicated in figure 26 above. To consider this behavior, an energy balance is utilized [26]:

$$E_{totat} = E_{kin} + E_{pot} = 0 \tag{4.13}$$

The potential energy directly results from the negative work which is performed along a way. Applying (4.11) E_{pot} follows:

$$E_{pot} = -W = -\int F \cdot d\vec{s} = \int kx \cdot dx = \frac{1}{2}kx^2 \tag{4.14}$$

The kinetic energy however needs to be split into the amount of the oscillating mass m and the amount due to all oscillating spring mass elements dm_k. The kinetic energy for m simply results to:

$$E_{kin}^{m} = \frac{1}{2}mv_m^2 \tag{4.15}$$

The determination of the spring's kinetic energy constitutes more complicated, as its elements does not provide a constant velocity as outlined above. Therefore, the infinitesimals spring mass element dm_k is introduced:

$$dE_{kin}^{k} = \frac{1}{2}v'(x)^2 \cdot dm_k \tag{4.16}$$

Utilizing the homogenous mass distribution of all spring elements, dm_k and $v'(x)$ can be substituted:

$$\begin{aligned} dm_k &= \frac{m_k}{l_0}dx \\ v'(x) &= \frac{x}{l_0}v_m \end{aligned} \tag{4.17}$$

l_0 herein constitutes the spring's length at unloaded state. By implementing these relations, the kinetic energy of the spring follows:

$$E_{kin}^{k} = \frac{1}{2}\frac{m_k}{l_0} \cdot \int_{x=0}^{x=l_0} v'(x)^2 \, dx \tag{4.18}$$

$$E_{kin}^{k} = \frac{1}{2} \cdot \frac{m_k}{3} v_m^2 \tag{4.19}$$

Inserting (4.15), (4.16) and (4.20) into (4.14), the energy balance for the spring-notched tube-poppet system yields:

$$E_{total} = \frac{1}{2} \cdot \left[\left(m + \frac{m_k}{3}\right) v_m^2 + kx^2\right] \tag{4.20}$$

To obtain a similar equation of motion for a harmonically oscillation as given by equation (4.13), equation (4.21) needs to be derivated with respect to time. Note that $v_m = v_m(t)$ and $x = x(t)$.

$$\frac{d^2x}{dt^2} + \frac{k}{m + \frac{m_k}{3}} x = 0 \tag{4.21}$$

By equating the coefficients again and introducing the corrected oscillation frequency $\tilde{\omega} = \sqrt{\frac{k}{m+\frac{m_k}{3}}}$ results to:

$$\frac{d^2x}{dt^2} + \tilde{\omega}^2 x = 0 \tag{4.22}$$

This now states the correct differential equation of motion of the considered oscillation system. It can be solved corresponding to (4.13):

$$x(t) = \hat{A} \cdot cos(\tilde{\omega}t) \tag{4.23}$$

$$v(t) = -\hat{A}\tilde{\omega} \cdot \sin(\tilde{\omega}t) \tag{4.24}$$

$$a(t) = -\hat{A}\tilde{\omega}^2 \cdot \cos(\tilde{\omega}t) \tag{4.25}$$

These equations represent the basis on which the shock loads of the proposed springs will be determined.

4.2.2 Geometric conditions

Other than considered by Lux, literature research [27][28] reveals, that not the entire space between actuator and notched tube can be used as space for the spring implementation. To prevent blocking of the spring during expansion, an additional free space between the spring's inside diameter and the notched tube (Mandrel diameter: index "M") and likewise between the spring's outside diameter and the actuator (Bushing diameter: index "B") have to be considered. Regarding the dimensions of the SMAV, this space is referred to as $\Delta d_{M-k,i}$ and $\Delta d_{k,o-B}$ respectively [27][28]. Hence the maximum installable spring force needs to be recalculated and yields less then stated by Lux. To maximize the available space for implementation, the notched tube's design is optimized. Figure 27 presents the adapted design. The maximum diameter of the spring is limited due to the actuator's dimension which are not variable. Hence, the spring's outer diameter is limited to $d_{k,o} \leq d_B - \Delta d_{k,o-B}$. The inner diameter of the spring is limited due to the front part of the notched tube to enable a welding to the NC housing. As the spring needs to be implemented from this side, this equals its minimum diameter. To enable this diameter however, the notched tube is required to provide the mentioned additional free space. Therefore, its outer diameter, the so-called mandrel diameter is reduced to $d_M = d_{k,i} - \Delta d_{M-k,i}$ from the notch onwards. The maximal length of the spring at compressed condition, hence the maximal block length is indicated as $l_{b,max}$. An additional ring is clamped into the housings groove to enable a flat and stable stop for the spring.

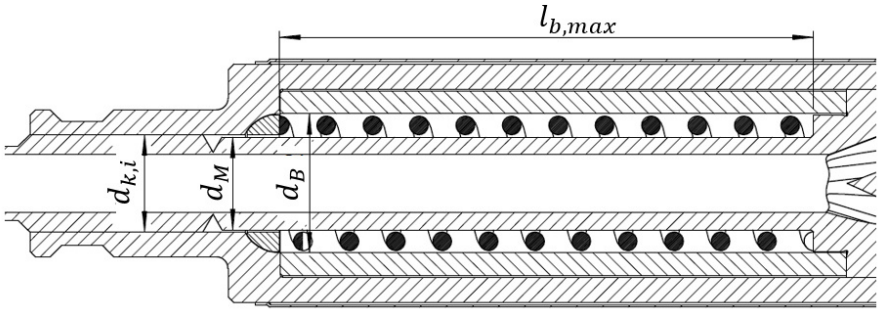

Figure 27: Geometric conditions and maximal available space for spring implementation

The mentioned dimensions, as well as all further parameter which are needed for the spring calculation are given by the following table 8.

Table 8: Geometric conditions for spring implementation

Parameter	**Symbol**
Bushing diameter	d_B
Mandrel diameter	d_M
Max. outer diameter	$d_{k,o}$
Min. inner diameter	$d_{k,i}$
Max. block length	$l_{b,max}$
Length of travel	Δx
Max. axial sealing force	F_A
Travel mass (broken notched tube, poppet and poppet junction)	m

With the given geometrical parameter, the strongest installable spring can be determined in a similar way Lux conducted. During previous projects at Ariane Group, the compatibility of spring materials to the specified fluids have been investigated already. Based on this, the spring material is chosen to be a stainless steel for aerospace applications: Material A. Alternatively, another stainless steel, material B is acceptable as it provides similar mechanical properties and a chemical composition. Their respective properties are given by table 9. The actual tensile stress and shear stress hereby is strongly dependent on the mean wire diameter. Their allowable values increase for smaller diameters [28]. This states the reason, the following calculation is conducted with the maximal values from table 9. With the maximal installable spring wire diameter d_w, the polar section modulus for a spring with a circular wire follows:

$$W_{polar} = \frac{\pi \cdot d_w^3}{16} \tag{4.26}$$

By considering the maximal allowable shear stress for the given material, the maximal momentum of torsion yields:

$$M_T = W_{polar} \cdot \tau_{max} \tag{4.27}$$

Eventually, the maximal installable force applied by a fully compressed spring at block length, follows with the mean spring diameter $\bar{d}$:

$$F_b = 2 \cdot \frac{M_T}{\bar{d}} \tag{4.28}$$

Considering the resulting spring stiffness k for this case of i_{eff} effective windings, and applying the length of travel for the poppet, the sealing force yields a little less than F_b:

$$k = \frac{G \cdot d_w^4}{8 \cdot i_{eff} \cdot \bar{d}^3} \tag{4.29}$$

$$F_{s,max} = F_b - k \cdot \Delta x \tag{4.30}$$

The resulting forces given by table 9 exemplify, that the available space for the spring is decisively restricted. Even the strongest available spring for these dimensions and made out of material A does not exceed the load requirement from 3.1.7. The resulting maximal forces applicable by a spring of material B yield slightly higher.

Table 9: Spring materials and maximal installable forces – material properties according to [29]

Material	Tensile stress R_m [N/mm²]	Shear stress τ_{max} [N/mm²]	Shear modulus G [N/mm²]
A	1150 – 2000	575 – 1000	78000
B	1300 – 2600	650 – 1300	73000

Material	Max. installable force F_b normalized by $F_{s,max,1}$ (see 4.2.3 and table 10)	Max. sealing force $F_{s,max}$ normalized by $F_{s,max,1}$ (see 4.2.3 and table 10)
A	1.13	1.03
B	1.47	1.38

4.2.3 Spring trade off and proposal

The previous section revealed, that even the strongest conceivable spring of the material A does not exceed the defined maximal sealing force for the given geometric dimensions. This makes the conclusion obvious, that all available springs made out of this material will not exceed this threshold value, but in fact will hardly reach a sufficient sealing force. Considering the higher maximal potential forces for the material B, commonly available springs might reach and exceed the requirement. An extensive research and comparing products of various spring manufactures yields, that spring dimensions usually are standardized. Hence, different manufactures provide the same spring geometries. For the given SMAV geometry according to table 10, mostly 6 potential suitable springs are available. These springs all provide the same wire diameter but vary in terms of length, wire number and resulting spring stiffness. One out of various spring manufacturer is found to provide two more spring variants (#2 & #3). The found spring dimensions for the resulting 8 variants are given by table 10. The stated properties are valid for springs made out of material B. All found springs made out of material A are largely surpassed in terms of maximal sealing forces. Furthermore, material A constitutes no standard material for all spring manufacturer but could be provided onto request by most of them.

With the stated input values from table 10, all desired output values such as sealing and preload forces, as well as shock loads can be calculated utilizing the principles from section 4.2.1. Thereby, the nominal length constitutes the length which is specified by the supplier for a certain compression. However, theoretically the spring could be compressed further until the block length is reached. Explaining the calculated values from table 10, an exemplary calculation for spring #1 is conducted.

By the given inner and outer diameter, the mean spring diameter and the wire diameter can easily be calculated. Considering the nominal length as the length at which the spring is compressed while preloaded, the spring deflections at open (1) and closed (2) valve state, accounted from its neutral position follow to:

$$x_{1,n} = l_0 - l_n \quad \& \quad x_{2,n} = x_{1,n} - \Delta x \tag{4.31}$$

Applying these lengths, the resulting preload and sealing forces can be determined:

$$F_{preload,n} = k \cdot x_{1,n}$$
$$F_{s,n} = k \cdot x_{2,n} \tag{4.32}$$

However, the spring could be theoretically compressed further as the nominal length until its block length is reached. This would result in the maximal available preload and sealing force:

$$x_{1,max} = l_0 - l_b \quad \& \quad x_{2,max} = x_{1,max} - \Delta x$$

$$F_{preload,max} = F_b = k \cdot x_{1,max} \tag{4.33}$$

$$F_{s,max} = k \cdot x_{2,max}$$

This $F_{s,max}$ defines the maximal available sealing force which can be applied by the considered spring onto the poppet at closed state of the valve.

Arbitrary of the chosen preload, the corrected oscillation frequency then results to:

$$\widetilde{\omega} = \sqrt{\frac{k}{m + \frac{m_k}{3}}} \tag{4.34}$$

Under nominal preload conditions and according to the solutions (4.26) of the equation of motion, the resulting acceleration of the spring at release results to:

$$|a_n(t=0)| = x_{1,n} \cdot \widetilde{\omega}^2 \cdot \cos(\widetilde{\omega} \cdot t) = x_{1,n} \cdot \widetilde{\omega}^2 = 0.33 \cdot S_{req,valve} \tag{4.35}$$

With the time until impact at x_2 the corresponding occurring shock load can be determined:

$$t_{2,n} = \frac{1}{\widetilde{\omega}} \cdot \cos^{-1}\left(\frac{x_{2,n}}{x_{1,n}}\right) \tag{4.36}$$

$$\left|a_n\left(t = t_{2,n}\right)\right| = x_{1,n} \cdot \widetilde{\omega}^2 \cdot \cos\left(\widetilde{\omega} \cdot t_{2,n}\right) = 0.29 \cdot S_{req,valve} \tag{4.37}$$

This load now constitutes the shock load on impact of the poppet onto the seal seat caused by the nominal preloaded spring. If the spring is preloaded heavier until its block length, a similar calculation yields the maximal possible shock load of $\left|a_{max,t_2}\right| = 0.32 \cdot S_{req,valve}$.

From the following table, it can clearly be stated, that no of the considered springs exceed the shock load generation requirement. For recap, this requirement allows a self-induced shock $S_{req,valve}$ measured at the valve itself, and a shock $S_{req,I/F}$ measured at the valve's mechanical interfaces. Even considering an additional margin of $0.3 \cdot S_{req,valve}$ for further shocks occurring as e.g., the shock due to rupture of the notched tube or likewise due to pressure gradients, all springs still provide a sufficient safety factor. The highest shock occurs for spring #1 at a preload up to block length and yields$0.32 \cdot S_{req,valve}$. For this case, the maximal available sealing force results to $F_{s,max,1}$ and herby constitutes the highest sealing force of all considered springs. As the shock generation proves non critical, this spring with the highest available sealing force is proposed for implementation. Hence, all poppet and seat combinations which require a sealing force less than $F_{s,max,1}$ can be considered feasible for the SMAV NO. If the actual required sealing force yields less than this value, this would improve the seal's reliability significantly.

Table 10: Spring trade off normalized by values from spring #1 and $S_{req,valve}$- input values according to [29]

Input	Symbol	Unit	#1	#2	#3	#4	#5	#6	#7	#8
Outer diameter	$d_{k,o}$	mm	n/a	n/a	n/a	n/a	n/a	n/a	n/a	n/a
Inner diameter	$d_{k,i}$	mm	n/a	n/a	n/a	n/a	n/a	n/a	n/a	n/a
Full length	l_0	$\frac{mm}{l_{0,1}}$	1	1	1	0.69	0.62	0.48	0.32	0.22
Block length	l_b	$\frac{mm}{l_{b,1}}$	1	1.2	1.03	0.74	0.7	0.51	0.35	0.26
Nominal length	l_n	$\frac{mm}{l_{n,1}}$	1	1.2	1.01	0.71	0.7	0.5	0.35	0.25
Spring stiffness	k	$\frac{N/mm}{k_1}$	1	0.82	0.97	1.42	1.48	2.1	3.29	5
Mass	m_k	$\frac{g}{m_{k,1}}$	1	1.2	1.03	0.72	0.7	0.15	0.36	0.26
Output										
Nominal force	$F_{s,n}$	$\frac{N}{F_{s,n,1}}$	1	0.67	0.96	0.89	0.73	0.8	0.63	0.38
Max. sealing force	$F_{s,max}$	$\frac{N}{F_{s,max,1}}$	1	0.7	0.95	0.87	0.77	0.81	0.68	0.45
Block force	F_b	$\frac{N}{F_{b,1}}$	1	0.72	0.95	0.94	0.86	0.96	0.98	0.96
Oscillation frequency	$\widetilde{\omega}$	$\frac{Hz}{\widetilde{\omega}_1}$	1	0.74	0.82	1.03	1.05	1.34	1.63	2.04
Nominal shock	$\lvert a_{n,t_2} \rvert$	$\frac{g}{S_{req,valve}}$	0.29	0.19	0.27	0.27	0.23	0.28	0.21	0.13
Max. shock	$\lvert a_{max,t_2} \rvert$	$\frac{g}{S_{req,valve}}$	0.32	0.21	0.3	0.29	0.26	0.31	0.25	0.17

The price of spring #1 depends on the lot size but is almost negligible within a range of a few Euros per piece.

By selecting spring #1, the notched tube needs to be redesigned to enable an appropriate installation of the spring. As stated, the maximal preload of the spring would be achievable by applying a spring deflection until block length. By adding a slight margin onto the block length due to manufacturing tolerances, a preloaded length of $l_{preload} = 1.05 \cdot l_{b,1}$ is chosen. This space must be provided by the notched tube at open valve conditions, hence the available space from figure 27 needs to be decreased slightly. This can be achieved in two ways. One way, the implemented stopping ring between housing and spring could be enlarged or otherwise the notched tube's wall thickness near the poppet could be increased. The second option provides two significant advantageous. Firstly, the resulting shock caused by the preloaded spring scales with the reciprocal of the spring and travel masses – ref. equation (4.26). Hence, by increasing the mass of the notched tube, the resulting shock load reduces. With an increased travel mass of $m' = 1.31 \cdot m$, the shock load eventually results to $0.24 \cdot S_{req,valve}$. Secondly, an increased wall thickness of the notched tube increases its stiffness significantly, which gains importance considering its maximal allowable elongation at break. This is discussed within the following chapter in greater detail. The novel design of the notched tube with the implemented spring #1 is pictured in the following figure 28.

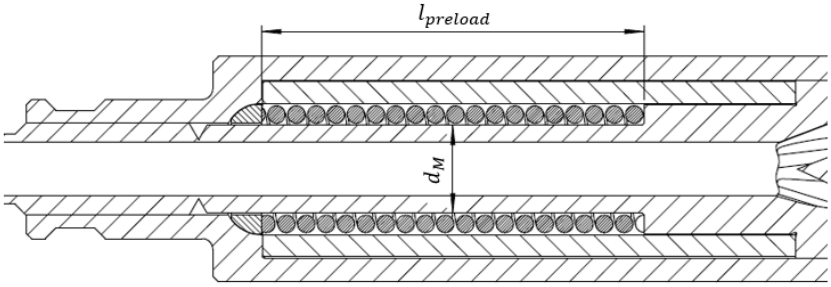

Figure 28: Spring implementation proposal

4.3 Elongation at break

Based on the spring proposal from the chapter above and likewise on the hydraulic resistance study, the notched tube is redesigned compared to previous theses and especially compared to the NC counterpart. This gains importance, as all changes on the design and especially on the tube's thickness and mean diameter significantly affect the tube's stiffness. This could cause the problem, that a lower wall thickness could decrease the stiffness that much, that the actuator would not be able to brake the notch anymore. As the actuator's way of expansion due to its phase transition is strictly limited to a few millimeter, the notched tube's allowable elongation is required to stay within a certain limit as well. This way, the correct working point of the actuator is ensured. The following table 11 presents the geometric conditions to evaluate the maximal allowable elongation of a notched tube while ensuring the rupture by the actuator. Therefore, the actuators expansion must always be greater than the listed spaces and tolerances. The parameter *fitting* describes the design space between actuator and notched tube. By welding the notched tube and the valve housing, the notched tube expands and/or displaces slightly. This parameter is evaluated from measurements on the NC notched tube. By subtracting additional tolerances and a certain safety margin, the maximal allowable elongation of the notched tube results to 29 % of the actuator's expansion.

The investigation on the elongation of the notched tube is conducted applying the geometric conditions according to figure 28. Previous investigations by Lux have proven, that an analytical calculation of the notched tube's elongation provides a quite large error compared to tensile stress experiments. This mainly is caused by the complex geometry of the poppet's junction which hardly can be described analytically. Numerical simulations utilizing the finite element method (FEM) have proven more accurate. Similar to the hydraulic resistance study, the FEM analysis is conducted by using the in-program FEM solver in Solid Works. Its features and key elements to acquire correct results are stated within the following subsection.

Table 11: Notched tube's allowable elongation

Parameter	**Worst case normalized by the actuator's expansion Δl_{Act} [-]**
Actuator expansion	1
Fitting	0.22
Welding displacement	0.33
Manufacturing tolerances	0.04
Safety margin	0.11
Maximal allowable elongation of notched tube	0.29

4.3.1 Implementation

Similar to the CFD study, the FEM simulation provides a great dependency on the implemented boundary conditions of the considered problem, as well as on the implemented mesh of finite elements. First simulations utilizing the FEM solver have demonstrated large deviations of the maximal occurring stresses depending on the type and precision of the implemented mesh. Therefore, for this simulation a mesh consisting of second order tetrahedron elements is eventually implemented [30]. These elements provide a high accuracy while keeping the computational time within an acceptable range. The implementation is conducted by utilizing a mesh which iteratively adapts in order to meet a defined convergence criterion. This feature is called h-adaptive and basically refines the mesh at areas of high occurring stresses by running iterative simulations. "h" herein, defines the diameter of the enveloping circle around the finite elements [30]. However, reaching the convergence criterion can cost high computational power if the starting mesh is chosen inadequate. Therefore, a starting mesh is implemented which already refines its cells at small scale geometric features from the CAD model, such as the notch. Both, the starting mesh as well as the final mesh after the last iteration are pictured by figure 29. For an exemplarily simulation the corresponding course of convergence until reaching the

defined criterion of 96 % is also displayed by figure 30. All conducted simulations are implemented following this described scheme and hence all calculations provide a similar graph of convergence for the eventually obtained solution.

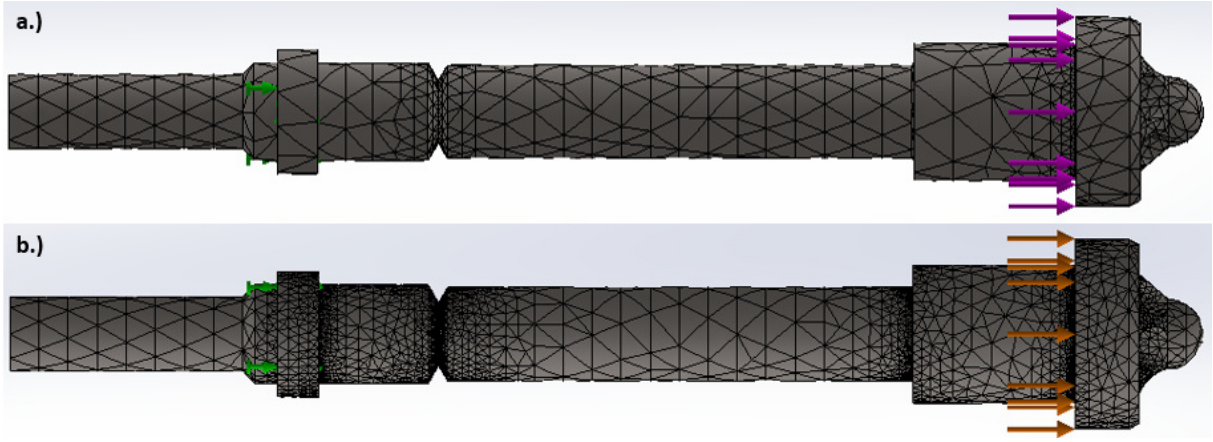

Figure 29: Implemented meshes for FEM simulation: a.) refined starting mesh; b.) iterated h-adapted mesh

The mentioned second aspect which needs to be considered is the correct and realistic implementation of boundary conditions. The defined boundary conditions for this very problem are also presented in figure 29 above. It is visible, that the actuator's force is implemented as force attacking at the entire contact surface area on the right. To picture the correct clamping behavior at the weld seam in the front part of the tube, a dummy housing is implemented at this area. The housing is defined fixated and firmly attached to the notched tube's outer surface. By implementing the explained principles, the following results for the novel NO notched tube are obtained.

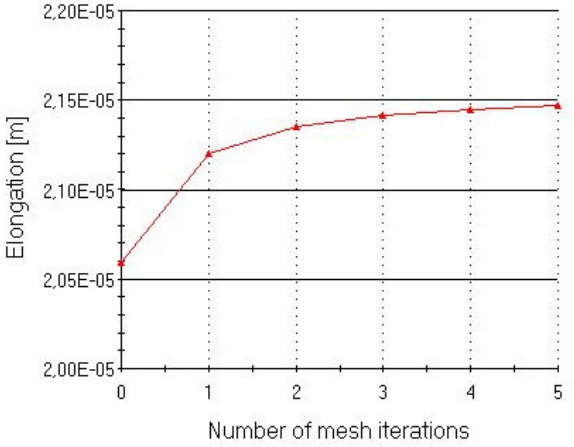

Figure 30: Exemplarily convergence of FEM simulation utilizing an h-adaptive mesh

4.3.2 Results

In order to validate the results obtained by the FEM study for the NO SMAV, a similar study is conducted for the notched tube of the normally closed valve. Those results again are compared to the tensile stress experimental investigations on the NC notched tube. For each tube, the FEM study is executed four times, each time applying a different force. One of these forces, $F_{NC,rupt}$ particularly constitutes the average force at which the NC notched tube broke during tensile stress tests. By conducting the study for different forces, a graph can be obtained giving the tube's elongation behavior dependent on the applied force. The graph's gradient is called the stiffness and is defined as following:

$$k = \frac{F}{\Delta l} \tag{4.38}$$

Herein Δl constitutes the notched tube's elongation. The following figure 31 shows the contoured results of the NO notched tube's elongation for an applied force of $F_{NC,rupt}$.. By evaluating the dark red area on the right at the poppet and likewise the dark blue area on the left, it is clearly visible, that only the part between the fixated boundary condition and the area where the force attacks, is subject of a deformation. Considering the large gradient at the notch, it is evident, that the notch elongates the most. This meets the expected behavior well. The figure presents a maximal elongation of $\Delta l_{NO,rupt} = 0.23 \cdot \Delta l_{Act}$ for the average rupture force.

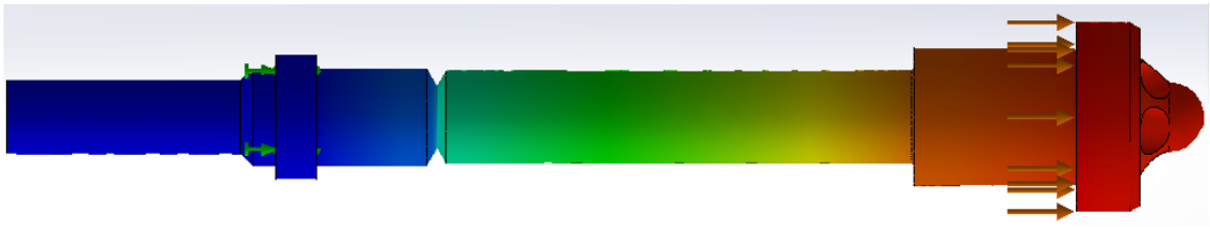

Figure 31: NO notched tube's elongation for $F_{NC,rupt}$

The relation between the applied force and the notched tube's elongation is illustrated by figure 32. This figure further presents the FEM results of the NC notched tube too. It can easily be seen that the NC tube provides a about 10.3 % greater stiffness k_{NC} than the NO variant k_{NO}. The lower stiffness of the NO tube can be explained considering its smaller hydraulic diameter and thinner wall thickness compared to the NC variant. However, the reinforcement of the tube at the poppet junction in order to enable the spring's implementation, results in a valuable stiffening effect. With the determined elongation of the NO notched tube of $0.23 \cdot \Delta l_{Act}$, the correct working point of the original actuator is ensured and the above stated requirement is fulfilled. In fact, a final safety margin of about $0.17 \cdot \Delta l_{Act}$ can be stated. Furthermore, comparing the novel FEM results to former tensile stress test results of the NC tube, the FEM analysis approximates the elongation always slightly greater than it occurs in reality. Hence, the real elongations at the rupture force also for the NO notched tube would probably yield about 15 % less than $\Delta l_{NO,rupt}$.

Worth mentioning considering the plot from figure 32 is, that the FEM simulation does not enable a simulation of the rupture. Therefore, the elongation values above the indicated rupture force constitute only hypothetical values if no rupture would occur.

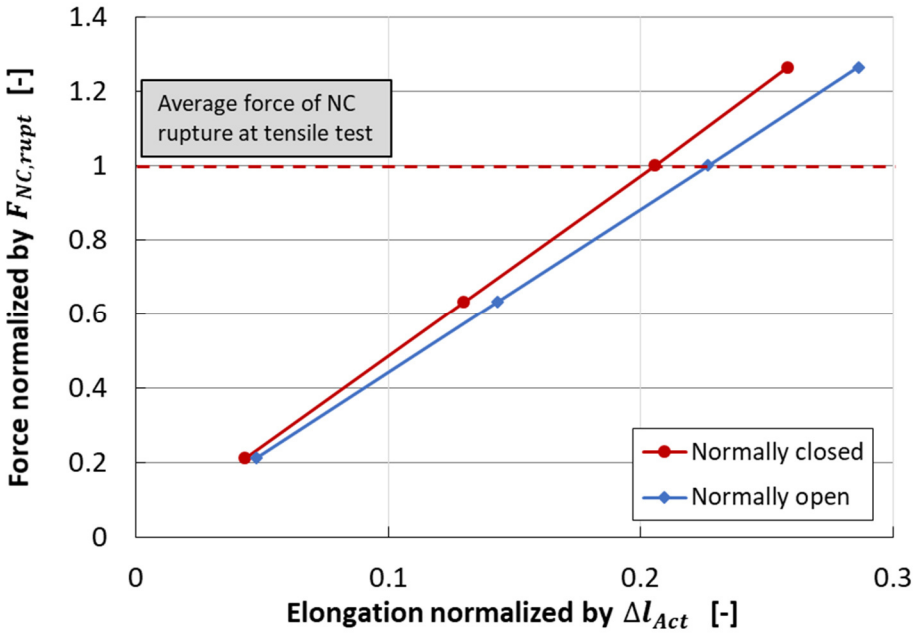

Figure 32: NO and NC notched tube's stiffness

4.4 Prototype design

The previous chapters have outlined the necessary optimizations on the SMAV NO design in order to meet all revised requirements. This subsection now presents the final prototype design after implementing those changes. To prepare engineering drawing usable by the Ariane Group's production, the above validated model is novel implemented within a CATIA environment. Figure 33 and figure 34

present sectional views onto the prototype at an open and respectively closed state. Compared to the SMAV NC, the NO valve provides great similarity as intended. Furthermore, only one external procured component – the spring – and three novel designed parts – the notched tube, the rear housing and the stopping ring – need to be developed and investigated. The corresponding three engineering drawings are prepared during this project and include a full tolerance and fit analysis. Further, all interface drawings regarding the assembly of the valve are prepared too. By collaboration with experts from Ariane Group, the proposed design by Lux of implementing an additional PTFE ring to improve the notched tube's glide behavior is rejected. Instead, the length of the glide surface is enhanced and the front edge is chamfered to prevent fretting and wedging. Its roughness is significantly smoothened. The partially increased wall thickness of the notched tube provides additionally stabilization. The positioning of the notch which was proposed by Lux has been evaluated reasonable for the reasons he outlined [9]. Hence, the notch is located as close as possible towards the weld seam of the notched tube while preventing thermal influences on the notch. According to the NC design, an additional E-type undercut is implemented at the NO notched tube as well, which is intended to decrease potential stress concentrations at the tube's stopping edge.

Further, the following table provides an overview over all component masses of the SMAV valve. These masses are determined by utilizing the CATIA mass function. A cost estimation of novel designed parts is conducted by referring to the corresponding engineering drawings.

Table 12: NO SMAV prototype weight and cost estimation per piece

Component	Material	Quantity	Weight [% NC]	Cost [€]
Upper clamp	Ti-Al alloy	2	n/a	n/a
Lower clamp	Ti-Al alloy	2	n/a	n/a
Elastomeric insert	n/a	2	n/a	n/a
Heater	n/a	1	n/a	n/a
Actuator	Nitinol	1	n/a	n/a
Front housing	Ti-Al alloy	1	n/a	n/a
Rear housing	n/a	1	10% NC	Similar NC + coating
Notched tube	n/a	1	12.8% NC	Similar NC
Stopping ring	n/a	1	0.3% NC	< 20 €
Spring	Spring Material B	1	6.7% NC	< 5 €
		Total:	105% NC	n/a

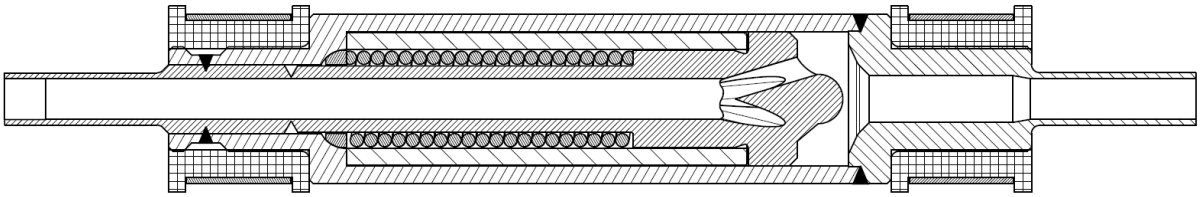

Figure 33: NO SMAV prototype design at unactuated open state

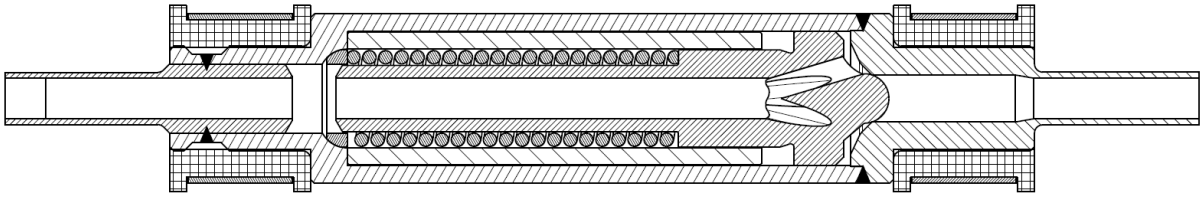

Figure 34: NO SMAV prototype design at actuated closed state

5. Seal design and investigations

As mentioned earlier within this thesis, Radermacher determined two potential seal designs which are most promising to fulfil the stated requirements. However, due to a lag of timing, he could not reproduce his first experimental results. Furthermore, as described within chapter 3, the requirements have been reconsidered and the seal must now meet novel criteria.

Thus, it is the objective of this section, to identify the best alternative of the two proposed seal designs by validating Radermacher's results and further to determine the sealing's capability to comply all new requirements such as an applied reverse pressure gradient. In case of insufficiency of fulfilling those requirements, optimizations to test procedures and the seal design itself are made.

5.1 Specimen design

The current two designs basically base on the same principle of creating a leak tight form closure by deforming a soft sealing partner plastically by pressing it onto the hard sealing partner. A classification into the broad range of seal design can be found in 2.3. In detail, the designs are presented in the following, as well as introductory a determination of the acting forces.

5.1.1 Force balance

Beforehand the final specimen geometry can be determined, it is necessary to identify and estimate all involved forces. However, the seal is intended to operate adequately not only at one constant pressure, but rather throughout the entire pressure domain which includes a reverse pressure gradient. Therefore, it needs to be distinguished between three extremal pressurization cases. These three cases are depicted in figure 35 below.

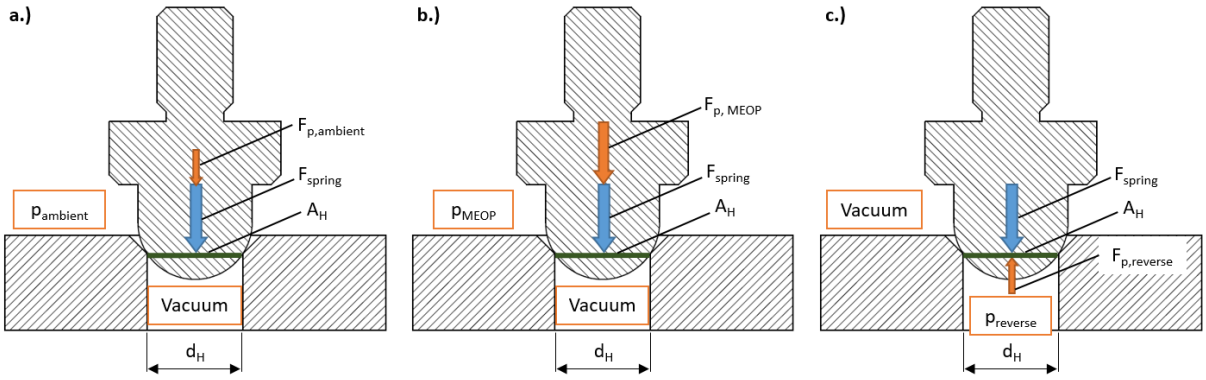

Figure 35: Seat-poppet pressurization cases: a.) Forward pressurization at low differential pressure; b.) Forward pressurization at MEOP; c.) Reverse pressurization

The pressurization case a.) represents the case of a very small pressure gradient between the inlet and the outlet. This case is applied when the seal is investigated on its sealing capability near atmospheric pressure of 1 bar GHe against the vacuum of the measurement line. Contrary, the second pressurization case b.) occurs for a maximal pressurization at the inlet at MEOP. The third case c.) shows the reverse pressurization at which a pressure is now applied at the former measurement line and the vacuum is generated on the former pressure side. This case not only constitutes a loss of the pressure caused sealing force, but furthermore this force now decreases directly the resulting axial sealing force. A_H constitutes the projected cross section of the through hole's hydraulic diameter and furthermore the approximated effective area, at which the pressure gradient acts. With the pressure domain stated in 3.1.3, the pressure related forces result to the following values for each pressurization case:

$$F_{p,ambient} = A_H \cdot p_{ambient} = \frac{\pi}{4} \cdot d_H^2 \cdot p_{ambient}$$
$$F_{p,MEOP} = A_H \cdot p_{MEOP} = \frac{\pi}{4} \cdot d_H^2 \cdot p_{MEOP} \quad (5.1)$$
$$F_{p,reverse} = A_H \cdot p_{reverse} = \frac{\pi}{4} \cdot d_H^2 \cdot p_{reverse}$$

A more detailed look on the acting forces, reveals figure 36. It shows that the axial force, causes a normal force on the actual sealing line. Hereby the angle α/2 is defined as the angle between the vertical axis and the tangent at the hypothetical infinitesimal contact *point* of the poppet and the seat's inner edge. $d_H$constitutes the hydraulic diameter of the flow path and r_P is the poppet's radius.

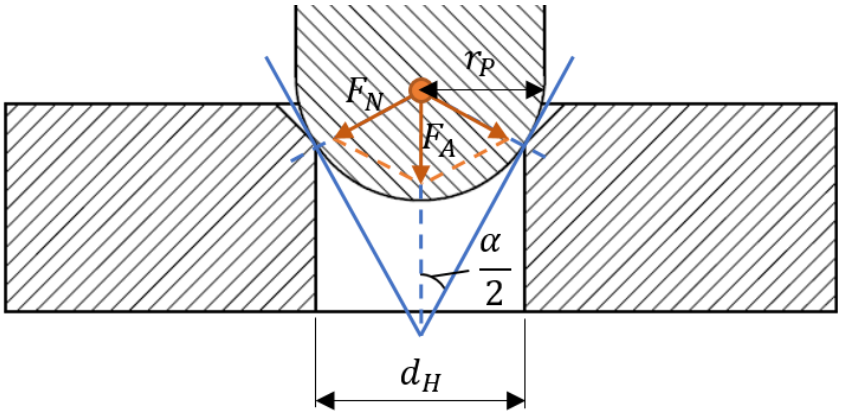

Figure 36: Normal and axial sealing forces acting onto seal seat and poppet

Utilizing the given geometric relations, the normal force on the sealing line is given by:

$$F_N = \frac{F_A}{2 \cdot \sin\left(\frac{\alpha}{2}\right)} \quad (5.2)$$

The angle α/2 then follows to [10]:

$$\frac{\alpha}{2} = cos^{-1}\left(\frac{d_H}{2 \cdot r_P}\right) \quad (5.3)$$

Inserting equation (5.3) into (5.2) then the normal force on the inner edge can be calculated as a function of the axial force:

$$F_N = \frac{F_A}{2 \cdot \sin\left(cos^{-1}\left(\frac{d_H}{2 \cdot r_P}\right)\right)} \quad (5.4)$$

From (5.4) it can be seen that F_N reaches a maximum for a certain F_A, when its denominator minimizes. The substitution of $x = \frac{d_H}{2 \cdot r_P}$ and the following differentiation of the denominator for x, results to:

$$\frac{d}{dx}\left(2 \cdot \sin\left(cos^{-1}(x)\right)\right) = \frac{-2 \cdot x}{\sqrt{1 - x^2}} \quad (5.5)$$

This shows that the denominator of F_N (5.4) reaches a maximum for $x = 0$ and reaches a minimum for:

$$\lim_{x \to 1}\left[\frac{-2 \cdot x}{\sqrt{1 - x^2}}\right] = -\infty$$
$$\lim_{x \to 1}\left[2 \cdot \sin\left(cos^{-1}(x)\right)\right] = 0 \quad (5.6)$$

This yields the important conclusion that the resulting normal force on the seal increases for a given axial force, when the ratio of poppet diameter to hydraulic diameter converges against a value of 1.

Wollner and Radermacher estimated the width of the sealing surface section with $w = 0.05\,mm$ [10][11]. Thus, the sealing area, not to be mixed up with the projected area A_H, results to:

$$A_s = \frac{\pi}{4} \cdot ((d_H + 2w)^2 - {d_H}^2) \tag{5.7}$$

With the above determined normal force from (5.4), the resulting approximated surface pressure on the seal, which forces the softer sealing partner to deform, then follows to:

$$p_s = \frac{F_N}{A_s} \tag{5.8}$$

Even if this surface pressure is only an approximation including the rough estimation of a perfect circular sealing surface with a very certain width, it is a valuable parameter to evaluate the required forces if a given material dependent yield strength needs to be reached for a plastic deformation.

5.1.2 Variant I: Hard metal seat – soft metal poppet

The first combination of poppet and seat Radermacher proposed, consists of a seal seat made out of a hard metal alloy (material I.A). Its counterpart, the poppet constitutes the soft sealing partner and is made out of an alloy of higher purity of the same basic material (material I.B). The corresponding material properties are listed in table 13. It is intended, that the poppet will deform under the sealing pressure plastically in form of the sealing line. Considering values given by table 13, it can be seen, that the required surface pressure (p_s from equation (5.8)) for a plastic deformation must exceed the value of the yield strength of the soft sealing partner: 180 MPa).

An engineering drawing of variant I is presented at figure 37. Radermacher chose the poppet diameter to be 20 % larger than the hydraulic diameter of the seat d_H. This way a narrow circular sealing line at the seats inner edge is created similar to a Tri-Point seat. The advantageous of this design are its simple geometry and its decent manufacturing effort as no additional manufacturing steps as polishing or coating are necessary. However, a major drawback of this version is its high required sealing force, as the soft metal still is much harder than e.g. a PTFE. Radermacher investigated this design experimentally and could gain the following results: Variant I demonstrated a good sealing capability with an average leakage rate of $2.05 \cdot 10^{-2} \cdot \Phi_{req,OP}$ throughout the pressure domain $(0 - 0.9 \cdot MEOP)$. However, he determined a required axial preload force of $1.34 \cdot F_{s,max,1}$, which greatly exceeds the installable spring forces. That is why, variant I needs to be optimized to qualify it for a further investigation. A design iteration is made in the following.

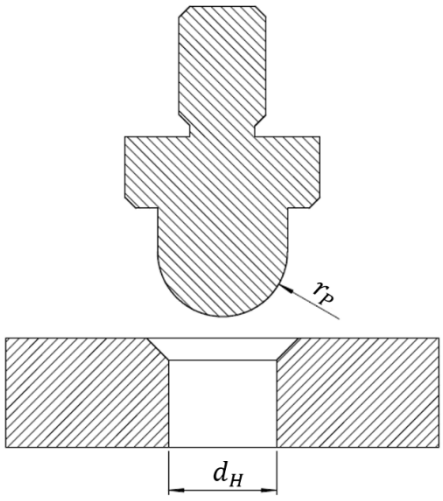

Figure 37: Seat & poppet variant I

Table 13: Mechanical properties of considered metal alloys [31]

Metal alloy	Component	Hardness	Tensile strength	Yield strength	Ultimate Strain
I.A	Poppet	120 HB	290 MPa	180 MPa	30%
I.B	Seat	310 HB	900 MPa	830 MPa	8%

Design iteration: Variant I.I

The leakage rate of variant I has proven almost 2 orders of magnitudes better than the leakage requirement. However, an optimization is necessary in order to reach this leakage rate at a lower axial sealing force than $F_{s,max,1}$. To reduce the required axial force while applying the same resulting surface pressure, the stated relations from section 5.1.1 can be utilized. By reducing the poppet's diameter in relation to a constant hydraulic diameter the axial force can be decreased while obtaining the same normal force to close the seal. Therefore, using equation (5.4), the required normal force can be calculated to $F_N = 1.21 \cdot F_{s,max,1}$. According to (5.8) this results to a surface pressure of 217 MPa, just above the yield strength value of table 13 to reach the plastic deformation of the poppet. Maintaining this surface pressure and by adding an additional margin, F_A is chosen to be below $0.9 \cdot F_{s,max,1}$. By inserting F_N and F_A into equation (5.4) and solving for r_P, a new maximum poppet diameter r_P' can be determined. For this diameter the preload requirement should theoretically be fulfilled. The iterated poppet and seat geometries yield according to figure 38.

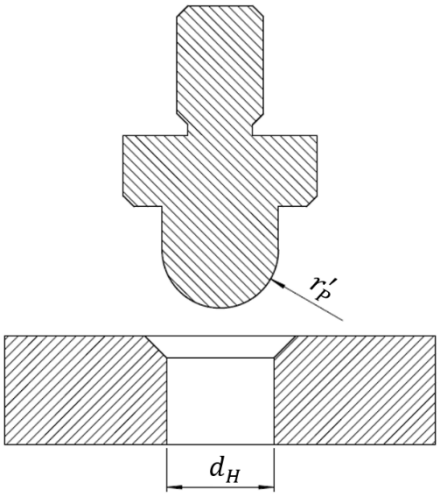

Figure 38: Seat & poppet variant I.I

In the course of this thesis variant I.I design will be investigated experimentally. The test results are presented later in section 5.5.2.

It has to be mentioned at this point, that this reduction of the poppet diameter not yet considers the third pressurization case from figure 35. This arises from, as previous tests only considered the pressurization cases a.) and b.). Case c.) was not considered in the course of previous theses and would again increase the required axial preload force.

5.1.3 Variant II: Hard metal poppet – soft metal coated seat

In the course of previous theses on the development of a leakage free poppet and seat combination, this second variant was determined to provide a great potential to meet the requirements. Geometrically, this variant does not differ from variant I seen in figure 37. However, other materials are used in order to further decrease the preload and increase the leak tightness. This variant features a poppet made out of the harder metal alloy from variant I, material I.A (therefore also referred to as material II.A), which makes it easier to process than the softer material I.B. The seat also is made out of I.A and thus provides the same advantageous for manufacturing. However, to achieve a sealing combination consisting of a soft and hard sealing partner, the seat is coated with a layer of a softer metal (material II.B) which provides a sufficient compatibility to all considered propellants. By considering three different key factors, the minimal required layer thickness of the material B's coating can be determined and is referred to as $\delta_{II.B}$.

The major influence on the thickness was evaluated by Wollner to be the material loss due to corrosion by aggressive fluids. Until the EoL of the valve, this value is estimated on the basis of a material compatibility research to be around $0.33 \cdot \delta_{II,B}$ [11]. A second influencing aspect results from the manufacturing tolerances of poppet and seat. Both, the poppet's and the through hole's diameter of the seat are tolerated by $0.15 \cdot \delta_{II,B}$. These tolerances can cause a deviation of a perfectly circular sealing line as both components could theoretically degenerate to ellipses considering their projected shape. To determine the required layer thickness, the worst case must be analyzed. The worst case is given if the tolerances are fully exploited for both parts and furthermore if the major axes of the resulting ellipses are perpendicular to each other. Figure 39 shows a sketch of this case and marks the resulting tolerated area. The thickness of this area gives the required layer thickness to compensate the manufacturing tolerance sufficiently and thus yields additional $0.33 \cdot \delta_{II,B}$.

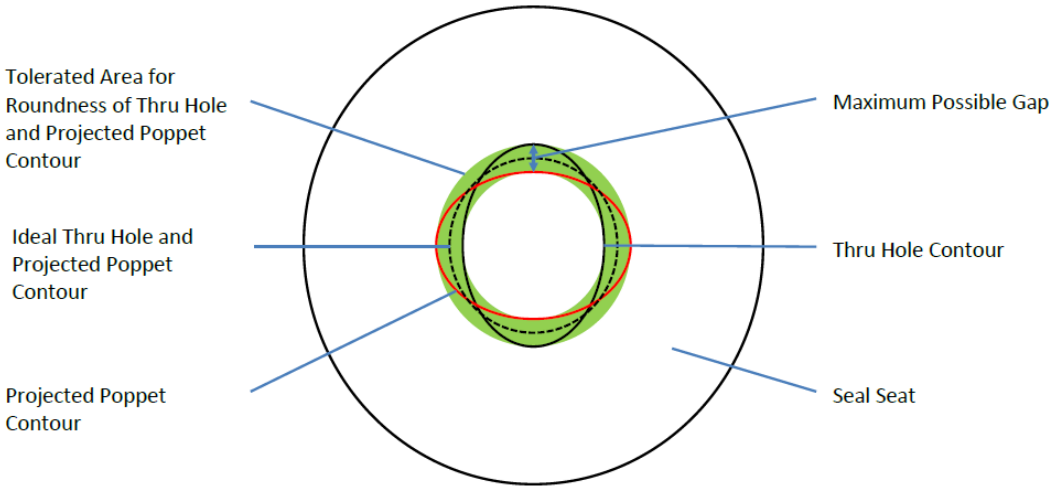

Figure 39: Maximum sealing gap due to circularity tolerances of seat and poppet [10]

The third factor which needs to be considered determining the minimal coating layer thickness, constitutes an additional margin of another $0.33 \cdot \delta_{II,B}$ to enable potential material removing post processing of the surface such as polishing or lashing. Hence, the overall layer thickness of the coating is determined to be $\delta_{II,B}$. Based on a supplier trade off [10], an external coating company was chosen which is able to plate the metal seats with this softer II.B layer. The coating process bases on two separated processes. When material I.A is exposed to air which comprises oxygen, immediately a protective Oxide layer forms at the surface. This makes a direct galvanic coating of the seat impossible as the plating layer would not adhere to the base material. Therefore, an intermediate process using the physical vapor deposition method (PVD) is required to apply an adhesive layer. This layer consists also of material II.B and provides a thickness of $0.01 \cdot \delta_{II,B}$. Subsequently, the main plating layer can be applied by galvanic bathing. An engineering drawing of the seat and its coating layer can be seen in figure 41 a.).

In the course of previous tests, a post processing of the coated surface was determined as overall important for sufficient sealing results. The coated layer shows a very rough surface with many randomly spread bumps and grooves. To close all leakage paths the poppet needs to deform those irregularities plastically. The greater the bumps and grooves the higher yields the required surface pressure for this deformation. Therefore, the best results at the lowest sealing forces have been obtained for a polished and pre-coined sealing line. The polishing of the surface decreases its roughness drastically and thus removes most of the bumps and grooves. An additional pre-coining is conducted to further decrease the required preload force while increasing the leak tightness. During the pressing of the poppet onto the seat's edge, the poppet forms the coating layer into its exact spherical form as like a stamp. Furthermore, the II.B layer adopts the poppet's higher surface quality. If this coining process is conducted in advance of the sealing test, the force required for this deformation can be conserved during the test. Therefore, the seat should be pre-coined with a certain load to press the poppet's spherical contour into the seat's sealing line. A detailed description of each process can be found in chapter 5.4.1 and pictures of the surface after each process step are presented in figure 40.

This variant has already demonstrated a good sealing capability at previous tests with an average leakage rate of $6.38 \cdot 10^{-2} \cdot \Phi_{req,OP}$ at an axial preload of $0.52 \cdot F_{s,max,1}$ [10]. This states the reason, as this variant will be investigated experimentally further in the course of this thesis to validate the first gained results. However, also two optimized designs of this version are developed and will also be subject of the envisaged tests.

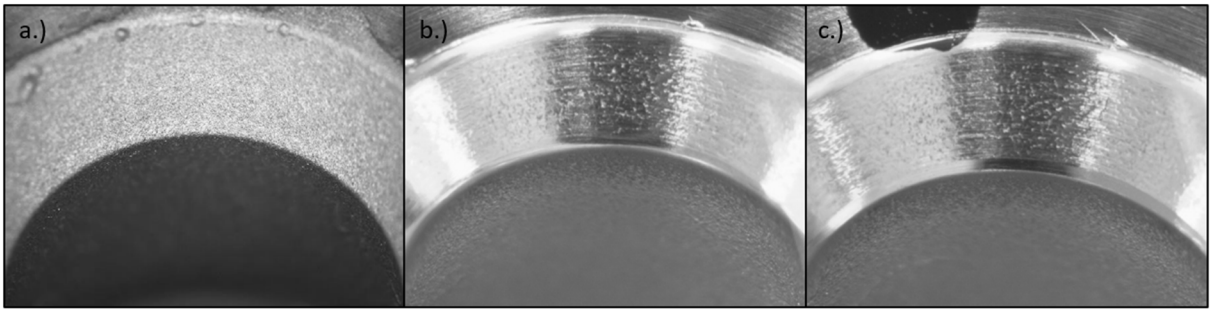

Figure 40: Specimen variant II: a.) unprocessed surface [10]; b.) polished surface; c.) polished surface and pre-coined sealing line

Design iteration: Variant II.I

To further improve the sealing capability and reduce the required axial preload force, a similar design iteration as for variant I.I is conducted. By remaining the seats geometry, as well as the coating and processing procedures as described for variant II, the poppet's diameter is reduced according to figure 38. Applying the principles stated in chapter 5.1.1, the surface pressure can be maintained constant while reducing the required axial force. The required axial preload of variant II was determined to be $0.52 \cdot F_{s,max,1}$ [10]. Hence the corresponding surface pressure for a sufficient form closure of this material combination can be calculated:

$$A_{s,II} = \frac{\pi}{4} \cdot ((d_{H,II} + 2w)^2 - {d_{H,II}}^2) \tag{5.9}$$

$$F_{N,II} = \frac{F_{A,II}}{2 \cdot \sin\left(cos^{-1}\left(\frac{d_{H,II}}{2 \cdot r_P}\right)\right)} = 0.47 \cdot F_{s,max,1} \tag{5.10}$$

$$p_s = \frac{F_{N,II}}{A_{s,II}} = const. \tag{5.11}$$

With the same seat's hydraulic diameter $d_{H,II} = d_{H,II.I}$ both the area of the sealing line, as well as the corresponding normal force remain constant compared to variant II: $F_{N,II} = F_{N,II.I}$. However, the ratio of hydraulic diameter to poppet diameter changes from 83.3 % to 92.5 %. Inserting this ratio into equation (5.10) the new required axial force can be calculated to:

$$F_{A,II.I} = 2 \cdot \sin\left(cos^{-1}\left(\frac{d_{H,II.I}}{2 \cdot r_{P,II.I}}\right)\right) \cdot F_{N,II.I} = 0.36 \cdot F_{s,max,1} \tag{5.12}$$

$$\frac{F_{A,II.I}}{F_{A,II}} = \frac{0.36 \cdot F_{s,max,1}}{0.52 \cdot F_{s,max,1}} = 68.4\,\% \tag{5.13}$$

This ratio between the axial forces shows, that the reduction of the poppet's diameter theoretically reduces the required axial preload by 31.5 % to 36 % of the available preload by spring 1: $F_{s,max,1}$.

Design iteration: Variant II.II

Considering the results of the hydraulic resistance design study from chapter 4.1, a larger seat's through hole has proven more efficient to reduce the valve's pressure drop rather than a smaller poppet diameter as design variant II.I provides. Applying the principles from chapter 5.1.1 again, the seat's hydraulic diameter can be enlarged to decrease its pressure drop while also decreasing the required axial preload onto the seal by maintain the original poppet's diameter. As calculated above at equation (5.11), the experimentally determined surface pressure onto the seal to achieve a leak tight form closure for this material combination needs to be reached.

On the first hand and according to equation (5.7), increasing the hydraulic diameter also increases the sealing area A_s and thus decreases the surface pressure p_s. This decrease of the applied surface pressure needs to be compensated by increasing the normal force:

$$A_{s,II.II} = \frac{\pi}{4} \cdot ((d_{H,II.II} + 2w)^2 - {d_{H,II.II}}^2) = 1.14 \cdot A_{s,II} \tag{5.14}$$

$$F_{N,II.II} = p_s \cdot A_{s,II.II} = 0.54 \cdot F_{s,max,1} \tag{5.15}$$

This increased required normal force however, does not imply necessarily that the axial force also increases, as it also depends of the ratio between poppet and hydraulic diameter:

$$F_{A,II.II} = 2 \cdot \sin\left(cos^{-1}\left(\frac{d_{H,II.II}}{2 \cdot r_{P,II.II}}\right)\right) \cdot F_{N,II.II} = 0.33 \cdot F_{s,max,1} \tag{5.16}$$

$$\frac{F_{A,II.II}}{F_{A,II}} = \frac{0.33 \cdot F_{s,max,1}}{0.52 \cdot F_{s,max,1}} = 64.4\,\% \tag{5.17}$$

By the implementation of this design iteration II.II, theoretically a 35.6 % lowered axial sealing force can be obtained while also decreasing the valve's pressure drop significantly. These advantageous state the reasons that this design iteration will be focused on during the following experimental investigation. An engineering drawing of this variant is illustrated by figure 41 b.). The surface post-processing as described for variant II will be applied the same way for this iterated design.

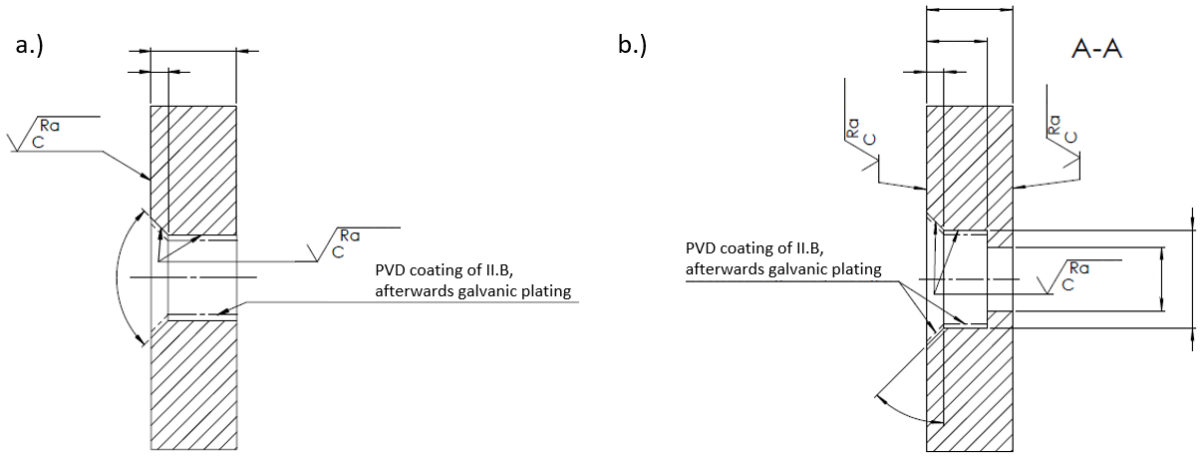

Figure 41: Engineering drawings of coated seal seats: a.) variant II; b.) variant II.II

5.2 Test facilities

This subsection describes the test jigs which are used for the envisaged tests. Previous investigations by Radermacher and Wollner on the seal have shown, that the currently used test jig provides some major disadvantageous which even probably influenced former test results [10][11]. Furthermore, the current test jig is not be able to perform reverse pressurization tests [10]. This is later discussed in greater detail. Nevertheless, these are the reasons, why a development of a novel test jig was indispensable. However, to determine further development steps, a validation of previous test results is necessary soon after the beginning of this thesis. Hence, the existing jig has to be used to implement the first tests and thus is described in the following paragraphs

5.2.1 Forward pressure leak testing device

The current jig which was used for the previous leakage rate measurements of the SMAV NO is presented in figure 42. The jig comprises of 4 plates and one cylindrical pressure vessel. By turning the external force adjustment screw on the top, an axial force can be applied on the poppet, which then gets pressed onto the valve seat. To represent a realistic behavior according to the valve's design, the force is transduced by compressing a spring. Between spring and adjustment screw, an implemented load cell [32] enables the internal measurement of the applied force. Avoiding a pressure gradient between the seal and the load cell, small venting holes are implemented to pressurize the entire upper part of the jig. As described later within chapter 5.4 in greater detail, the seal seat is mounted on the bottom plate of the jig and right above the poppet is implemented into a self-centering poppet holder. The pressure of gaseous Helium is applied from the marked lateral inlet port on the right, and a vacuum generating mass spectrometer is connected to the outlet port. A further description of the test's fluid plan and all involved measurement methods are presented in 5.2.2.

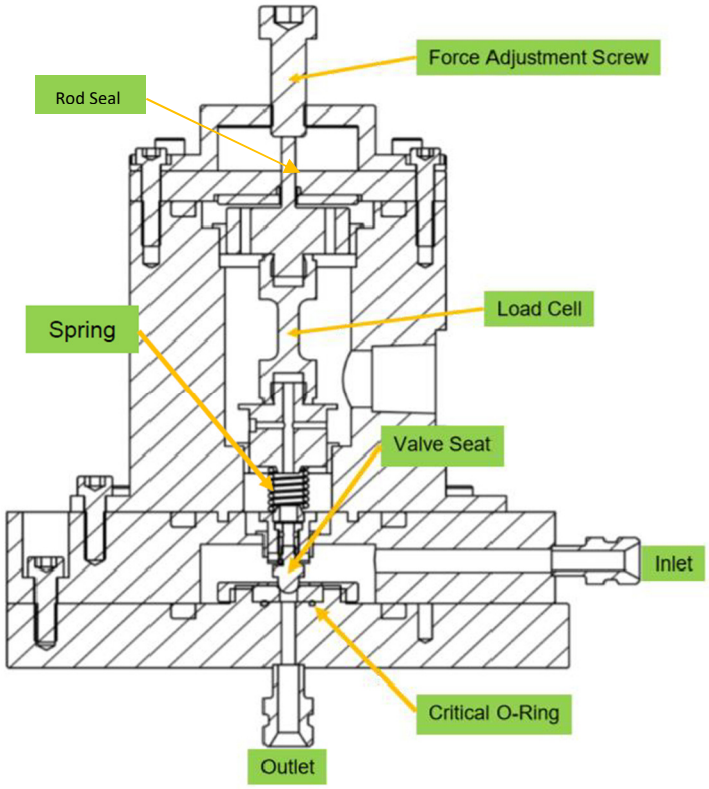

Figure 42: Forward pressure test jig – derived from [33]

Even though the test jig served its purpose well to identify potential poppet and seat combinations out of a variety of variants, it provides some critical drawbacks:

O-Ring Permeation:

As it is indicated in figure 42, the measurement line is sealed towards the high pressure side just by using one small elastomeric O-ring (12 x 1.5 mm, Shore A 70, NBR). Although macroscopically treated, such an O-ring is a sufficient sealing for high pressure applications as technically there is no pressure decay detectable on the high pressure side, but it is not well suitable for applications where a microscopic measurement on atomic level is conducted on the low pressure side. Especially considering long term tests, elastomeric seals tend to a diffusion process called permeation [34]. The permeation process describes the process of gas dissolving into the seal's surface and continuously diffusing into the entire seal material over time. Eventually, gas which has entirely diffused through the O-ring, it evaporates again at the seal's surface at the low pressure side. Originating from there, it reaches the measurement line and is falsely detected by the mass spectrometer. The evaporating process is even increased, if additionally, the force on the O-ring and its resulting compression decreases over time. Considering the always higher leakage rates while decreasing the applied pressure, this very behavior can clearly be identified at previous [10] and novel implemented tests. In section 5.5.1, these results are presented, which show the dependency of the O-ring caused leakage due to exposure to Helium. Further within this thesis, this leakage rate will be referred to as *background leakage rate*.

Maximal pressurization

Besides the O-ring diffusion issue, furthermore the test jig was not designed to be used at a pressure of MEOP. Two circles of M6 and even one circle of M5 screws at the top would provide a far too low safety factor of 1.1 for this pressure. Additionally, to provide the lateral pressurization of the test jig, the bolt circle was interrupted by one screw. This way the screws experience an asymmetrical load profile which stresses some screws even more. This states the reason, because all measurements utilizing this jig cannot be conducted throughout the entire pressure domain but need to be aborted at 87% MEOP.

Reverse pressurization

Another drawback of this test jig is given, considering its design for only forward pressurization from the inlet port. A pressurization from the lower outlet port according to the novel reverse leakage rate requirement, would involve, that the entire upper part of the jig needs to be vacuumed by the mass spectrometer. However, the mechanism of the jig is based on the external force adjustment which implies the use of a seal for a translational movable rod. For the pressurized application this seal is simply implemented by a spring energized elastomeric C-seal (Variseal RVE00040 [35]). A schematic of the assembly and its pressurization can be found in figure 43. Previous investigations [10], extensive literature research and consultation by sealing suppliers yield that a sufficient sealing of a rod between atmosphere and vacuum proves quite difficult and results for most elastomeric seals in a decreasing quality of the vacuum over time. This however, would be highly not desirable considering the long term thermal cycling tests.

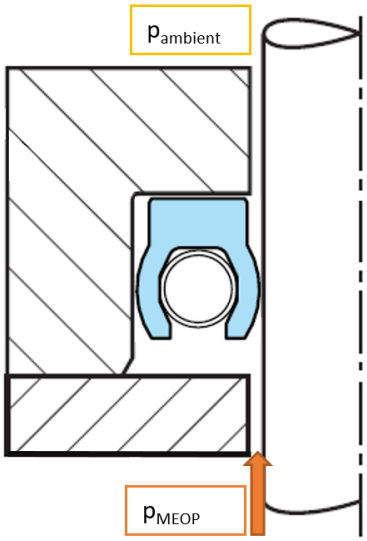

Figure 43: Rod sealing at MEOP pressurization case – derived from [35]

Considering all those aspects, it makes it reasonable to develop a novel test jig and to eliminate all stated drawbacks. This jig and its features are described in the following.

5.2.2 Optimized forward and reverse pressure leak testing device

The previous section exemplified the necessity of a novel test jig to enable less falsified measurement results for all application cases which need to be investigated. In the beginning of the development process, it is reasonable to conduct a concept trade off to quickly assess and evaluate different opportunities with their respective pros and cons. Therefore, a list of criteria, such as requirements are defined, which should be fulfilled by the new test jig as best as possible. The derived criteria are stated in the following table 14. On the right, the criteria are assigned to a weighting factor between 1 and 5, where 5 constitutes a most important key factor the new jig should provide inevitably and 1 represents a dispensable requirement if necessary.

Table 14: Criteria for test jig concept trade off

#	Criteria	Description	Weighting (1 – 5)
1	Reverse pressurization	Possibility of reverse leakage tests up to MEROP	5
2	Forward pressurization	Possibility of forward leakage tests throughout the entire pressure domain (1 bar – MEOP)	5
3	Force measurement	Measurement of the applied force internal of the jig	5
4	Force adjustment	Opportunity to adjust the applied force external of the jig stepwise during the test	4
5	Dynamic behavior	Simulation of the dynamic impact of the poppet after sudden release of a preloaded spring	2
6	Spring characteristic	Representing a realistic behavior according to the valve design	4
7	Long term usage	No permeation of GHe towards the measurement line over time	5
8	Thermal extrema	Ability to execute long term tests exposed to a thermal cycling environment	5
9	Sealing force	Required clamping force for used pressure and vacuum flange seals as low as possible	2
10	Seat/Poppet design	Applicability to use the current seat and poppet design to ensure to reproducibility compared to previous tests	3
11	Reusability	Reusability of components of the forward pressure jig; reusability of seals and actuator (if existent)	2
12	Costs	Costs for production, operation and external purchased parts	4
13	Manufacturability	Effort, time and complexity of production	2
14	External parts	Number of external procured parts and their delivery time	1
15	Handling	Usability during mounting and operation	3

Based on these requirements three concepts are developed and assessed later on. As, after the trade off, concept III is chosen for a detailed development, concepts I and II are only shortly introduced in the following. An overview of the rated criteria is presented in table 15.

Concept I: Dynamic concept using a SMA actuator

This test jig design is simply based on the actuation using an original SMA actuator of the SMAV. To reduce material consumption the actuator would break a small pin with a notch of the same geometry as the original notched tube. The rupture would release a preloaded spring which pushes the poppet onto the seat while it pushes against a load cell on the other side. This would enable both a truly realistic simulation of the dynamic poppet impact, as well as internal force measurements. The fact, that this concept does not feature an external force adjustment constitutes both advantage and disadvantage simultaneously. This way there is no translation rod which is needed to be fed through into a vacuum chamber and thus results in great simplicity. On the contrary it is not possible to adjust the force on the poppet once after test begin. The only way to adjust the force is by implementing different springs with different spring constants in between the tests. A further major drawback of the concept is the high operating costs, as the SMA actuators are only single use items. Concept I is illustrated by figure 44.

Concept II: Dynamic concept using a release mechanism and interface change

This design again bases on the abrupt release of the poppet as concept I. However, the expensive SMA actuator now is replaced by a cheaper spring activated release mechanism. The force measurement would be enabled by a load cell which is now placed below the seat. As a mechanism which cannot be activated by heating it up like concept I, a mechanical feed through to the outside of the test jig would be necessary to trigger the release. As there is no mechanical feedthrough available which provides a sufficient sealing capability for both a high vacuum (HV) and a pressurization up to MEOP, this would require a changeable interface for each case. A schematic drawing of concept II is presented in figure 45.

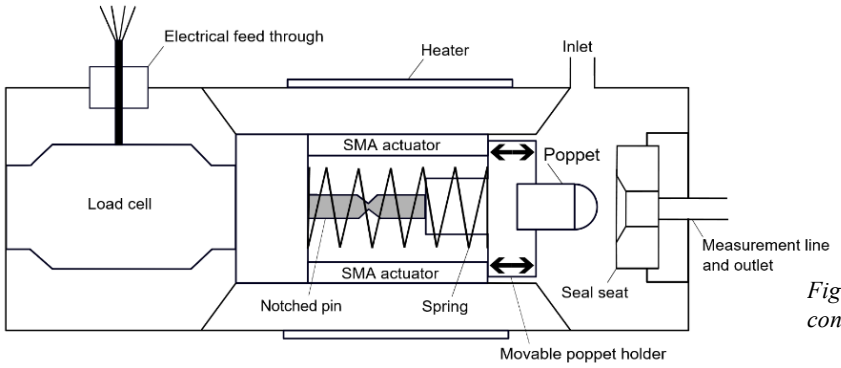

Figure 44: Schematic drawing of concept I for novel leak testing device

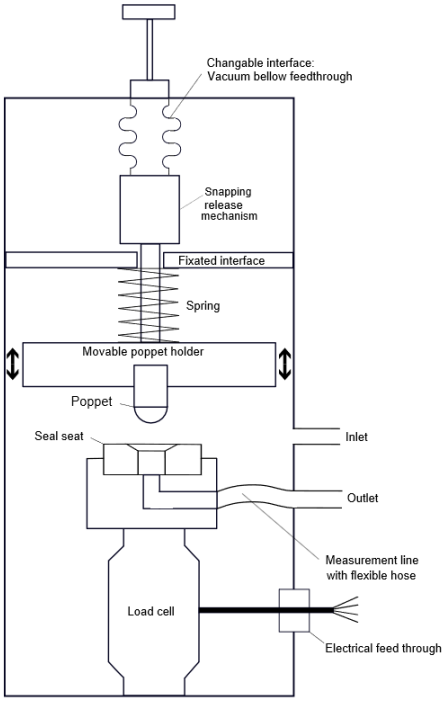

Figure 45: Schematic drawing of concept II for novel leak testing device

Table 15: Test jig concept trade off results

#	Concept I		Concept II		Concept III	
	Description	**Rating (0 – 5)**	**Description**	**Rating (0 – 5)**	**Description**	**Rating (0 – 5)**
1	Double sealing	5	Double sealing	5	Double sealing	5
2	inherent	5	After I/F change	3	After I/F change	3
3	Simple	5	Below seat, flexible	3	Simple	5
4	By spring change	1	By spring change	1	Inherent	5
5	Possible	5	Possible	5	Not possible	0
6	Similarity given	5	Similarity given	5	Similarity given	5
7	Metal seals	5	Metal seals	5	Metal seals	5
8	Possible	5	Possible	5	Possible	5
9	Copper flat seal	2	Copper flat seal	2	Copper flat seal	2
10	Possible	5	Possible	5	Possible	5
11	Single use actuator	0	Single use seals	3	Single use seals	3
12	Actuators	1	Two interfaces	4	Two interfaces	4
13	Low	4	High	1	Medium	2
14	Heater	4	Vacuum feedthrough	2	Vacuum feedthrough	2
15	Simply	4	Decent	3	Decent	3
	Total:	**206**	**Total:**	**193**	**Total:**	**211**

Concept III: Static concept using a force adjustment mechanism and interface change

The detailed evaluation of the three concepts above, determines this concept most promising to meet the most test jig requirements. Especially, considering the low TRL (Technology readiness level) of the seat and poppet combination as yet, a determination of the basic sealing capability and its required sealing force seems more important than the simulation of the dynamic impact. Besides the trade-off results, this is a decisive key factor for this concept.

This concept bases on the same force adjustment principle as the forward pressure test jig presented in 5.2.1. The poppet gets pushed onto the seat by an external adjustable mechanism. The force is transduced by a spring and measured by a load cell between spring and force adjustment mechanism. As shortly mentioned above, a critical component of the jig is its required mechanical feedthrough. This feedthrough must be translational movable and both pressure and vacuum tight against atmospheric pressure. Therefore, the development focuses on a jig at which the upper part can be switched and replaced depending on the pressurization application. Hence, two upper parts exist which include the respective linear feedthrough. The CAD model of the test jig with its two interfaces is shown in the following figure 46.

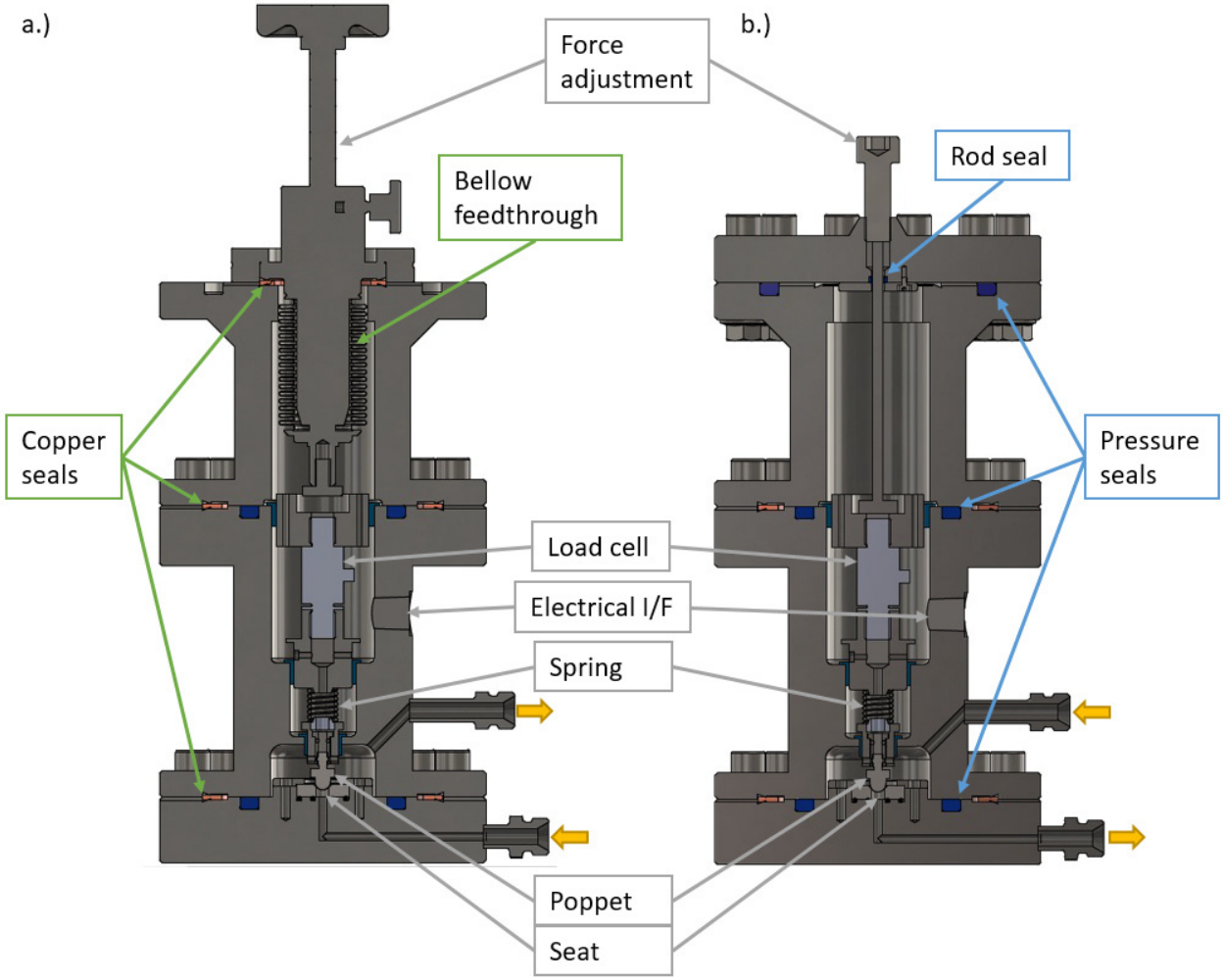

Figure 46: CAD model of novel test jig according to concept III: a.) Reverse pressure I/F; b.) Forward pressure I/F

As it can be seen, by relocating the pressurization ports, full bolt circles can be implemented at the new jig. Furthermore, all screw connections are calculation with a sufficient safety factor for MEOP. A full strength-calculation can be found in the following chapter, as well as its experimental validation in section 5.2.4. The switchable vacuum interface, seen in a.) enables the intended reverse leakage tests. All inner components of the jig are designed with venting holes, so that an applied pressure or vacuum expands throughout the entire upper part of the jig avoiding pressure gradient driven falsifications of the force measurements. The jig is developed following the former test jig concept and therefore enables the reusability of already existing components as e.g., the poppet holder, the load cell itself and its adapter, the glide bearings and the spring. Firstly, this features a great saving of manufacturing time and costs, and further enables the comparability to previous test results as the same spring and load cell are used.

Figure 46 a.) illustrates that the reverse pressure is applied from the lower port. At this case, the mass spectrometer is connected to the upper port and generates a vacuum throughout the upper part of the jig. Therefore, the flanges are sealed with cheap but highly effective copper flat seals according to CF vacuum flange norm [37]. Those metallic seals provide a UHV even throughout the entire temperature domain. The linear feedthrough for this vacuum application is implemented as a flexible metal membrane bellow. This bellow enables a translational movement while maintaining a HV inside the jig. Furthermore, this feedthrough is capable to apply a force of 150 N onto the poppet and provides a 50 mm stroke. A detailed specification can be found in table 16. A major drawback of the bellow feedthrough is its restriction to low pressures. Therefore, a second pressure interface (I/F) is needed, presented in figure 46 b.). During a forward leakage test, the pressure up to MEOP is applied from the upper port and the mass spectrometer now is connected to the lower outlet port. As spring energized elastomeric

seals [35] have proven very capable at the former forward pressure test jig, the same types are implemented for this application. Also, the rod seal at the feed trough can be reused from the former jig. Further it is worth mentioning, that the switch between the two configurations can simply be conducted by demounting the respective upper plate without disassembling the lower part of the jig and especially not the investigated specimen. Regarding a potential rotational twist by reusing and reassembling specimens, this gains importance. If poppet and seat would be reassembled even slightly twisted compared to a first test, potential deviations of the spherical, respectively the circular form could lead to an easy leakage path. By just switching the upper interfaces, this failure is eliminated.

One further concern of the former test jig was the background leakage by permeation of GHe through the critical O-ring between seat and measurement line. For the new test jig two concepts have been developed that should meet all in the following stated requirements:

- Seal the measurement line sufficiently by providing a leakage rate of 3 orders of magnitude better than the target leakage rate of the valve seal $\Phi_{req,OP}$
- Be applicable throughout the entire temperature domain without permeation
- Be applicable for long duration and thermal cycling tests without permeation
- Allow forward and reverse pressurization without disassembling the seat

According to the expertise of experts at Ariane Group, a simple concept of two concentrically elastomeric O-rings instead of one ring was proposed previously [10][11]. Herein, this concept is elaborated and designed in greater detail, finally evaluated and depicted in figure 48 presenting both pressurization cases. The concept bases on the implementation of venting holes between the O-rings. These holes provide a venting of the space between the rings with atmosphere at ambient pressure. In theory, this would result in a mixing of the permeated GHe atoms with atmospheric molecules and would eventually lead to the dissipation of Helium through the holes. Hence, the vacuumed O-ring would not be attacked by the Helium which permeates through the pressure exposed O-ring and the measurement line would be sufficiently sealed. However, at this early design phase it is not fully clear yet, whether the venting holes provide such a large impact on the partial pressure of the GHe concentration between the O-rings. Due to a restricted space, the holes must be chosen quite small compared to the O-rings' surface areas. Helium atoms mixed within a still air environment provide a motion according to the Brownian motion as seen in figure 47. This motion describes the irregular and undirected thermal movement due to collisions with other surrounding atoms and molecules [36]. Considering this and furthermore the larger surface area of the O-rings compared to the venting holes, it seems evident that not the entire partial pressure of GHe can be reduced to zero, but that a remaining proportion of atoms will penetrate even the second O-ring.

An estimation of this proportion which is dissipated through the first O-ring and eventually reaches the second O-ring would be quite rough and only statistical. Its accuracy would not be sufficient. This is why, it is decided to conduct experimental investigations on this atom motion behavior.

Due to these concerns, another sealing concept for the measurement line is developed by close collaboration with the sealing company HTMS located at Belgium. This design rejects elastomeric seals and therefore bases on metal seals. This fully eliminates the unwanted permeation through soft O-ring materials. However, as metal provides a harder surface, it is more challenging to reach the target leakage rate. Therefore, the surface roughness of the test jig's bottom plate and the seat's bottom side need to be largely decreased. This concept now bases on two concentrically metal C-rings. As they are pressure activated, C-rings provide the advantage of an increasing

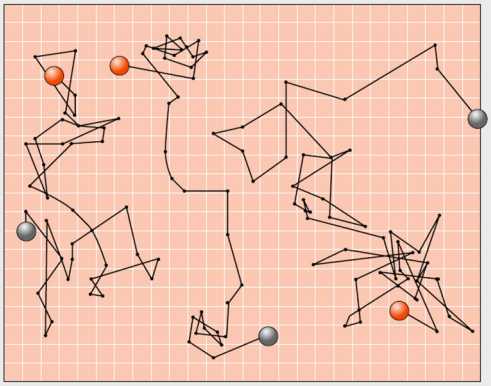

Figure 47: Brownian motion [36]

sealing capacity for increasing pressure. A sketch of the implementation can be seen in figure 49. Different to the previous concept, at which both O-rings permanently seal a certain pressure gradient, now only the pressure exposed C-ring is actively sealing while the other ring remains passive during an application. The active ring for the respective pressurization cases is indicated in figure 49 too. To increase the preload on the rings, it is decided to implement a spring energized and Silver-plated Inconel C-ring as the outer, external pressure ring. As the diameter of the inner ring is too small for a similar spring energized design, here a Tin-plated Inconel C-ring is implemented which additionally is solution annealed and precipitation hardened in advance.

As it is hardly predictable at this phase, which of the discussed sealing solution will provide better results, it is decided to manufacture both options and to evaluate the most suitable variant by investigating them experimentally within the further course of this thesis. The corresponding results on the background leakage rates are shown in section 5.5.1.

Concluding this subsection, a brief overview over all external purchased parts for the new jig can be found in the following table 16. Additionally, two exemplary engineering drawings of single components of the jig are attached at the appendix XI.I.

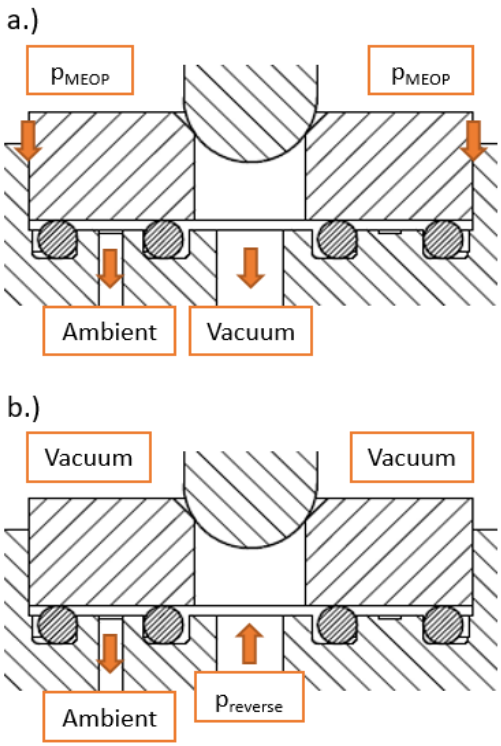

Figure 48: Seat sealing by concentrically O-Rings with venting holes: a.) Forward pressurization; b.) Reverse pressurization

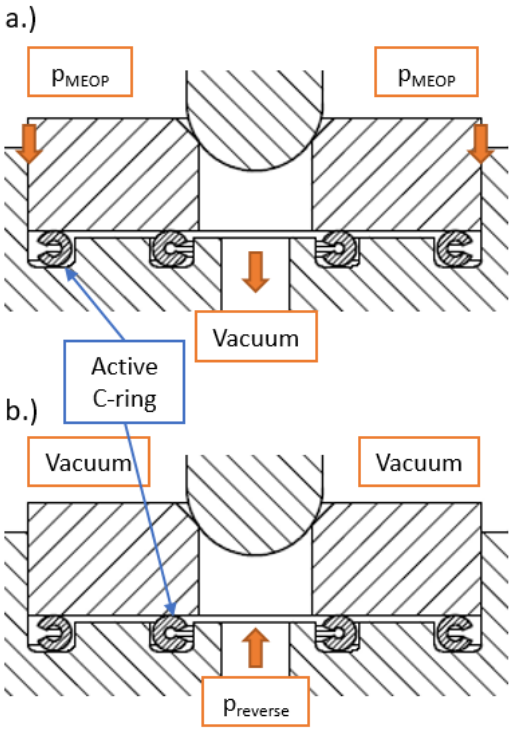

Figure 49: Seat sealing by concentrically C-rings: a.) Forward pressurization; b.) Reverse pressurization

Table 16: Specifications of components implemented in novel leak testing device

Component	Product	Pressure [bar]	Temperature [°C]	Other
HV bellow feedthrough	DN40 CF: PF 631 010 –T [38]	UHV to 0.5	Up to +300	50 mm stroke; 200 N axial load
Electrical feedthrough	WFS-R1/4"-24CU-4-V [39]	HV to 500	-60 to +200	4 AWG24 Cu wires for load cell
Load cell	XFTC 300 [32]	N/A	-40 to +120	Details see table 17
Copper Seals	DN 40 CF [38] DN 75 CF [38]	UHV to 1	-196 to +200	OHFC
Variseals	DVE300630-T05S [35] DVE300900-T05S [35]	1 to 4000	-150 to +200	Turcon material
O-Rings	ORAR00010-E7502 [35] ORAR00016-E7515 [35]	HV to 250	-45 to +150	Shore A 70
C-Rings	CI-000900-1.57H-2/0-4-SN50 [40] CSE-001615-1.57M-2/2-1-S50 [40]	UHV to MEOP	-50 to +90	Requires surface finish R_a=0.4

5.2.3 Analytical verification of novel leak testing device

Besides the considerations outlined above regarding the overall functionality, a full strength-calculation was a crucial aspect developing the novel leakage test jig. Particularly, all bolt connections require an analytical verification about their strength to withstand the occurring loads. Additionally, also the induced stresses into the pressure vessels' material need to be determined and evaluated regarding maximal allowable stresses. For a first design of the device, the bolt connections are chosen according to the norm of DN 75 CF for vacuum seals. All further geometries such as sealing diameters and wall thickness are chosen with respect to the given geometrical conditions.

Strength calculation of bolt connections

The safe operation of the novel test jig can only be ensured by dimensioning all pressurized bolt connections correctly. The driving factor hereby are the operating pressure and its area of attack at the jig's flanges. Due to functional aspects, two sizes of Variseals are implemented into the device. At the lower two bolt connections seals with an outside diameter of 63 mm are implemented. At the upper flange a seal with an outside diameter of 90 mm is chosen. As this results in a larger area of attack, the upper bolt connection has to withstand higher pressure induced forces. All essential input parameter for the following rough, but conservative dimensioning calculation are given by the following table 17. The corresponding output parameter are presented in table 18. A detailed strength calculation according to VDI 2230 is purposely not presented herein in order to keep the extent of this report manageable. To verify the simplified calculation, a proof pressure test is conducted and outlined in the following chapter.

Table 17: Input parameter for bolt strength calculation of novel leak testing device

Parameter	Symbol	Value	Unit
MEOP	p_{MEOP}	n/a	bar
Proof pressure	p_{proof}	n/a	bar
Screw nominal diameter	d_n	8	mm
Number of screws	n	12	-
Pitch	P	1.25	mm
Yield strength (12.9)	$R_{p0.2}$	1080	MPa
Outer diameter of Variseal	$d_{s,1}$	63	mm
	$d_{s,2}$	90	mm

With the given seal diameters and number of bolts, the forces applied to a single bolt can easily be determined:

$$A_p = \frac{\pi}{4} \cdot {d_{s,i}}^2 \tag{5.18}$$

$$F_p = A_p \cdot p_{MEOP} \tag{5.19}$$

$$F_{bolt} = \frac{F_p}{n} \tag{5.20}$$

The stress area or the chosen M8 bolts, which is the essential area of a screw to withstand an applied load, yields as follows:

$$d_{eff} = d_n - 0.64952 \cdot P \tag{5.21}$$

$$d_{root} = d_n - 1.22687 \cdot P \tag{5.22}$$

$$A_\sigma = \frac{\pi}{4} \cdot \left(\frac{d_{eff} + d_{root}}{2} \right)^2 \tag{5.23}$$

By comparing the applied stress per bolt with the maximal allowable stress, a safety factor can be calculated:

$$\sigma_{bolt} = \frac{F_{bolt}}{A_\sigma} \tag{5.24}$$

$$\mu = \frac{R_{p0.2}}{\sigma_{bolt}} \tag{5.25}$$

Table 18: Output parameter of bolt strength calculation of novel leak testing device

Parameter	Symbol	Bolt connection with $d_{s,1}$	Bolt connection with $d_{s,2}$	Unit
Area of attack	A_p	3117.2	6361.7	mm^2
Total force on flange	F_p	n/a	n/a	N
Force per bolt	F_{bolt}	n/a	n/a	N
Bolt stress area	A_σ	n/a	n/a	mm^2
Applied stress per bolt	σ_{bolt}	n/a	n/a	MPa
Safety factor MEOP	μ_{MEOP}	> 1.5	> 1.5	-
Safety factor proof pressure	μ_{proof}	> 1.2	> 1.2	-

This first dimensioning calculation demonstrates that all bolt connections provide a sufficient safety factor for both MEOP and proof pressure ($\mu_{MEOP,req} > 1.5$).

Tensile and compressive stresses in the pressure cylinders

The calculation method of the occurring stresses in a vessel which is pressurizes from the inside depends on its wall thickness. Stresses within a thin-shell pressure vessel require a different calculation than stresses occurring in a thick-walled pressure vessel. Vessels are considered as thick-walled, if the ratio of outer radius to inner radius exceeds the value of 1.2 [41]. Considering the maximum inner and the minimum outer radius from table 19, the novel leak testing device provides a radii ratio of 1.7 and thus can clearly be considered as thick-walled. At thick-walled pressure vessels two kind of stresses need to be taken into account: Compressive

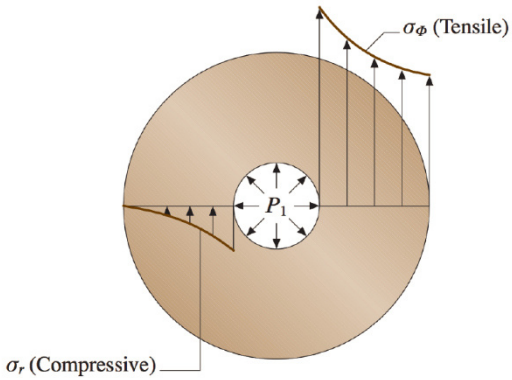

Figure 50: Stress distribution for a thick-walled vessel pressurized from the inside [41]

stresses σ_r and tensile stresses σ_ϕ. With the absence of bending and shear forces both are axial symmetric but vary with the radius r. At figure 50 these stresses are illustrated.

Table 19: Parameter for pressure vessel calculation

Parameter	Symbol	Value	Unit
Maximal inner radius	$r_{i,max}$	20	mm
Minimal outer radius	$r_{o,min}$	34	mm
MEOP	p_{MEOP}	n/a	bar
Proof pressure	p_{proof}	n/a	bar
Ambient pressure	p_{amb}	1	bar
Material properties of stainless steel 1.4301 [31]			
Yield strength	$R_{p0.2}$	205	MPa
Tensile strength	R_m	515	MPa

After identifying all relevant stresses occurring inside the pressure vessel, their values need to be determined exactly. Therefore, literature gives the Lame's equations for thick-walled pressure vessels [41]. These equations are given by equation (5.25) and (5.27) and allow the calculation of the relevant compressive and tensile stresses.

$$\sigma_{r,MEOP} = \frac{p_{MEOP} \cdot r_{i,max}^2 - p_{amb} \cdot r_{o,min}^2}{r_{o,min}^2 - r_{i,max}^2} + \frac{(p_{amb} - p_{MEOP}) \cdot r_{o,min}^2 \cdot r_{i,max}^2}{r_{i,max}^2 \cdot (r_{o,min}^2 - r_{i,max}^2)} \tag{5.26}$$

$$\sigma_{r,MEOP} = (-)\frac{p_{MEOP} \cdot r_{i,max}^2}{r_{o,min}^2 - r_{i,max}^2} \cdot \left(1 - \frac{r_{o,min}^2}{r_{i,max}^2}\right) \tag{5.27}$$

$$\sigma_{\phi,MEOP} = \frac{p_{MEOP} \cdot r_{i,max}^2 - p_{amb} \cdot r_{o,min}^2}{r_{o,min}^2 - r_{i,max}^2} - \frac{(p_{amb} - p_{MEOP}) \cdot r_{o,min}^2 \cdot r_{i,max}^2}{r_{i,max}^2 \cdot (r_{o,min}^2 - r_{i,max}^2)} \tag{5.28}$$

$$\sigma_{\phi,MEOP} = (+)\frac{p_{MEOP} \cdot r_{i,max}^2}{r_{o,min}^2 - r_{i,max}^2} \cdot \left(1 + \frac{r_{o,min}^2}{r_{i,max}^2}\right) \tag{5.29}$$

As shown, by inserting p_{MEOP} into the Lame's equation, the stresses for the nominal pressurizations can be determined. The yield values result in a sufficient safety factor for MEOP:

$$\mu_{r,MEOP} = \frac{R_{p0.2}}{\sigma_{r,MEOP}} > 1.5 \quad \& \quad \mu_{\phi,MEOP} = \frac{R_{p0.2}}{\sigma_{\phi,MEOP}} > 1.5 \tag{5.30}$$

Conducting an equivalent calculation inserting p_{proof} instead of p_{MEOP} Lame's equations yield the following values:

$$\sigma_{r,proof} \quad \& \quad \sigma_{\phi,proof} \tag{5.31}$$

$$\mu_{r,proof} = \frac{R_{p0.2}}{\sigma_{r,MEOP}} > 1.2 \quad \& \quad \mu_{\phi,proof} = \frac{R_{p0.2}}{\sigma_{\phi,MEOP}} > 1.5 \tag{5.32}$$

The determination of these 4 safety factors demonstrates the ability of a safe operation of the novel leak testing device throughout the entire pressure domain up to a proof pressure. However, to validate the analytical results, experimental investigations on the device are conducted in the following.

5.2.4 Experimental validation of novel leak testing device

To validate the theoretical strength calculation presented within the previous chapter, the novel developed test jig needs to undergo crucial experimental investigations. This especially gains importance considering the safety of human lives while handling the test device. Therefore, and most importantly, the test jig must pass a proof pressure test successfully. This test validates the jig's capability of a safe operation even far above the nominal operating pressure of MEOP. As introduced within the previous chapter, the safety factor of 1.5 is applied again.

After the successful proof pressure test and cleaning, the test jig is subject of a Helium sniffing test. This test determines potential external leakages of GHe by utilizing a mobile Helium detector *sniffing* all seals. It should demonstrate the jig's ability ensuring a sufficient sealing of GHe at all component interfaces. Hence, all Variseals, all Copper flat seals and the electrical feed trough are investigated during this test. The test is conducted according to the fluid plan and test set-up from section 5.2.5 at 0.6·MEOP and MEOP. No external leakage is detected.

The determination of the background leakage rate into the measurement line is further presented within chapter 5.5.1.

Proof pressure test

The proof pressure test is conducted at the Ariane Group's cold test facilities at Lampoldshausen. As outlined above, this test should demonstrate the jig's safe operation at MEOP multiplied by the safety factor of 1.5. Hence, a proof pressure of 1.5·MEOP is required to be applied. Preventing any danger due to a potential failure and rupture, the test device is placed inside a shatterproof container made out of Kevlar as seen in figure 51. The upper side of the container is covered by a bulletproof blanket. The corresponding flow schematic for this test is further presented in figure 52. The leak testing device is assembled with its pressure configuration interface and connected to the indicated fluid circuit enabling a forward pressurization. The outlet port is closed by a dummy plug. The inlet port is connected to the feed line system which provides a pressurization of water by an attached nitrogen supply and a pressure regulator. The pressure is measured by a pressure gauge and is read from a digital display at the control panel. As the load cell XFTC 300 provides a protection index of IP50, it is not compatible with any kind of fluids. Therefore, the load cell is replaced by a dummy for this test. Validating all parts of the test jig which includes the welded adapter of its outlet port, the test is executed without the implementation of a seal seat and a poppet.

Figure 51: Test set-up for proof pressure test of novel leak testing device

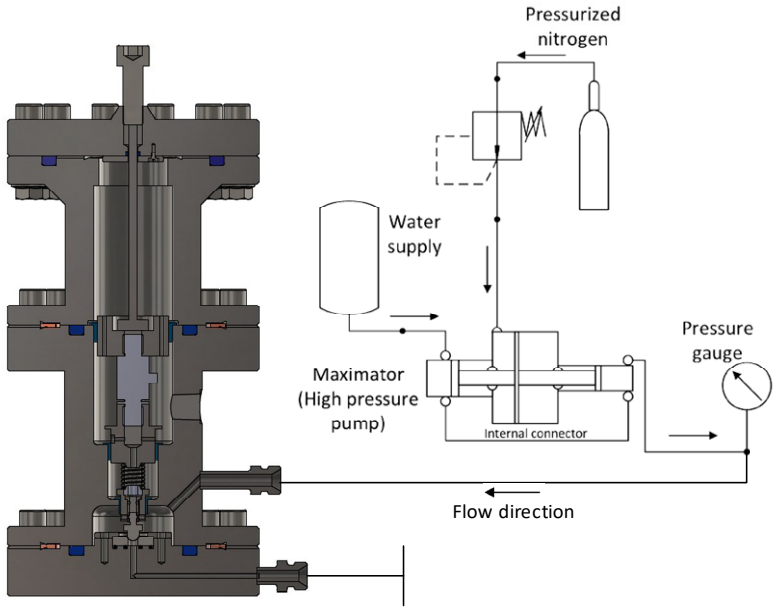

Figure 52: Flow schematic for proof pressure test of novel leak testing device (modified from [42])

After setting up the experiment as described, the inlet water pressure is increased continuously up to the proof pressure. Once reaching $p_{proof} + 5\%$, the pressure was hold for 10 min. The recorded pressure data can be read from figure 53. As it can be seen, no significant and abrupt pressure drop was measured. Hence all parts, as well as all seals withstood the applied pressure. The only anomaly which occurred during the test is also indicated in the pressure profile. Within about one minute, the pressure decreased steadily from about 105% to 100% proof pressure before it was re-pressurized again. After the test, the jig was inspected visually and a few small water droplets have been found leaking through the Teflon taped thread of the electrical feedthrough. However, as the absence of leakage was not the objective of the test and as the device withstood the applied pressure loads, this test is passed successful. Subsequent the test, the Teflon tape was fixed by exchanging the old tape. By further visual inspection, no visual damages or deformations at any components are detected. Hence, the safe operation of the novel leakage test devices is validated and further investigations can be conducted.

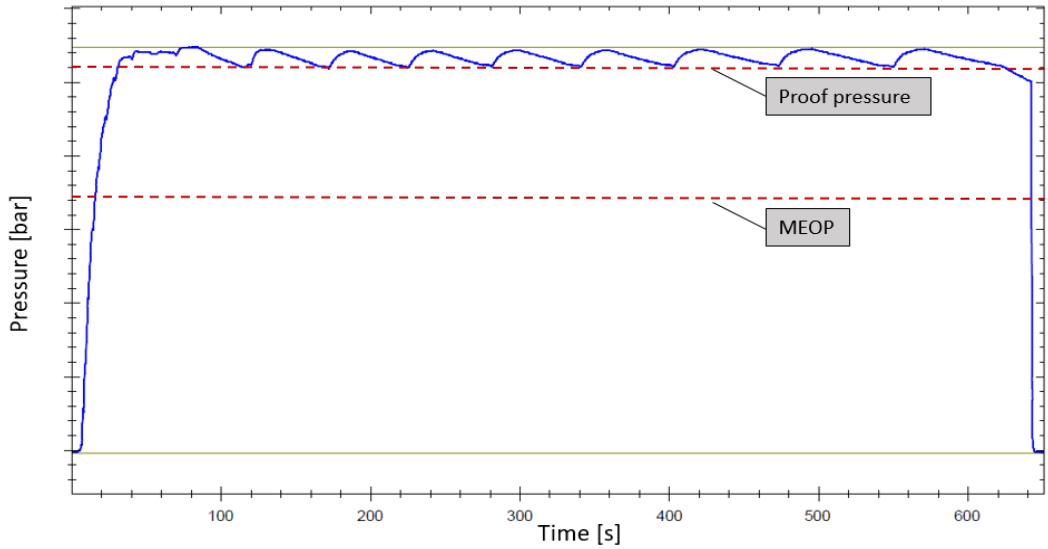

Figure 53: Result of proof pressure test of novel leak testing device

5.2.5 Fluid plan and measurement methods for leakage tests

As the proof pressure test, all experimental investigations on leakage rates are also conducted at the cold test facilities at Ariane Group at Lampoldshausen. The use of this cleanroom class 9 test facility prevents small dust particles, which could cause a leakage path, deposit onto the sealing surfaces after cleaning and during mounting of the specimen. Figure 54 presents the flow schematic of the test set-up. After exiting its tank (8), the GHe firstly is compressed by the Helium compressor (7) and subsequently manually regulated by the He pressure regulator (5). The pressurization line between regulator and test jig (3) is connected to a Keller PA-33X pressure transducer (4) which displays the current pressure readings using a digital display. While the pressurization line is connected to the inlet port of the jig, the Helium leak detector (3) is connected to the jig's outlet port. This Leybold UL 200 leakage detector is a mass spectrometer with an additional turbomolecular pump to establish a UHV and detect a leakage rate up to $5 \cdot 10^{-11}\, scc/s$. The incoming atoms firstly get ionized by collisions with accelerated electrons and subsequently separated for a certain mass to charge ration by a magnetic sector field. This way, the ion collector can be calibrated to detect only Helium atoms and no other gas species. The measured leakage rate can then be read from an attached digital display again.

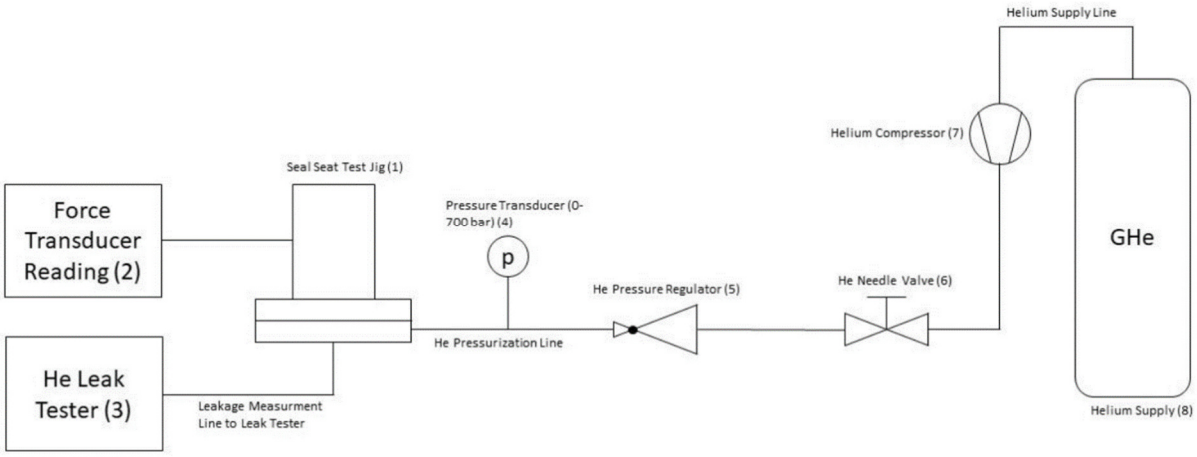

Figure 54: Fluid plan of leakage test set-up [10]

As briefly mentioned before, the applied force onto the seat and poppet is measured by the miniature load cell XFTC300 which is implemented into the test jig. This stainless-steel load cell provides a linear relation between the applied force and the output signal throughout its entire measurement range. The load cell's operational voltage of 10 V is supplied by the amplifier module Burster Type 9243. This module also amplifies the load cell's output signal of a few millivolts to a range between ±10 V and thereby enables a reading by the data acquisition module DataQ DI-1120. This basically constitutes a simple analog to digital converter which is connected to the measurement laptop via USB. The signal is visualized and saved by the corresponding DataQ software WINDAQ. An overview over the described measurement methods can be seen in table 20.

Furthermore, regarding the implementation of tests at thermal extrema, the implementation of thermal sensors is required to control and regulate these thermal environments. Therefore, four Pt100 resistance temperature detectors (RTDs) are implemented at different measurement points at the jig and its surrounding. The temperature regulation is conducted following one reference temperature reading. A more detailed description of the positioning of the temperature sensors is stated in chapter 5.4.4.

Table 20: Measurement equipment overview

Parameter	Sensor	Range	Accuracy	Output
Pressure	Keller PA-33X [43]	0 to 700 bar	± 0.05 %	Digital display
Leakage rate	Leybold UL 200 [44]	10^{-3} to 5 $\cdot 10^{-11}$ scc/s	±50 %	Digital display
Temperature	RTD Pt100	-200 to 600°C	±0.75°C	Laptop reading
Force	XFTC300 [32]	0 to 500 N	±2.5 N	mV range
Amplifier	Burster Type 9243 [45]	2.5 mV to 10 V	±0.05 %	± 10 V
Data acquisition	DataQ DI-1120 [46]	±100 V	14 bit resolution	Laptop reading

5.3 Test plans

This subsection will provide an overview over all envisaged tests. Firstly, the driving objectives which shall be determined by the implemented tests are presented. Later, the test procedures, as well as an assignment of poppet and seal test articles are given.

5.3.1 Test objectives

The experimental investigations described within this chapter should serve the major objective to identify one potential seal variant for the SMAV NO out of various possibilities. Further, the investigated seals should be characterized considering important key aspects. Primarily, the sealing capability of the specimen should be determined during the tests. In particular, this includes the seal's performance throughout the entire pressure and temperature domains which are stated at 3.1. Furthermore, the force which is required to meet the specified leakage requirements shall be determined during the tests too. This force greatly affects the design of the spring which is implemented in the valve. Lastly, potential procedures of treatment of the specimen shall be elaborated too. This e.g., implies a processing of the coated surface or further cleaning and mounting procedures.

5.3.2 Test procedures

To determine all the stated test objectives, three classifications of tests can be defined. These tests mainly differ regarding their test parameter. Thereby it is distinguished between parameter which are maintained constant during a test, parameter which are varied during a test and parameter which are intended to be determined by the test. An overview of the resulting seal test categories is given by table 21. The respective tests are further described in the following.

Table 21: Classification of seal tests and its test parameter

Envisaged test	Const. parameter	Varied parameter	Determined parameter
Force determination	Temperature	Force, Pressure	Forward- & reverse leakage rate, Required axial sealing force
Constant temperature	Force, Temperature	Pressure	Forward- & reverse leakage rate
Thermal cycling	Force, Pressure	Temperature	Forward- & reverse leakage rate

Force determination at constant room temperature

To evaluate the seal's fundamental capability of fulfilling the leakage requirements, a first test of each specimen will be conducted at a constant room temperature. The further aim of this test is to determine the preload onto the poppet which is required to obtain the target leakage tightness. This especially includes all three pressurization cases shown by figure 35. Therefore, the applied axial force, as well as the inlet pressure of GHe are varied during the test. Serving this procedure, a test plan is

developed which makes it possible to evaluate this force. This test plan is shown by the flow chart of figure 55. It can be seen, that the determination of the required preload constitutes an iterative process. The test will start with an initial preload force of 10 N and no applied pressure of GHe. During the test procedure the applied pressure will be continuously increased according to the defined pressure levels given by table 22. At each pressure level the leakage rate is measured and instantly compared to the target leakage rate. If the requirement is fulfilled, the applied pressure can be increased further. If the leakage requirement is missed, the axial preload needs to be increased by 10 N steps.

From table 22 it can be seen, that two pressurization phases are applied during the test of each pressurization case, thus in total 4 test phases with corresponding 26 pressure levels need to be implemented. Firstly, an increasing forward pressure from 1 bar absolute pressure to MEOP is applied. After reaching MEOP, the applied pressure is decreased stepwise. Subsequently these two phases are conducted successfully, the novel pressurization case of an applied pressure reverse to the nominal flow direction is realized by switching the interfaces of the new test jig. Once again, the pressure level gets cycled and the required sealing force is determined.

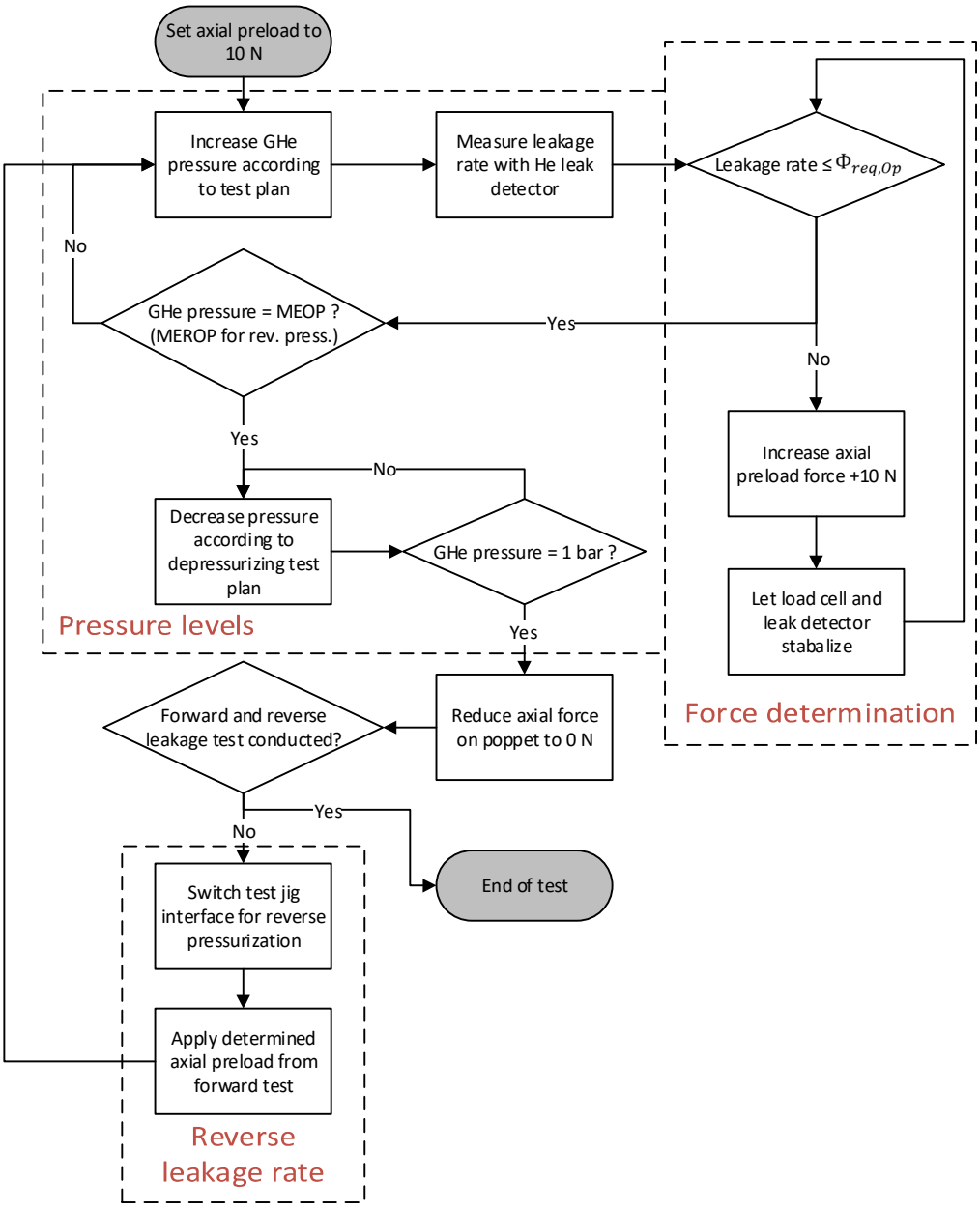

Figure 55: Flow scheme for force determination tests

Table 22: Pressure levels for leakage rate measurement tests at constant temperature

Test phase	#	Forward pressurization [% MEOP]	#	Reverse pressurization [% MEROP]
Increasing pressure	P1	0.3	P16	3.3
	P2	0.6	P17	6.6
	P3	1	P18	16
	P4	7	P19	33
	P5	15	P20	66
	P6	30	P21	100
	P7	60	--	--
	P8	100	--	--
Decreasing pressure	P9	60	P22	66
	P10	30	P23	33
	P11	15	P24	16
	P12	7	P25	6.6
	P13	1	P26	3.3
	P14	0.6	--	--
	P15	0.3	--	--

Leakage rate measurements at constant minimal and maximal temperature

After the prove of the sealing's capability and the determination of its corresponding required preload force, the specimen's performance can further be investigated at different environmental conditions as the minimal and maximal operating temperature defined at 3.1.2. Those conditions represent critical application cases as material properties generally are dependent on the temperature. This especially holds true for the density and strengths of solid materials. Different materials provide a different shrinkage and expansion behavior due to temperature changes which will inevitably lead to small movements and stresses at the sealing line. Even the motions of gas atoms and molecules are strongly dependent of the temperature and may tend to penetrate through the seal more likely at a higher thermal energy. This exemplifies the purpose and need of these tests within an extreme thermal environment to determine all those uncertainties.

As this test again is implemented with a constant temperature over time, its procedure bases on the above described test plan. However, to reach the maximal and minimal temperatures, the test jig needs to be placed inside a thermally controlled chamber at the cold test facilities at Ariane Group. An opening of the chamber during a test would significantly disturb the controlled environment and result in an unintended decrease or increase respectively of the temperature. Therefore, a force adjustment during the thermal extrema tests is not possible and hence the axial force will be set to the value which is determined from the force determination test above. However, the pressurization cases and levels from table 22 are still applicable for this test. Worth mentioning, to switch the interface of the test jig to enable the reverse pressurization case, the test needs to be paused after finishing the forward pressurization scheme until the jig's temperature allows a manual switch between the pressure and vacuum interfaces. The installation of required temperature sensors is further explained within the chapter 5.4.4.

Leakage rate measurements during thermal cycling

As seen from table 21, this test differs from the two test types above regarding the constant and varying test parameter. For this test the temperature is not maintained constant anymore but cycled. This even enhances the above mentioned challenges on the seal. The specimen is now exposed to a constant pressurization and a constant preload force. At the thermal cycling tests, the jig again is placed inside the thermal chamber and the previously determined axial preload force needs to be applied. To model a greatest possible similarity to later qualification tests of the valve, the thermal cycling profile from chapter 3.2.2 should be applied for these development tests as well. As described, this cycle comprises 12 full thermal cycles and 6 points at which a leakage measurement should be implemented. During the

entire thermal cycling and especially during the leakage rate measurements, the test jig needs to be maintained a certain constant pressure. . For the forward pressurization case, this pressure is defined at MEOP, whereas for the reverse pressurization case the maximal reverse pressure MEROP should be applied. If the two previous tests at constant temperatures have identified another pressurization case at which the leakage rate reaches its maximum, this pressure should also be applied during the thermal cycling tests.

5.3.3 Specimen assignment

This subsection gives a brief overview about all scheduled tests and assigns the specimen which will be investigated at those tests by use of serial numbers (SN). As described within chapter 5.1.2, variant I will not further be investigated experimentally as for the above stated reason of a too high sealing force. However, its design iteration variant I.I, as well as variant II and its improved versions variant II.I and II.II will be investigated. Particularly, variant II serves to validate the results gained by Radermacher during previous tests. To validate those tests, variant II will be investigated only at a constant room, minimal and maximal temperature as implemented by Radermacher. Furthermore, no leakage measurement during a reverse pressurization has been conducted previously and therefore is not needed to be validated. That is why, the three validation tests with variant II SN1 of lot 2 (L2) are implemented right after the start of this thesis using the former test jig for forward pressurization. Concluding this validation, also variant II is neglected, as its design iterations variant II.I and II.II are investigated further. From previous investigations two test articles of variant II are unused. One of these samples is used for the validating investigation of variant II (SN1 L2). The second unused specimen is modified to meet the geometry of variant II.I. In order to investigate the most promising solutions which provide the greatest similarity to potential later prototypes, all other envisaged tests focus on specimen of variant I.I and II.II. The test article assignment of these variants therefore is listed in the two following table 23 and table 24.

As shown, 5 tests investigating each poppet-seat variant are envisaged. To implement these tests, 5 specimens of variant II.II are manufactured and coated in the course of this project according to the procedures which are stated within section 5.1.3.

Table 23: Test article assignment for variants I.I and II.II

Test article assignment		**Poppet (variant I.I & variant II.II)**				
		SN1	**SN2**	**SN3**	**SN4**	**SN5**
Seat (variant I.I & variant II.II)	**SN1**	X				
	SN2		X			
	SN3			X		
	SN4				X	
	SN5					X
Test #		**#1**	**#2**	**#3**	**#4**	**#5**

Table 24: Envisaged experimental investigation on variant I.I and II.II

Test #	Description	Purpose	Temperature [°C]	Abs. pressure [bar]	Force [N]
1	Ambient test	• Force determination of new specimen variants • Forward & reverse leakage rate at room temperature	+22 ± 3	1 – MEOP	To be deter-mined
2	Minimal temperature test	• Sealing performance at thermal extrema • Forward & reverse leakage rate at minimal temperature	$T_{Op,g,min}$+0/-3	1 – MEOP	From #1
3	Maximal temperature test	• Sealing performance at thermal extrema • Forward & reverse leakage rate at maximal temperature	$T_{Op,g,max}$+3/-0	1 – MEOP	From #1
4	Thermal cycling	• Sealing performance at thermal and pressure extrema • Performance durability over long test period	$T_{Op,g,min}$+0/-3 to $T_{Op,g,max}$+3/-0	MEOP & MEROP	From #1
5	Thermal cycling	• Sealing performance at thermal extrema and critical pressure • Performance durability over long test period	$T_{Op,g,min}$+0/-3 to $T_{Op,g,min}$+3/-0	Critical pressure	From #1

5.4 Test preparation

5.4.1 Specimen preparation

To ensure no external induced leakage paths e.g., by dust particles, all test articles must be cleaned in advance of any experimental investigations. Furthermore, all specimen must be examined by a visual inspection checking for any scratches, damages or contaminations. Therefore, the articles are cleaned inside an ultrasonic isopropanol bath for 10 minutes. Afterwards a visual inspection under a microscope is conducted. Hereby, the articles are photographed and documented. Finally, after the mounting of the seat and the poppet while wearing gloves, again they are cleaned by using liquid isopropanol. To ensure a full evaporation they are dried with nitrogen gas afterwards.

This procedure represents the standardized method of preparing all test articles. However, some test articles such as variant II and II.I require an additional pre test surface treatment. As briefly mentioned before, the coated seats of these variants need to be polished and pre-coined in advance. Therefore, the following procedure is implemented:

The rough surface of the coated material II.B as seen in figure 40 a.) needs to be hand polished using sandpaper with a grain size of 2400. The seat is mounted in a lathe machine which is set to 1500 rpm. By wrapping the sandpaper around a small wooden stick, the through hole and the seat's chamfer can be polished adequately. The polished result is then cleaned again inside an isopropanol bath and inspected under the microscope. Afterwards, the seat's sealing line needs to be pre-coined. Figure 56 illustrates the pre-coining set-up. The poppet is mounted into a hydraulic hand press, while the seat in placed onto a load cell. This load cell provides a measurement range up to 500 N. To reach a sufficient coining effect, the maximal force is applied, hence 500 N pre-coining force. The force is hold for 1 minute and read at the display of an attached amplifier. As described earlier at 5.1.3, poppet and seat underlie a certain manufacturing tolerance. Thus, their shapes are not a perfect sphere or a circle respectively. Considering this, the plastically deformed stamp molding is not perfectly rotational symmetric likewise. This makes it overall important to prevent a twisting of poppet and seat at the final assembly into the test jig, compared to their orientation during the pre-coining. That is why, poppet and seat need to be marked in advance of the pre-coining process as seen in figure on the right (black marks).

Figure 56: External pre-coining set up for variant II, II.I & II.II

Pictures of the unprocessed surface, the polished surface, as well as the pre-coined sealing line have been already presented at figure 40.

5.4.2 Test jig preparation

To prevent a transmittance of dust contamination from the jig to the specimen, in advance of mounting poppet and seat, the test jig is cleaned using isopropanol and nitrogen gas. Using the former forward pressure test jig or also the novel jig with the double O-ring application, it is important to implement new and non-permeated O-rings and grease them with Krytox beforehand. This increases the vacuum sealing capability. However, implementing the metal C-rings into the reverse pressurization jig, it is overall important to handle the rings with gloves, especially the Tin-plated CI-rings. Afterwards the poppet can be mounted by screwing it into the poppet holder and the seat is placed into the provided groove. Following this, the seat needs to be tightened to apply a certain preload force onto the sealing of the measurement line. Both metal C-rings require a preload between 77 – 104 N/mm circumference [40]. Finally, the test jig can be closed be screwing the lower two flanges together.

Regarding the novel reverse pressurization test jig, the interface change of the vacuum respectively pressure feedthrough can easily be executed by removing the upper flange and pulling the entire interface upwards. The vacuum interface uses the smaller bolt circle with an implemented CF copper flat seal of size DN 45. Mounting the pressure interface at the outer bolt circle, the additional Variseal 75.8 x 90 mm needs to be implemented.

5.4.3 Load cell calibration

In advance to a test after a long intermediate time without testing and furthermore, after the test jig and its load cell were disassembled, it is necessary to calibrate the load cell. This is important to prevent zero drifts over time falsifying the measurements and to ensure the application of the correct scale calculating the forces out of the measured voltages. The calibration is implemented by loading the spring and the load cell upside down with calibration weights as indicated in figure 57. By the given mass of the weight, the force due to gravity can easily be calculated and correlated to the measured output voltages of the load cell. Exemplary, the calibration values for the measurements of variant I.I and II are listed in table 25. To maximize the accuracy of the calibration the measurement is conducted two times. Utilizing these values, a calibration line which is presented in figure 58 can be calculated. This line constitutes a linear curve of best fit out of the given values. Its gradient gives the mean sensitivity of the load cell -11.311 N/V. To apply the calibration line during the measurements, its parameters need to be implemented into the DataQ measurement software.

Figure 57: Load cell calibration procedure [33]

Table 25: Load cell calibration data

Weight [kg]	Equivalent force [N]	Measured Output [V]	
		#1	#2
0	0	9.78	9.77
0.1	0.981	9.68	9.69
0.6	5.886	9.3	9.3
1.1	10.791	8.85	8.89
2.1	20.601	8.07	8.17
5.1	50.031	5.57	5.44
10.1	99.081	1.25	1.19
15.1	148.131	-3.56	-3.18

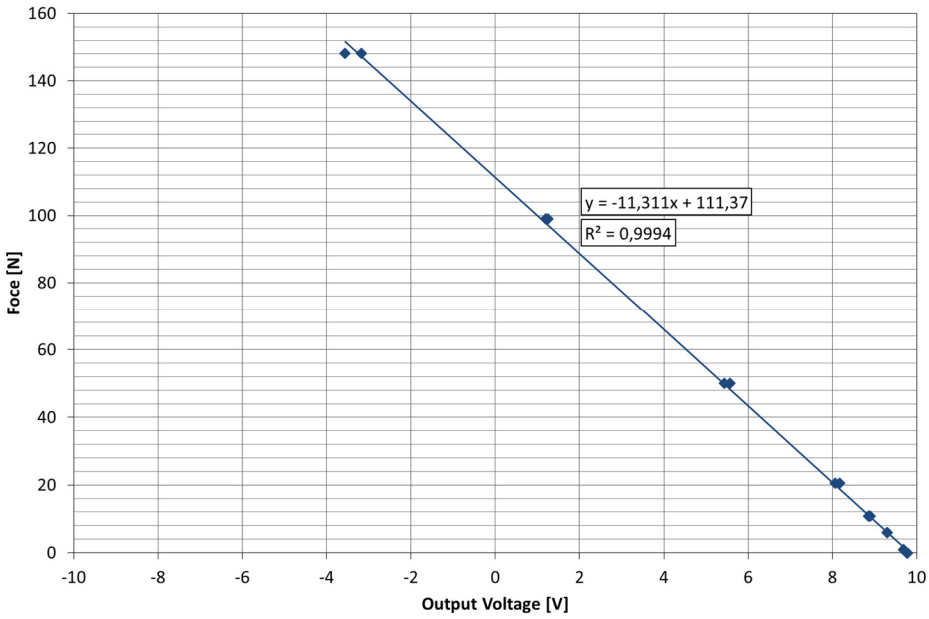

Figure 58: Load cell calibration graph

5.4.4 Thermal sensor installation

Considering the implementation of the envisaged tests at thermal extrema or especially thermal cycling, the accurate record of the temperature at certain measurement points is of overall importance. Therefore, three RTDs of type Pt100 with a measurement range of -200°C to 600°C are attached to the test jig. A fourth Pt100 is placed right next to the jig to measure the environmental temperature. As the installation of RTDs inside the jig is not possible, three measurement points at the outer surfaces of each component are chosen. This still yields representative measurements as the jig is made out of stainless steel which provides a good thermal conductivity. By implementing a hold time, after all thermal sensors at the outside have reached the target temperature, it can be expected that the inside temperature and especially the seat's and poppet's temperature have reached the same target. Figure 59 indicates all measurement points. As the seat is mounted onto the bottom plate, this attached RTD represents the reference temperature of the seal. However, only after all four thermal sensors have reached the target temperature and display values within the 3 K tolerance, the respective test is started.

Figure 59: Installation of thermal sensors

5.5 Leakage test results

The four previous subsections provided a detailed description of the specimen which are subject of the investigations. The respective test objective and furthermore the methods of the tests' implementation are also described. Concluding this chapter, this subsection now presents the test results of the above developed test schemes.

5.5.1 Background leakage

In advance of the investigation of final specimen, the test facilities itself needs to be characterized in detail. This particularly has to be considered as no falsification of the later presented test results is highly desirable. As described within section 5.2.1, at previous investigations the former test jig has proven some insufficiencies regarding the correctness of the measurement results. The so-called background leakage rate which is caused by the permeation of GHe atoms through a soft elastomeric O-ring as a function of pressure and exposure time, may have falsified previous test results significantly. To investigate this permeation behavior in detail, tests with blind seats are implemented. Those seats simulate a fully leakage free seal seat. This enables a separation of seal leakage and O-ring permeation and thus allows an accurate and quantifiable determination of the background leakage rate.

Former test jig for forward pressurization

As mentioned above, the permeation through a single elastomeric O-ring seal is significantly influenced by the time the O-ring is exposed to the GHe and furthermore by the compressing force onto the ring. To validate this statement, tests have been implemented at which the critical O-ring is reused from previous tests. This way, the O-ring has already been exposed to GHe over a period of 20 minutes and hence the ring is expected to be saturated with Helium atoms. If this is the case, the O-ring would not be able to absorb further atoms and thus demonstrate a higher permeation rate, the so-called background leakage rate. To enable a quantitative evaluation, the measurement is compared to a test result of a fresh and unused O-ring from [10]. The results are presented by the following figure 60.

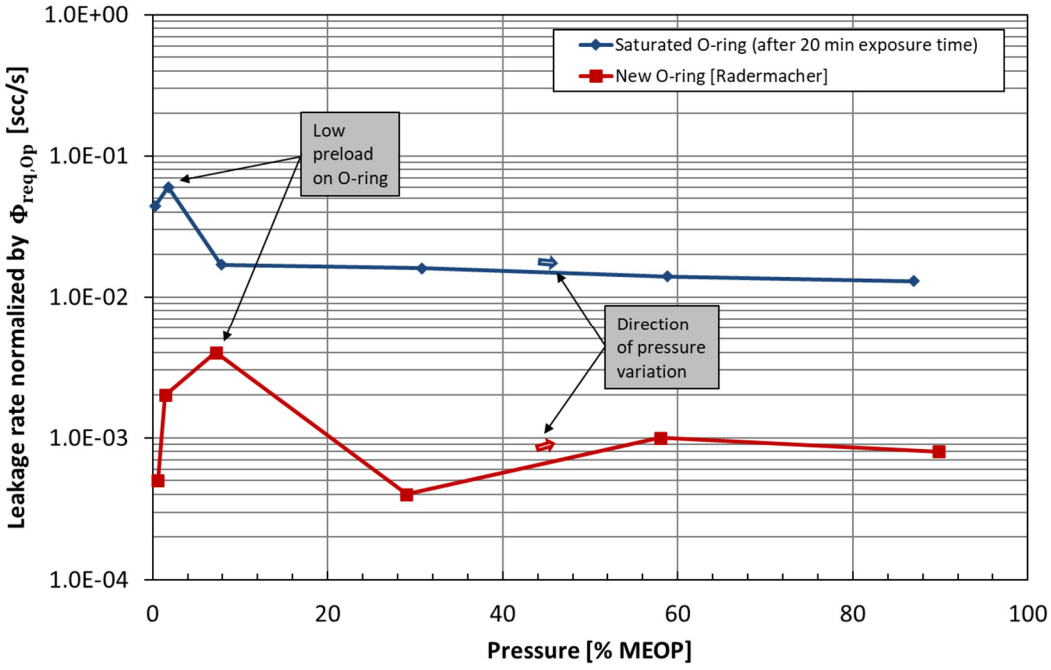

Figure 60: Background leakage rate of former leak testing device with elastomeric O-ring

The leakage rate of the used O-ring yields more than one order of magnitude higher than the leakage rate of a fresh O-ring. This confirms the above stated thesis that the O-ring permeation highly increases with the exposure time of the O-ring. Considering long thermal cycling tests, this behavior would falsify

all measurements significantly as the background leakage rate reaches almost the area of the seal's target leakage rate. Figure 60 shows further, that the background leakage rate reaches a maximum at low pressures up to 10 % MEOP. It is assumed that this peak might be caused by two different mechanisms. At low pressures the compressing force applied by the pressure onto the blind seat is not high enough to close all macroscopic leakage paths. After reaching a leakage maximum, the pressure driven compressing force increases and thus seals all macroscopic leakage paths. The remaining background leakage rate then is mainly caused by the microscopic permeation process. This result particularly is important considering the design of the novel test jig to enable higher preloads on the seal at lower pressures by improving the mounting mechanism. This is realized by 6 M6 screws instead of one single screwcap.

Novel test jig with O-ring solution during forward and reverse pressurization

The novel leak testing device was subject of extensive experimental investigations validating all its different application cases. For a first test, the jig is assembled with the bottom plate designed for the implementation of the two concentric elastomeric O-rings. A picture of the implemented rings and the 5 venting holes (ref. chapter 5.2.2) is presented by figure 61 a.). Both O-rings are unused and greased with Krytox before the test. The novel designed seat mounting mechanism is tightened up to its limit, that the O-rings are not exposed to varying axial forces by a moving seat during a variation of pressure (Figure 61 b.)). For the first test, the jig is set up with its pressure configuration according to figure 46 b.) enabling a forward pressurization. Once after test begin, the pressure was adjusted stepwise according to the specified pressure levels from table 22. Both directions of pressure change, increasing as well as decreasing pressure have been applied. The overall test duration was 60 min with significant hold times of 15 min at 0.6 ·MEOP and MEOP. After the end of the test, the O-rings which are now contaminated with Helium atoms are replaced by new ones. Furthermore, the pressure interface of the jig has now been changed to the vacuum interface according to figure 46 a.) enabling the reverse pressurization.

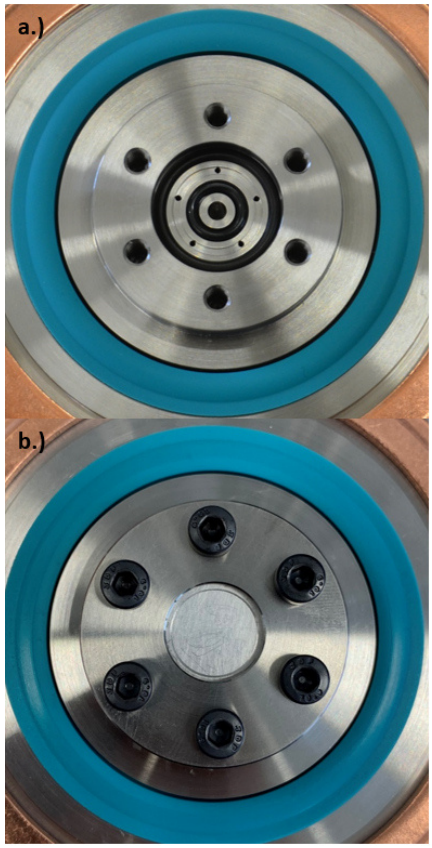

Figure 61: Sealing of measurement line of novel leak testing device: a.) Concentric O-rings with venting holes; b.) Blind seat

The blue graph of the following figure 62 illustrates the obtained results for the background leakage rate through both elastomeric O-rings during a forward pressurization. The two red graphs give the background leakage rates for a reverse pressurization. While the dotted graph represents the results after one hour subsequent the forward pressure test, the continuous red line gives the leakage rate after 2 days not using the leak testing device.

From the diagram it can clearly be seen, that the background leakage rate at a forward pressurization is successfully reduced to be below the requirement threshold value of $10^{-3} \cdot \Phi_{req,OP}$ over the entire pressure domain up to MEOP. This holds true for both an increasing and a decreasing pressure variation. Due to the higher preload while not twisting the O-rings, enabled by the redesigned mounting mechanism, the peak leakage rate at about 10 % MEOP (ref. figure 60) can be eliminated entirely. As the test duration was 60 minutes, which is about three times as long as the maximal test duration using the former test jig, it can further be stated that the venting holes prevent a significant permeation by GHe of the second O-ring. Solely at a very low pressure gradients during decreasing the pressure, the background leakage rate rises slightly faster. It is assumed that this might be due to the greater relief of the O-ring and its compression at these pressures, which rises the partial pressure of Helium at the space

between the O-rings drastically. In this case the five venting holes are simply not enough to dissipate all atoms and prevent the permeation of the second O-ring. But still, its background leakage rate remains at a low value of $2 \cdot 10^{-3} \cdot \Phi_{req,OP}$. Hence it can be concluded that both a long duration test of several hours at a constant high pressure or also a pressure varying test do not state a problem regarding measurement falsifications due to a background leakage rate.

Considering the reverse background leakage rate, figure 62 clearly shows a strong dependency on the interim time between a forward and reverse pressurization test. During a forward test, the blue elastomeric pressure seals (also shown in figure 61), the so-called Variseals, are exposed to GHe for a long duration. In this case for even 60 min. Just as elastomeric O-rings these Variseals are subject of a significant permeation process too. Thus, they are saturated with Helium atoms after the forward pressurization application. Changing the direction of pressurization immediately after a previous forward pressurization, the background leakage rate is increased significantly by outgassing Helium atoms. This explains the high background leakage rate of around $10 \cdot \Phi_{req,OP}$ during the first reverse pressurization. Proving the made claim, a second reverse background leakage test is conducted after two days of outgassing at atmosphere. The obtained reverse background leakage rate yields 3 orders of magnitude lower than during the first test and ranges between $1 \cdot 10^{-2} \cdot \Phi_{req,OP}$ to $3 \cdot 10^{-2} \cdot \Phi_{req,OP}$. Considering the strong influence of outgassing time, it is assumed that a leakage rate below the stated requirement of $10^{-3} \cdot \Phi_{req,OP}$ can be obtained for a reverse pressurization by prolonging the time in between the tests or by changing/removing the saturated Variseals.

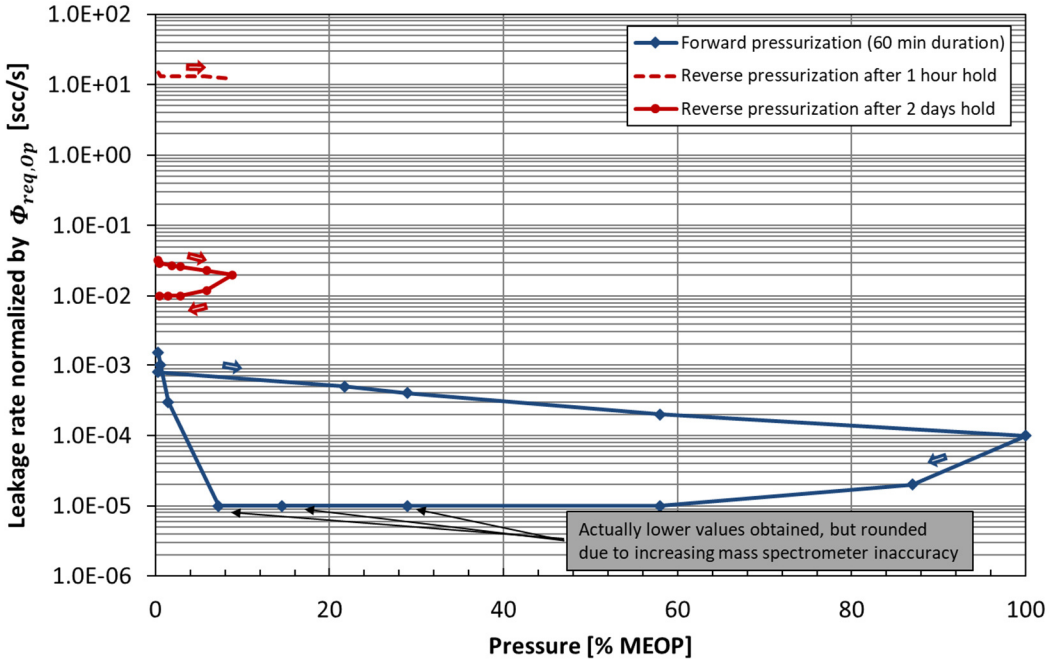

Figure 62: Background leakage rate of novel leak testing device with two concentric elastomeric O-rings and venting holes

Novel test jig with C-ring solution during forward and reverse pressurization

After the successful test of the elastomeric O-rings outlined above, the second solution for an efficient sealing of the measurement line by implementing two metal C-rings is investigated similarly. Applying the found results on the permeation of the Variseals during a forward pressurization however, this time the reverse pressurization test is executed in advance the forward pressurization case. As this investigation is conducted subsequent the previous reverse pressurization test of the O-rings, the Variseals provide the same level of saturation as above. Hence a reverse background leakage rate of around $1 \cdot 10^{-2} \cdot \Phi_{req,OP}$ is obtained – compare red graph of figure 63. This especially gives the results, that both solutions, the O-ring – as well as the C-ring solution perform similarly well during a reverse pressurization.

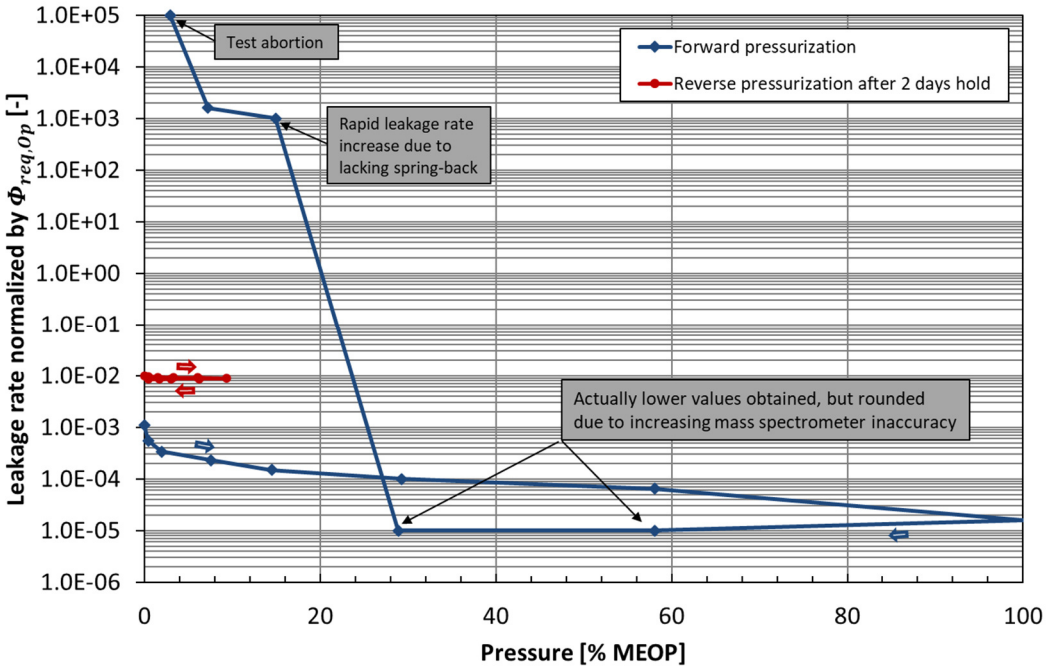

Figure 63: Background leakage rate of novel leak testing device with two concentric metal C-rings

After the reverse pressurization, the forward pressurization test is conducted by simply exchanging the vacuum bellow feedthrough. The corresponding results are given by the blue graph of figure 63. As a major difference compared to the O-ring variant, the metal C-rings require a very certain preload to perform sufficiently. This preload ranges between 77 – 104 N/mm circumference [40]. As this especially implies, that the C-rings do not enable a heavy mounting until contact between seal seat and bottom jig plate, the seal seat is able to move upwards and downwards when it is subject to a pressure variation. This results further in a variation of the load onto the C-rings. During the increasing pressure test phase, the load onto the C-rings steadily increases which results in an increasing sealing capability and hence in a decreasing background leakage rate. This also holds true for high pressures during the decreasing pressure phase. Background leakage rates of less than $10^{-4} \cdot \Phi_{req,OP}$ are obtained. However, at the pressure decrease from 29% MEOP to 14% MEOP, the leakage rate jumps by about 8 orders of magnitude. After further reducing the pressure, the test has to be aborted at leakage rates of $10^{+5} \cdot \Phi_{req,OP}$ to prevent damage to the helium mass spectrometer. This indicates a macroscopic leak and a failing of the outer external C-ring. After the test, the C-rings are inspected visually under the microscope for any damages. No cracks or unwanted deformation are visible. Hence it is concluded, that the high loads caused by high pressures itself and the heavy axial forces by the moving blind seat during the test, significantly decreases the ring's ability of a *spring back.* Without this spring back, the seal provides a malfunction if the applied force decreases again at low pressures. Thus it can be summarized, that the C-rings provide a very well sealing capability without any permeation processes for low varying pressures, as e.g. during the reverse leakage test, as well as for constant high pressures. This advantage particularly is worth considering regarding long term thermal cycling test for several days at constant MEOP. However, for a varying pressure throughout the entire pressure domain up to MEOP and back, the C-rings are unsuitable.

5.5.2 Variant I.I

According to section 5.3.3, the first test of variant I.I constitutes a preload determination test at ambient temperature. Therefore, poppet and seat combination SN1 are subject of this test. As this test is implemented subsequently after the start of this thesis, it is conducted by using the old forward pressure test jig. The temperature is maintained at room temperature and pressure and force are varied. The determined required sealing force is presented by the following figure 64. Additionally, the gained results are compared to results from previous tests [10] of variant I, SN2.

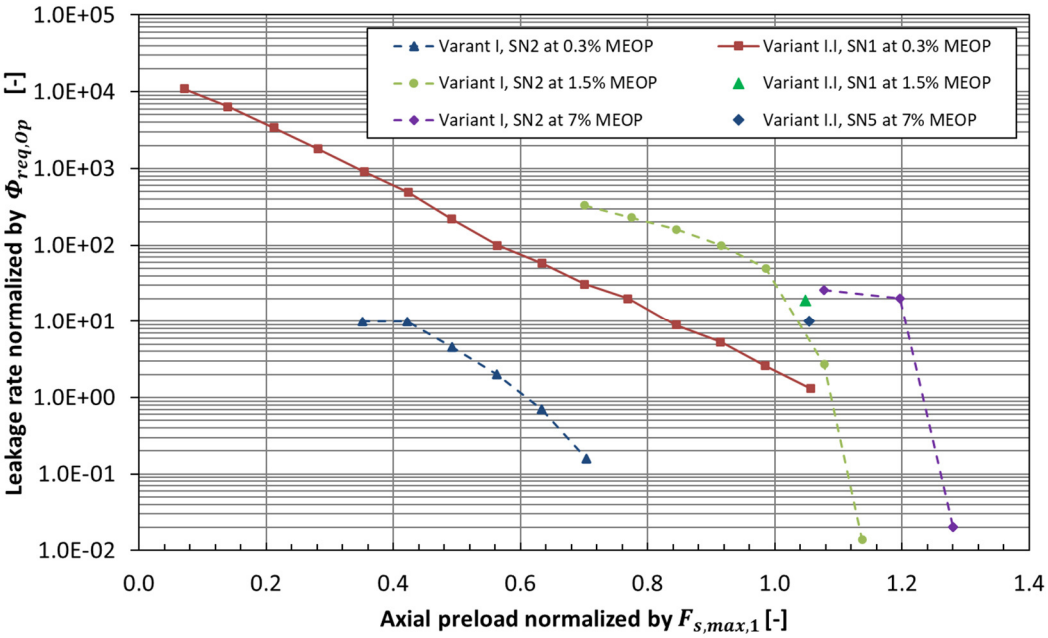

Figure 64: Preload determination test results variant I.I SN1 (Variant I SN2 data from [10])

Analyzing the graph of variant I.I separately, it shows that the capability of leak tightness increases with the applied axial preload force, which seems quite plausible in the first place. It shows, that a smaller ratio of poppet diameter to hydraulic diameter, changes the course of the leakage rate graph from linear to an exponential decrease (vice versa within the presented semi-logarithmic diagram). However, the absolute values of the leakage rate constitute surprisingly high compared to the previous test results of variant I. According to the maximal installable spring force, the force increase is stopped at a value of $1.06 \cdot F_{s,max,1}$. At this preload force the pressure is varied according to the levels of the defined test plan. These results are presented in figure 65.

As the preload determination results would have let expected the leakage rate of variant I.I throughout the pressure domain remains mostly two orders of magnitude higher than the results of variant I gained by Radermacher. However importantly, both results have been yielded at different preload forces as indicated in the legend. Further it can be seen that the leakage results improve with a higher pressure. As mentioned earlier, this results from the additional sealing force applied by the GHe pressure. After reaching a pressure of 60% MEOP the test of variant I.I had to be aborted, as the Teflon tape which seals the electrical feed though started to leak. It is assumed that this comes from the long intermediate time the test jig has been stored since the last test by Radermacher.

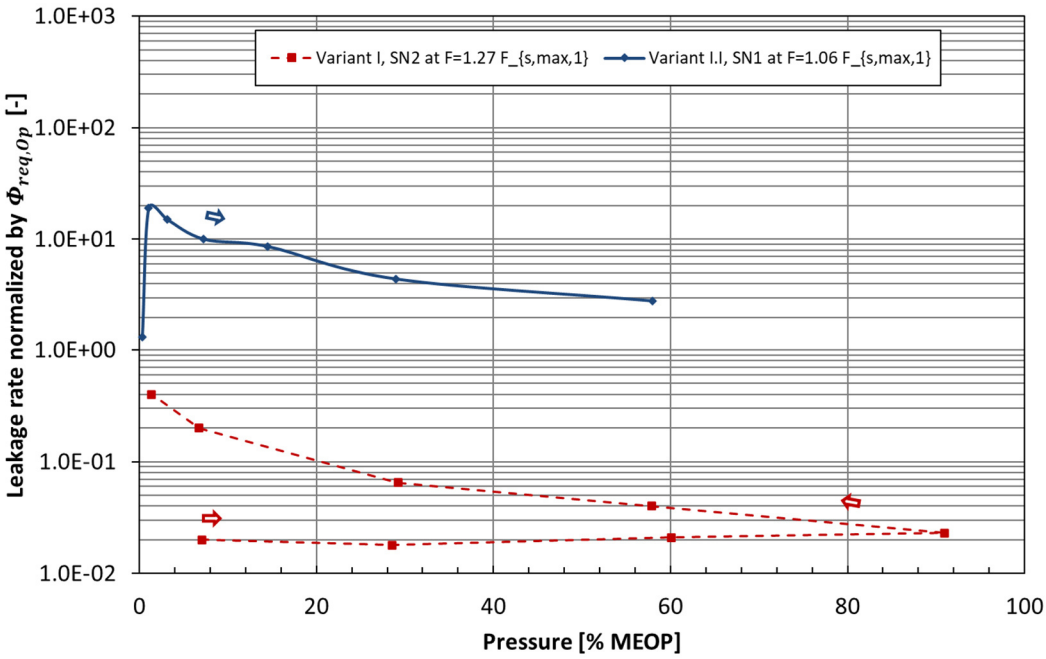

Figure 65: Forward leakage rate test results at ambient of variant I.I SN1 (Variant I SN2 data from [10])

Following the test, both specimen, poppet and seat are investigated under the microscope. The pictures made are presented in figure 66. The poppet's image on the left clearly shows, that despite the lower sealing force, a plastic deformation at the sealing line occurred. As this variant I.I is not able to meet the leakage requirement even though a plastic deformation occurred and especially considering the preload increase by the additional reverse pressurization case, it is decided to reject this variant from further experimental investigations. Thus, the development now focuses on the more promising variants II and II.I.

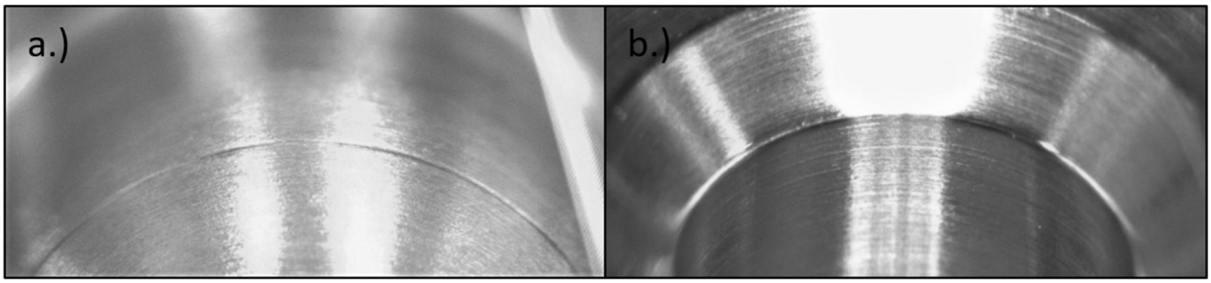

Figure 66: Microscopic pictures of variant I.I SN1 – a.) Poppet material I.B; b.) Seat material I.A

5.5.3 Variant II

As mentioned before, to determine the further development steps a soon validation of the results of Radermacher was necessary at the start of this thesis. Therefore, the specimen SN1 of lot 2 (L2) of variant I are subject of this subsection (Lot 1 was investigated by Radermacher (L1)). To validate the results, the tests are implemented at equal conditions and applying the procedures according to 5.3.2. The seat coated with material II.B is hand-polished and cleaned by an ultrasonic isopropanol bath, afterwards the seat is pre-coined by pressing the poppet onto the sealing line. After a visual inspection and the mounting of both poppet and seat, they are cleaned again by usage of Isopropanol and N_2 gas. To implement this test, the former forward pressure test jig is used again. First, a preload determination is conducted to evaluate the required sealing force for the further tests. The results of this test can be found in figure 67. The red graph and additionally the single measurement points represent the results for SN1 of L2. By analyzing these values, a required preload of $0.49 \cdot F_{s,max,1}$ can be identified clearly.

With this preload force, the specimen demonstrates a leakage rate of lower than $10^{-2} \cdot \Phi_{req,OP}$. Compared to the values of L1 SN2 [10] a quite similar preload (ref. $0.52 \cdot F_{s,max,1}$) can be determined.

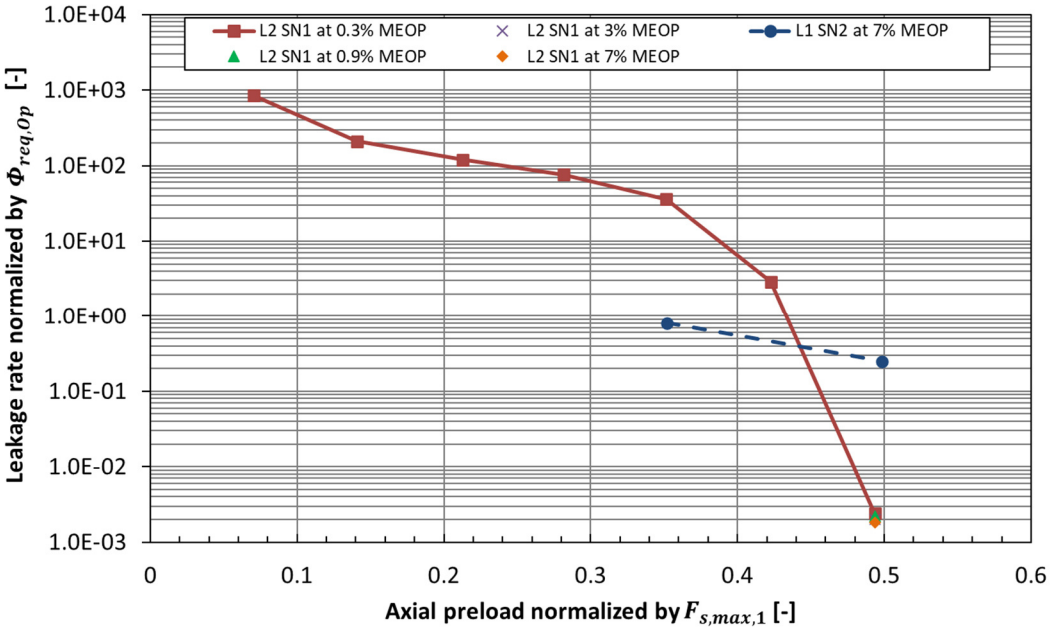

Figure 67: Preload determination test results variant II L2 SN1 (L1 SN2 data from [10])

Subsequently to the determination of the preload, the leakage rate measurement at ambient temperature throughout the entire pressure domain according to the test plan and pressure levels is conducted. The test phase of decreasing pressure levels is also implemented. The results are presented at figure 68 and again compared to results from previous tests of L1 SN2 [10]. Generally, both leakage rates are at the same order of magnitude, especially at pressures above 30% MEOP. The target leakage of $\Phi_{req,OP}$ greatly exceeds the measured leakage rate at these pressures which remains lower than $2 \cdot 10^{-2} \cdot \Phi_{req,OP}$. However, the two graphs show two anomalies which are not similar. As discussed earlier and identified as an O-ring leakage issue due to a poor preload, the previous test results exhibit a leakage rate peak at 10% MEOP. For this test however, the O-ring was preloaded heavily by tighten the screwcap at the bench vice. This adds an additional preload onto the O-ring and seems to eliminate the leakage peak at 10% MEOP but induces a new peak at very low pressures near ambient during the decreasing pressurization. This unusual behavior is intended to result from a twisting and slight damaging of the O-ring during the heavy tightening. Nevertheless, the conducted ambient test is evaluated as successful and therefore two further tests at minimal and maximal temperature are implemented reusing this specimen L2 SN1.

In advance of the thermal extrema tests, the twisted O-ring is replaced by a new O-ring which again is only hand-tightened. Furthermore, a pause of 1 day between the tests is implemented to ensure a sufficient outgassing of Helium atoms out of the O-ring while no pressure is applied. The set preload however, is fixed and not unloaded between the tests. Figure 69 illustrates the corresponding results. Additionally, the test results of leakage measurements at ambient temperature before and after the thermal extrema are depict. The diagram clearly shows the leakage rate's dependency on the temperature. It can be stated, that the seal capability increases when the test aperture is exposed to cold temperatures. This is mainly caused by two reasons. Firstly, the GHe atoms provide a far lower thermal energy at lower temperatures and thus their motion is limited. Hence, they tend less to penetrate the sealing. In fact and secondly, the preloaded force onto the poppet increases with decreasing temperature as the test jig shrinks and applies an additional force. Averagely, the measured sealing force during the cold test was about 10 N higher than the set preload force. The reverse principle is shown at the hot test at $T_{Q,g,max}$. Here the test jig expands and thus decreases the actual load onto the poppet. That is why, a higher leakage rate is detected. However, considering the requirement comprising the temperature

dependent leakage rate profile, a rate of $10 \cdot \Phi_{req,OP}$ at $T_{Q,g,max}$ still meets the requirement of $\Phi_{req,Q}$ at this temperature. Concluding the thermal extrema tests, a final ambient test is conducted to verify the seal's performance even after one full thermal cycle. The purple and dashed graph presents a slightly higher leakage rate than pre test, but the overall seal's performance still remains better than the leakage requirement.

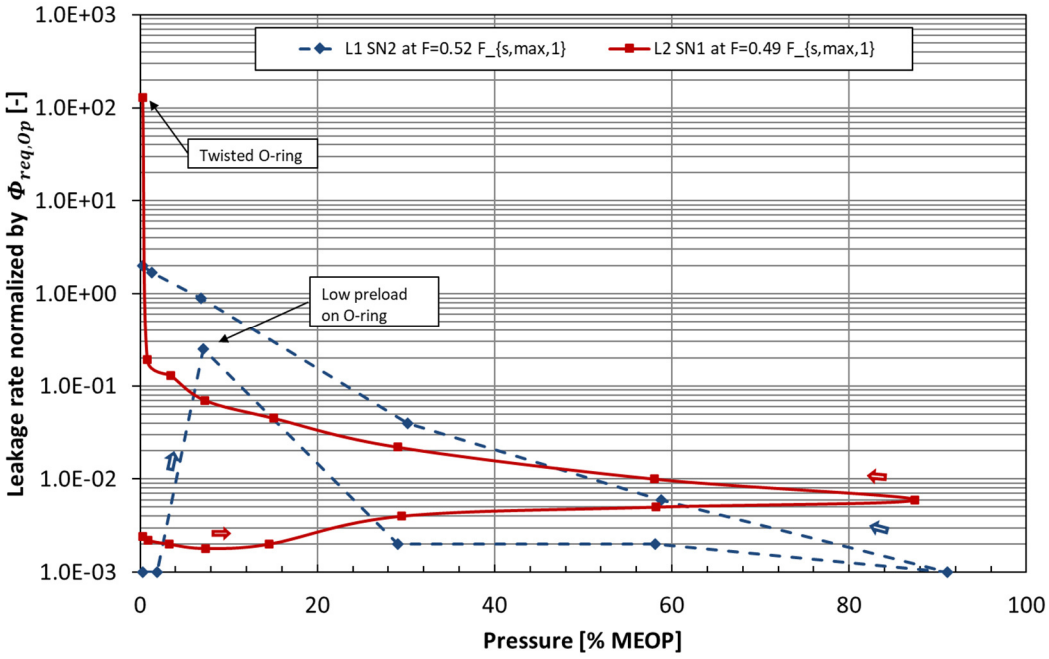

Figure 68: Forward leakage rate test results at ambient of variant II L2 SN1 (L1 SN2 data from [10])

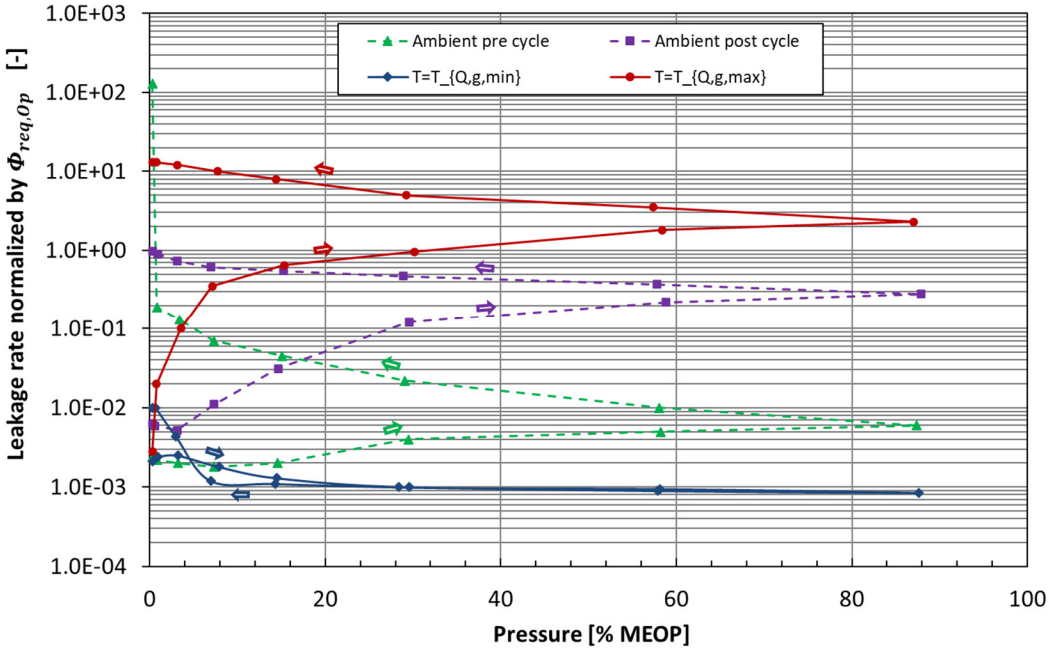

Figure 69: Forward leakage rate test results at thermal extrema of variant II L2 SN1

A visual inspection of the specimen under the microspore post the tests did not show any anomalies or damages neither at the poppet nor at the coated seat. Despite the fact, that nearly all results meet the stated requirements, except for some explained exceptions, also a sufficient similarity to Radermacher's results can be recorded. To improve the seal's performance further, the new iterated designs of this variant, variant II.I and II.II are subject of the investigation in the following.

5.5.4 Variant II.I

After the successful tests of variant II validating previous results, its first optimized variant II.I is subject of the following leakage investigations. Therefore, the test specimen variant II.I SN1 is prepared according to the procedures outlined in 5.4.1. Both poppet and seat are polished with sandpaper. Particularly, the seat's rough surface is smoothened. After cleaning the articles inside an isopropanol bath both components are implemented into the leakage test jig. This time, the novel leak testing device enabling both a forward and a reverse pressurization is utilized. The seat is assembled with two unused O-rings greased with Krytox. Different to the specified procedures, the seat is not pre-coined using an external hydraulic press with 500 N for 1 min, but is pre-coined directly inside the test jig after its implementation. This way, the potential error source of assembling poppet and seat slightly twisted compared to their orientation during the external stamping, which can cause leakage paths due to manufacturing tolerances, can be eliminated entirely. Therefore, and according to the test plan, the forward pressurization test is conducted first. By turning the force adjustment screw as deep as possible until the implemented spring reaches its block length, 347 N can be applied onto the poppet and the seat. This force is hold for 2 minutes. After pre-coining the force determination test is started by applying an initial preload of $0.35 \cdot F_{s,max,1}$. The corresponding results of this test are presented in the following figure 70. Although the preload force is increased up to a value of $1.19 \cdot F_{s,max,1}$ at 7.8% MEOP, the leakage rate remains at a high level and does not fulfil the requirement. Particularly compared to variant II, it can be seen, that the starting leakage rate at $0.35 \cdot F_{s,max,1}$ yields quite similar, but the course of the graph demonstrates a more exponentially decreasing character (straight line within a semi-logarithmic plot) instead of linearly decrease of the leakage rate for an increasing preload. This behavior matches the results obtained for variant I.I which provides the same geometrical properties as variant II.I.

Well knowing that the leak tightness usually increases with an increasing pressure, the pressure variation test is executed after reaching $1.19 \cdot F_{s,max,1}$ preload. The corresponding results are presented in figure 71 – red graph. As estimated it can be seen, that the leakage rate significantly drops after reaching a certain pressure between 30% to 60% MEOP. This behavior leads to two possible conclusions. Firstly, the force applied during the pre-coining inside the test jig with 350 N instead of 500 N might be not high enough to fully deform the coated metal layer. Only with the additional force by the applied pressure, the coated layer deforms enough. 30% MEOP pressure difference acting onto the area of the hydraulic diameter results in an additional force of $1.39 \cdot F_{s,max,1}$. Hence, minimal $2.58 \cdot F_{s,max,1}$ are required to deform the surface layer entirely. Secondly, the steeper sealing line due to the smaller poppet diameter might inhibit the self-centering and glide behavior into the seal seat. As the poppet's and seat's contact area is still a metal-metal connection, an additional axial force is required to fit the poppet into the seat's through hole. This can be the result of a larger deformation due to increased normal forces onto the seat. This second thesis will be validated later by the investigations on variant II.II. Nonetheless, after reaching higher pressures during the increasing pressure phase, the leakage rate remains almost constant at a very low level within the range of $10^{-3} \cdot \Phi_{req,OP}$ and $10^{-4} \cdot \Phi_{req,OP}$. Also, during the decreasing pressure phase, which constituted a critical phase during all previous tests, the leakage rate remains within this range. Finally, it can be stated, that the increased sealing capability improved by a decreasing diameter ratio of poppet and seat comes with the cost of a higher required preload.

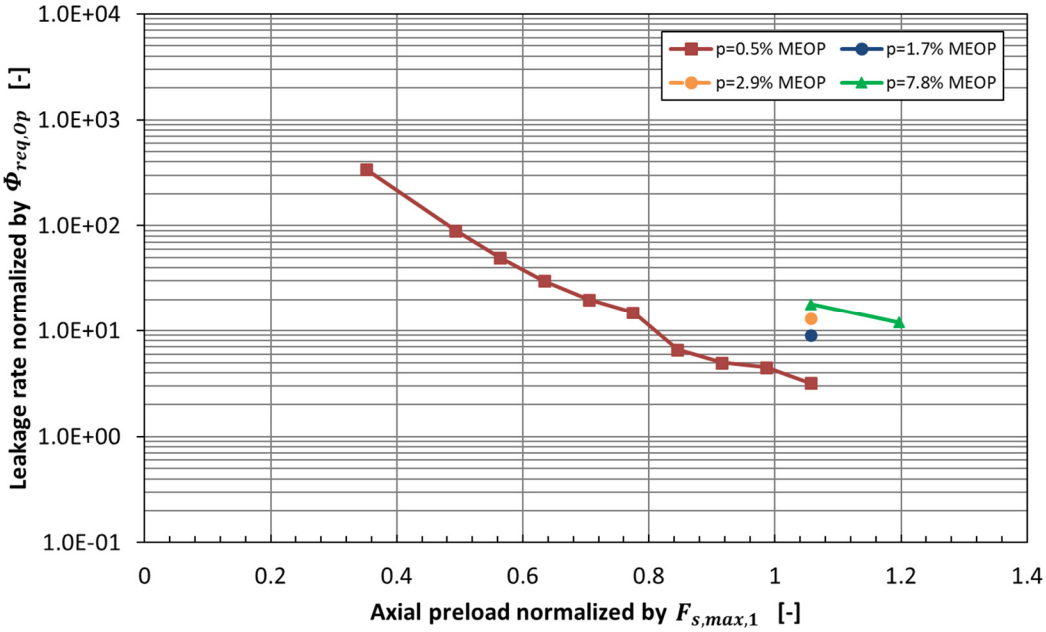

Figure 70: Preload determination test results variant II.I SN1

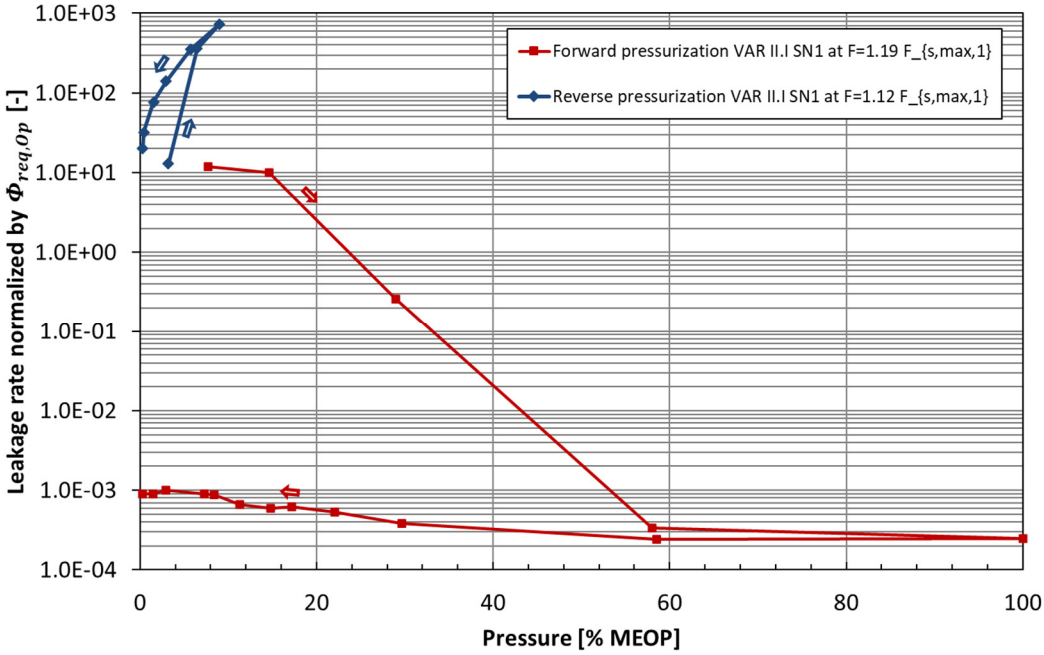

Figure 71: Forward and reverse leakage rate test results at ambient of variant II.I SN1

After the forward pressure test, the reverse pressurization test is conducted. Therefore, only the jig's upper interface is replaced by the vacuum bellow feedthrough. Especially seat and poppet are not disintegrated. Based on the findings from 5.1.1, two days hold time is kept ensuring a sufficient outgassing of all Variseals and the outer O-ring which has been exposed to GHe too.

At test beginning the behavior of the metal bellow feedthrough was quite uncertain in terms of influencing the applied preload force. That is why, special focus was on the acting force after implementation and during vacuuming the test device. Therefore, the bellow holder was not mounted in the first place to enable a full expansion of the bellow. Figure 72 shows the yield force measurement. Due to its compression at its implemented length, a force of 25 N is read before vacuuming already. As the bellow provides a quite large area of attack it gets sucked in into the jig during vacuuming and results in a force reading of 77.46 N at 1 bar differential pressure. This corresponds to a circular area of attack with a diameter of 31.4 mm and complies very well with the geometric dimensions of the bellow (33 mm

outside diameter [38]). This gives valuable insights on the influence of the vacuum feedthrough on the acting forces

After this determination, the bellow holder was mounted and an axial force of $1.12 \cdot F_{s,max,1}$ was applied onto the poppet. As the bellow is only specified for a maximum of 140 N against vacuum (200 N against atmosphere) the force is not further increased to not damage the bellow. However, by a preload determination test it is determined that this force is required to reach an initial leakage rate within the order of $10 \cdot \Phi_{req,OP}$. This especially equals $3.5^{-2} \cdot \Phi_{req,rev}$. The corresponding results of the reverse pressure test are shown in figure 71.

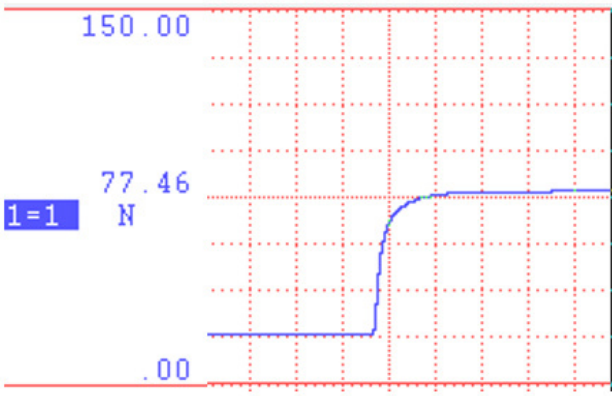

Figure 72: Force increase at reverse pressurization test during vacuuming due to expanding bellow feedthrough

The pictured graph clearly shows a strong dependency on the applied differential pressure. At a pressure of MEROP, the leakage rate yields $2.6 \cdot \Phi_{req,rev}$. Furthermore, the reverse leakage rate requirement (refer section 3.1.5) is exceeded at a pressure of 66% MEROP. During the decreasing pressure phase, the leakage rate decreases again. This, as well as the vacuum which was stable during the test at $3 \cdot 10^{-3}\ mbar$, indicates, that no macroscopic failure of the sealing occurred, but rather that the reverse pressurization enables a simple and very pressure dependent generation of microscopic leak paths. This and the generally high leakage rates already at very low pressures lead to the conclusion, that the current seal design is simply not optimal to withstand a reverse pressurization.

5.5.5 Variant II.II

As last seal variant the enlarged seat of material II.A coated with material II.B combined with the classic material II.A poppet of nominal diameter is investigated. These investigations are implemented at the end of this project enabling the use of the novel leak testing device. In total, three specimen SN1, SN3 and SN4 are subjects of the following studies. SN2 is rejected from further investigations as pre-test inspections under the microscope revealed significant scratches of the coating layer at the sealing line. Generally, the quality of the coating of this batch is very insufficient and therefore further outlined in the next subsection. Due to requirement exceeding results in the first place – particularly by SN1 – test procedures and especially the preprocessing of the specimen SN3 and SN4 are adapted to improve the sealing capability and further deduce important insights for a later implementation into a valve. An overview of all conducted tests and the particular processing of the specimens is given by the following table 26.

Table 26: Conducted leakage rate investigations on test articles of variant II.II

Test article	Processing	Tests conducted			
		#1	#2	#3	#4
SN1	• Externally coined in hydraulic press with 500 N acc. to 5.4.1. • Flexible bellow during vacuuming	Reverse pressure variation and preload determination at ambient	Forward pressure variation and preload determination	--	--
SN2	Rejected due to scratches				
SN3	• Internally coined in test jig with 345 N to prevent twisting • Flexible bellow during vacuuming	Forward pressure variation and preload determination at ambient	Reverse pressure variation and preload determination at ambient	--	--
SN4	• Externally coined in hydraulic press with 500 N acc. to 5.4.1. • Fixed bellow during vacuuming	Forward pressure variation and preload determination at ambient	Forward pressure variation at minimal temperature	Forward pressure variation at maximal temperature	Reverse pressure variation at ambient temperature

As listed, SN1 is subject of the reverse pressurization scheme in advance to a forward pressurization. This is decided to preserve the Variseals inside the test jig from saturation. However, the forward pressurization test has to be aborted due to high leakages potentially damaging the mass spectrometer. As a possible reason a twisting of the test articles during the integration into the test jig is assumed. Therefore, and similar to variant II.I SN1, SN3 is coined inside the test jig and the forward pressure variation test is conducted first. To ensure a sufficient coining effect SN4 is externally pre-coined again and subject of three forward pressurization tests at ambient temperature and thermal extrema. To improve the sealing capability during the reverse pressurization, this time the preload onto the poppet applied by the bellow feedthrough is set and fixated already in advance of vacuuming the upper part of the test device. This eventually demonstrates a significant effect and results in a fulfillment of all requirements.

Coating layer quality

As briefly mentioned above, the quality of the coated surface on the seat is evaluated as very insufficient and unsatisfactory at this lot of variant II.II. The following figure 73 shows some imperfections photographed during the microscopic inspections in advance of all tests. As SN1 exhibits a droplet right beneath the sealing area, SN2 shows two significant scratches while one of it is located right at the sealing line. At the sealing line of SN5 apparently organic residuals from the coating process are identified. Yet the worst condition of the surface layer is detected at SN6. Here a significant detachment of the layer from the seat can be seen. If such a detachment occurs at the layer of a real valve this might result in fatal consequences for the valve itself and for the entire propulsion system. If propellants get between the layer and the housing, the layer might spall off entirely. Firstly, this would cause a malfunction of the valve and furthermore would contaminate the fluids with solid pieces of material II.B which can initiate further failures within the propulsion system such as blocking of a fluid path.

While the quality of the coating layer is sufficient for the basic investigations herein, especially considering further preprocessing surface treatments such as polishing and coining, it has to be stated clearly, that the quality needs to be highly improved for later qualification and flight models. In cooperation with the coating manufacturer and the internal quality insurance it is recommended to elaborate a procedure to ensure a constant and high quality of the coating.

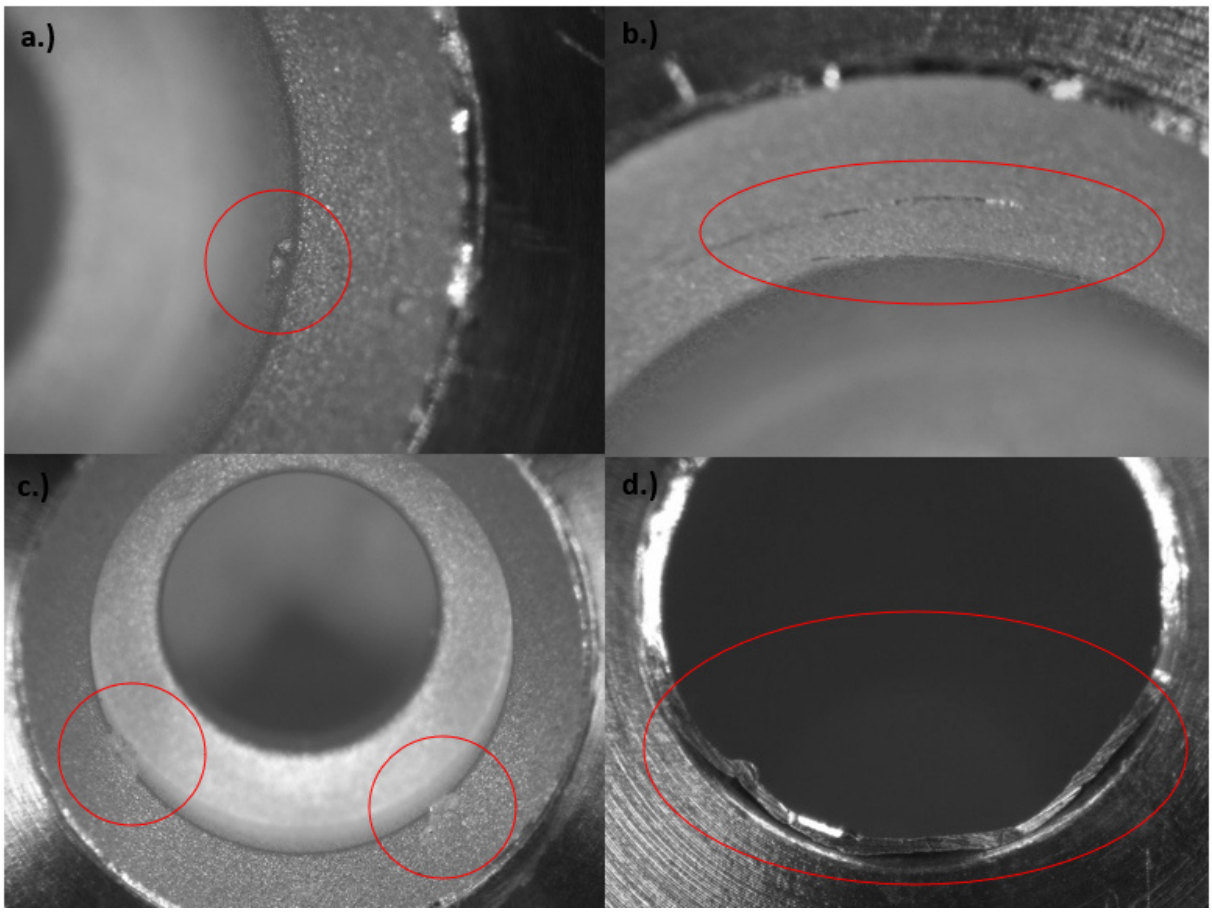

Figure 73: Examples of coating layer imperfections of variant II.II: a.) SN1; b.) SN2; c.) SN5; d.) SN6

Forward pressurization

In the following subsection the leakage rate measurement results of SN3 and SN4 during a forward pressurization are presented. As mentioned above and depict in table 26, SN3 is pre-coined within the leak testing device with a force of 345 N, whereas SN4 is pre-coined externally with 500 N. The following figures 74 and 75 illustrate the obtained results during the preload determination and pressure variation tests.

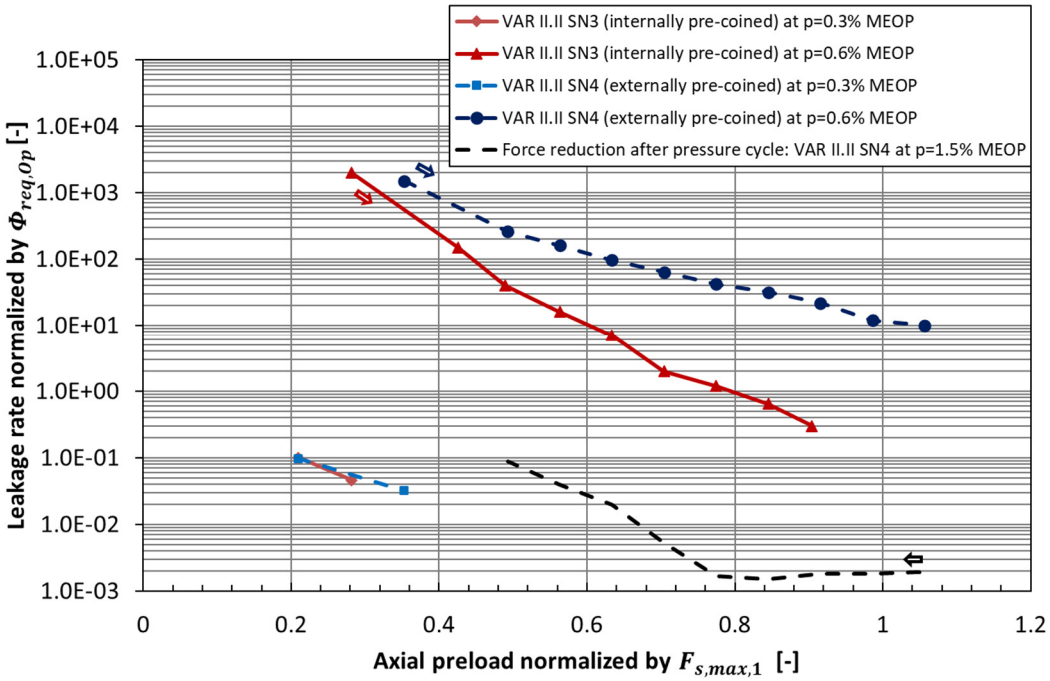

Figure 74: Preload determination test results variant II.II SN3 and SN4

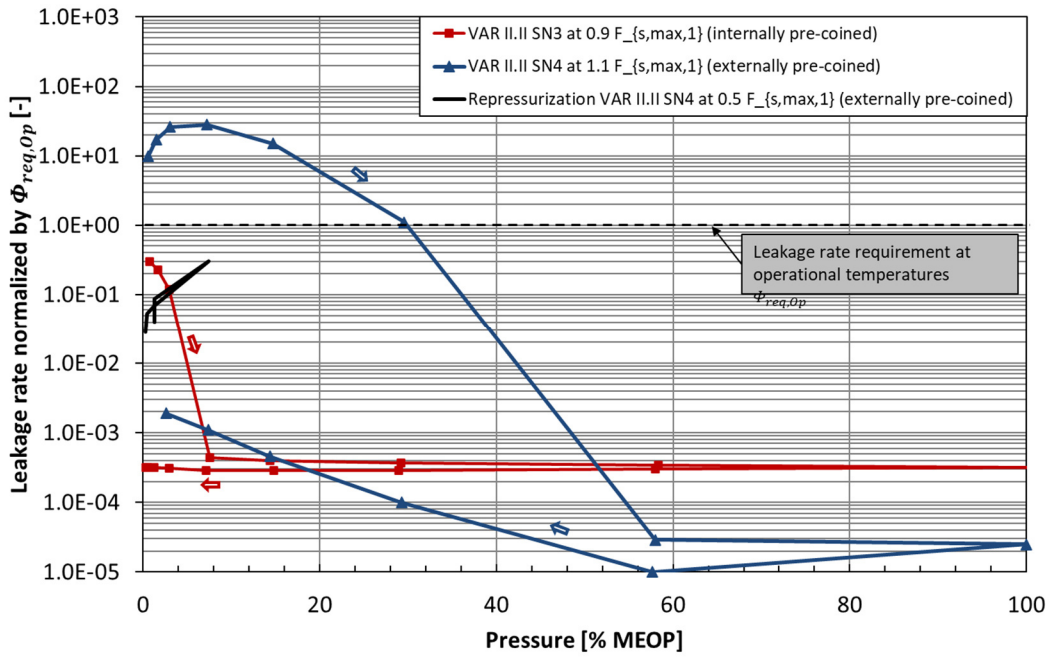

Figure 75: Forward leakage rate test results at ambient temperature of variant II.II SN3 and SN4

From these figures it can be seen that an internal pre-coining in advance of the tests improves the seal's sealing capability and especially increases the negative gradient of the preload determination graph. This results in a better leak tightness at lower preload forces (compare SN3 at $0.9 \cdot F_{s,max,1}$ and SN4 at $1.1 \cdot F_{s,max,1}$). SN3 in particular, meets the leakage rate requirement $\Phi_{req,OP}$for operational temperatures throughout the entire pressure domain and demonstrates a very stable leak tightness also during the

critical decreasing pressurization phase. However, both specimens exhibit a significant drop of the leakage rate at medium pressures. After this drop the leakage rate always remains at a low level. Subsequent the complete forward pressure test of SN4, its preload force is reduced stepwise until $0.5 \cdot F_{s,max,1}$ at an applied pressure of 1.5% MEOP. Both figures above illustrate the corresponding leakage rates measured (black graph). SN4 provides a sufficient leak tightness at the critical pressures between 10% MEOP with even half of the initial preload. The leakage rates stay within the requirement. Three important conclusions can be drawn from the obtained results:

- As the preprocessing results from SN4 eliminates the possibility of an insufficient coining effect potentially caused by an internal pre-coining with less force, the corresponding results show that an internal pre-coining improves the leakage rate significantly especially at low pressures. This is probably due to a reduction of influence of manufacturing tolerances.
- The poppets of variant II.II require an additional force – which is applied by the increasing pressure in this case – to glide and settle into the seat. This behavior also occurred at variant II.I SN1 already. As variant II does not demonstrate this behavior, it is probably caused by a steeper contact line. Higher normal forces at the sealing line result in a larger deformation of the coating layer, which again results in a larger movement of the poppet in axial direction until it comes to rest in the seat.
- Once the poppet is fit into the seat, the sealing capability is improved (compared to variant II) and provides very low leakages mostly below a value of $10^{-3} \cdot \Phi_{req,Op}$ throughout the entire pressure domain. Even after a preload reduction from $1.1 \cdot F_{s,max,1}$ to $0.5 \cdot F_{s,max,1}$ the leakage rate requirement is not exceeded.

After the ambient test of SN4, the test article was subject of 2 further forward pressurization tests, one at the defined minimal temperature $T_{Q,g,min}$ and one at the maximal temperature $T_{Q,g,max}$. Therefore, the test jig is placed and installed inside a thermal chamber according to 5.4.4. The test articles are not disintegrated between the tests. As the previous test has demonstrated the seal's capability to meet the leakage requirement even at lower preload forces, the thermal tests are conducted with a set preload of $0.63 \cdot F_{s,max,1}$. Figure 76 illustrates the obtained leakage results.

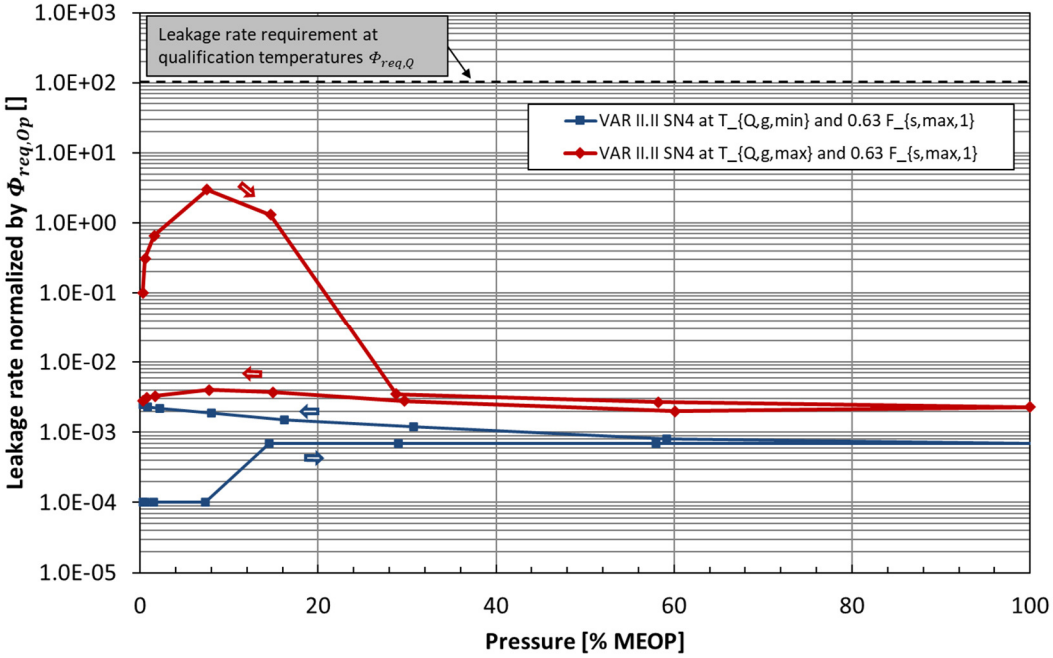

Figure 76: Forward leakage rate test results at thermal extrema of variant II.II SN4

Similar to the obtained results for variant II at a minimal temperature, the leakage rates of variant II.II SN4 remain constantly low at around $10^{-3} \cdot \Phi_{req,Op}$ throughout the entire pressure domain. At the

maximal temperature however, variant II.II demonstrates significant lower leakage rates than variant II. The diagram further shows that the measured leakage rates remain mostly several orders of magnitude lower than the specified leakage rate requirement for qualification temperatures.

Reverse pressurization

This subsection summarizes the obtained results for the test articles SN1, SN3 and SN4 of variant II.II. Figure 77 illustrates the corresponding leakage rates. It can clearly be seen, that SN1 and SN3 provide a similar pressure dependent behavior resulting in the violation of the reverse leakage rate requirement between 10% and 50% maximum reverse pressure. As explained for variant II.I and briefly mentioned in table 26, during the vacuuming process of SN1 and SN3, the bellow is left unfixed and flexible. Afterwards, the force is increased stepwise. With the findings of the previous tests on the settlement behavior of the seal, it is assumed that the vacuuming loosens the poppet-seat fit which was obtained by a previous forward pressurization test. Therefore, at SN4 the preload is applied by fixating the bellow feedthrough in advance of vacuuming the test jig. As the green graph of SN4 indicates, this eliminates the previous issue of an increasing leakage rate. During the entire reverse pressure test of SN4 its leakage rate remains well below the reverse leakage requirement. Although meeting the requirement now, it still needs to be mentioned, that all reverse leakage rates even at low differential pressures yield much higher than all obtained forward leakage rates.

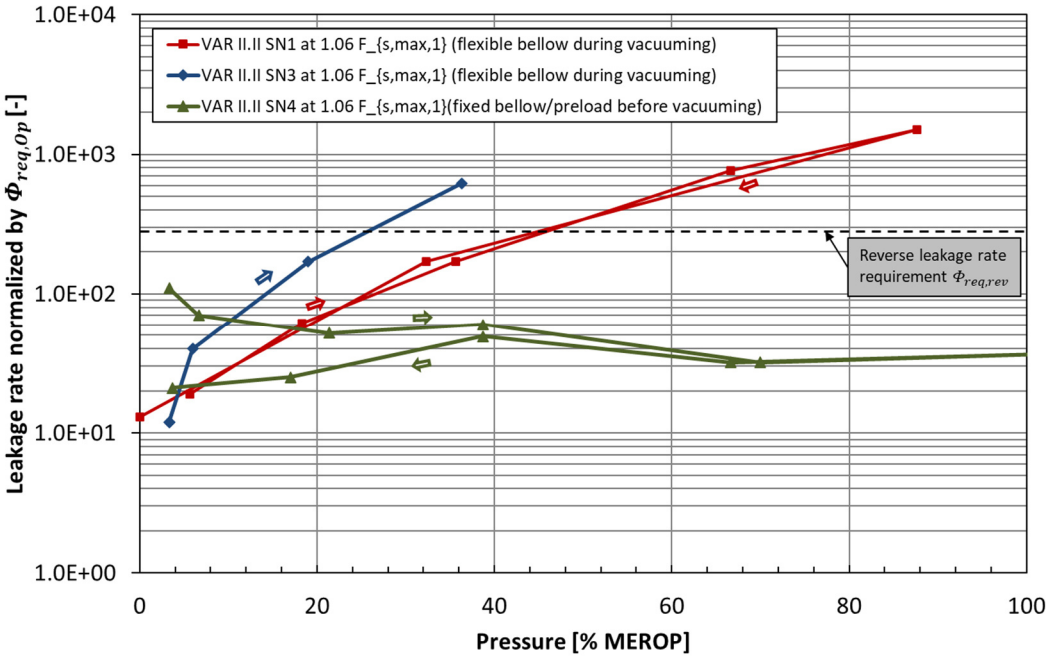

Figure 77: Reverse leakage rate test results at ambient temperature of variant II.I SN1, SN3 and SN4

5.5.6 Summary

Concluding chapter 5 about the experimental investigations on the valve's internal seal, this subsection gives a brief overview of the obtained test results which are outlined above in greater detail. Applying a ranking scheme according to table 28, a comparison of the test results and an evaluation of the seal variants' suitability for the NO SMAV is presented in table 27.

Table 27: Summary of leakage test results and assessment of seal variant applicability for the NO SMAV

Requirement	Variant I.II		Variant II	
	Evaluation	**Rating**	**Evaluation**	**Rating**
Forward leakage rate at ambient temperature	Leakage rates between $\Phi_{req,Op}$ and $10^2 \cdot \Phi_{req,Op}$	-	- Leakage rate between $\Phi_{req,Op}$ and $10^{-2} \cdot \Phi_{req,Op}$ - Critical at low pressures	+
Forward leakage rate at minimal qualification temperature	n/a		Stable leakage rate at $10^{-3} \cdot \Phi_{req,Op}$	++
Forward leakage rate at maximal qualification temperature	n/a		- Leakage rate between $\Phi_{req,Op}$ and $10 \cdot \Phi_{req,Op}$ - Exceeds operational requirement while fulfilling qualification requirement ($10^{-1} \cdot \Phi_{req,Q}$)	+
Reverse leakage rate at ambient temperature	n/a		n/a	
Maximal preload of $F_{s,max,1}$	Required preload exceeds $F_{s,max,1}$ by far	-	$0.5 \cdot F_{s,max,1}$ is the lowest required preload of all variants	++

Requirement	Variant II.I		Variant II.II	
	Evaluation	**Rating**	**Evaluation**	**Rating**
Forward leakage rate at ambient temperature	- Steeper contact angle increases normal forces, which results in a larger deformation and larger width of the sealing line - After settlement stable leakages at $10^{-3} \cdot \Phi_{req,Op}$ are achievable	++	- Steeper contact angle increases normal forces, which results in a larger deformation and larger width of the sealing line - After settlement stable leakages at $10^{-3} \cdot \Phi_{req,Op}$ are achievable	++
Forward leakage rate at minimal qualification temperature	n/a		Stable leakage rate at $10^{-3} \cdot \Phi_{req,Op}$	++
Forward leakage rate at maximal qualification temperature	n/a		- Leakage rate at $10^{-2} \cdot \Phi_{req,Op}$ - Slight increase at low pressures, but no requirement violation	++
Reverse leakage rate at ambient temperature	- High initial and pressure dependent leakage rates above $10 \cdot \Phi_{req,Op}$ - Requirement violation at 33% MEROP - Needs to be repeated with fixated preload before vacuuming	o	Requirement fulfilled after adaption of test procedure (fixed bellow feedthrough)	+
Maximal preload of $F_{s,max,1}$	Due to larger deformation and steeper contact angle an additional force is required to enable a settlement into the seat	o	- Due to larger deformation and steeper contact angle an additional force is required to enable a settlement into the seat - It is demonstrated that 0.5 to $0.63 \cdot F_{s,max,1}$, are enough to meet the requirements after settlement	o

Table 28: Ranking scheme applied for seal variant applicability assessment

Ranking	Description
++	- Requirement well fulfilled with a certain safety factor - Suitable for the NO SMAV without any restrictions
+	- Requirement tightly fulfilled
o	- Requirement partially fulfilled and/or only under certain prerequisites regarding test procedures and preprocessing - Further investigations should be conducted
-	- Requirement is not be fulfilled - Not suitable for the NO SMAV

The experimental investigations demonstrated an improvement of the sealing capability with an increasing sealing angle between poppet and seat. However, this improvement comes with the cost of a poorer glide and settlement behavior due to increased normal forces and a larger plastic deformation. It is found that the reverse leakage rate requirement can be fulfilled under the prerequisite of a previous full settlement of the poppet into the seat. The importance of pre-coining and the implementation without any twist is demonstrated again. All these findings affect other components of the valve as well. The notched tube for example should be equipped with an anti-twist mechanism. The applicability of the proposed spring must be checked. These considerations are presented within the conclusion of chapter 7.

A further finding of this chapter is the insufficient quality of the seat's coated surface. The potentially harmful consequences of surface imperfections and especially of a layer detachment are outlined above. During a further development, a procedure to increase and ensure the quality should be elaborated.

Lastly, it can be stated that the novel developed leakage test device worked smoothly and fulfilled all specified requirements during all application cases. Especially the long duration background leakage rate is improved significantly below $10^{-3} \cdot \Phi_{req,Op}$. The saturation of O-rings and Variseals only needs to be considered when conducting a reverse leakage test right subsequent a previous forward leakage test. Here two days hold time should always be implemented to enable a sufficient outgassing of Helium.

6. Hydrazine compatibility

So far, the previous chapters have concentrated on the development of the SMAV NO and its single components. All design optimizations have been evaluated considering their functionality and feasibility by utilizing analytical, numerical and experimental methods. However, the compatibility of the valve to enable the safe use of explosive propellants and especially hydrazine has not been considered yet in greater detail. Within the chapter 3 which covers the valve's requirements, the compatibility to hydrazine at both liquid and vapor phases has been postulated as an important requirement. Therefore, this chapter now subjects investigations on this very compatibility and outlines the reasons for the above stated requirement. Thereby, it mainly concentrates on the compatibility of the valve's working principle to hydrazine, than instead of the chemical resistance of the valve's materials. To gain a broad overview on the potential threats caused by the actuation of a SMAV, firstly an extensive literature research is conducted on this issue. The identified threats due to elevated feed line temperatures, as well as to adiabatic compression are presented and evaluated in the following. Later on, to validate the found results, experimental investigations on the already developed SMAV NC are conducted. These investigations concentrate on the above mentioned threats on actuating the valve while it conveys hydrazine. The corresponding results are presented in section 6.2.

6.1 Decomposition and explosive properties of hydrazine

6.1.1 Thermal decomposition

Hydrazine constitutes an endothermal compound consisting out of nitrogen N_2 and hydrogen H_2. Its molecular formula yields N_2H_4. Due to its endothermal character, a release of energy during thermal decomposition is highly expectable. This exothermic decomposition is a complex mechanism consisting out of various sub reactions. However, the homogeneous decomposition can be described by summarizing two main reaction equations. Both equations describe the process of decomposition with the absence of any chemical reaction but under the influence of heat [47].

$$3\ N_2H_4 \longrightarrow 4\ NH_3 + N_2 \tag{6.1}$$

$$N_2H_4 \longrightarrow N_2 + 2\ H_2 \tag{6.2}$$

$$\Rightarrow\ 3\ N_2H_{4(l,g)} \longrightarrow 4(1-x)NH_{3(g)} + (1+2x)N_{2(g)} + 6x\ H_{2(g)} \tag{6.3}$$

From (6.3) it can be seen that hydrazine decomposes into ammonia NH_3, nitrogen and hydrogen. Due to its exothermal properties, the thermal decomposition can potentially cause a thermal runaway [48]. This thermal runaway can result in a pressure multiplication up to the 14-fold [47][48]. This would have fatal consequences for a spacecraft. Furthermore, the compound of hydrazine is highly reactive at both conditions, with and without the absence of oxidizer. In detail, hydrazine vapor does not exhibit an upper explosion limit, which means that also 100 % pure hydrazine is flammable and self-igniting [47][48]. Especially hydrazine vapor provides such an increased risk [7][48]. Besides oxidizers, some metallic materials such as Pl, Fe, Cr, Mo and Cu catalyze the decomposition strongly [47][48]. The most dominating influence on the decomposition rate is given by the temperature. Up to a temperature of 300°C, the hydrazine decomposition rate provides a quite stable and linearly dependency on the temperature – it follows the Arrehnius equation [49]. Above this threshold value however, catalytic effects gain dominance. Besides the wall material and the temperature, the pressure provides an important influence too [47]. Within equation (6.3) it is indicated that all products occur at gaseous state. Hence, it is evident, that an increase of the surrounding pressure decelerates the decomposition [47]. The influence of the pressure on the vapor phase's decomposition rate at a temperature of 205°C is indicated in figure 78. From this figure it can clearly be identified that a pressure between 20 and 30 bar

significantly reduces the rate of decomposition and hence the threat of a thermal runaway. In fact, a slow heating of hydrazine within a pressurized environment constitutes no large risk [47].

Hydrazine changes its state from liquid to gaseous phase by crossing the line of vapor pressure. This line, as well as the corresponding liquid phase density is illustrated by figure 79. From this graph it can be stated, that the nominal boiling point of hydrazine at atmospheric pressure, yields 114°C. Due to falsifications and hazards by thermal decomposition at higher pressures and temperatures, data on the vapor pressure above the normal atmospheric pressure is very rarely published. However, the red graph constitutes a valuable approximation [18]. This graph illustrates further, that several hundred °C are required to boil hydrazine under pressurized conditions between 20 and 30 bar.

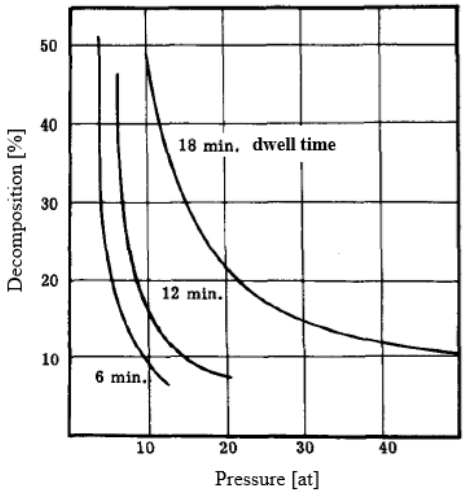

Figure 78: Thermal decomposition rate of hydrazine vapor as a function of pressure and dwell time at 205°C [47]

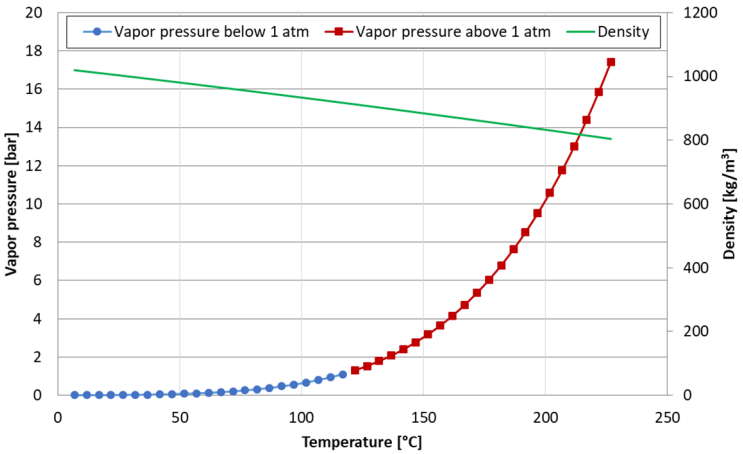

Figure 79: Thermophysical properties of pure hydrazine - data from [18]

6.1.2 Explosive properties

Besides the risks from a thermal decomposition of hydrazine, as a high energetic compound, hydrazine also provides explosive properties. Considering explosive events, some distinctions need to be stated in advance. As the explosion mechanisms of liquid and gaseous hydrazine hugely differ, these issues are discussed separately. Furthermore, three potential occurring events need to be distinguished: Deflagration, detonation and explosion. These events mainly differ in terms of occurring pressure peaks and reaction velocities. While detonations follow the Chapman-Jouget (C-J) equation, explosions can be initiated by either a deflagration or detonation.

By comparing various tests on the explosive potential of gaseous hydrazine, it can be stated, that hydrazine vapor at ambient pressure and nominal boiling point of 114°C is able to deflagrate. Rarely, this deflagration flame can also merge into a detonation [18]. If it does so, overpressures have been measured that greatly exceed the expected overpressures according to C-J. The enabling mechanism is identified as the shock wave amplification of coherent energy release (SWACER). This mechanism describes the coupling of chemical energy release and the propagating shock wave [7].

The detonation behavior of pure liquid hydrazine was investigated under various conditions, but mostly by external ignition of the compound within a straight metallic tube of a certain diameter length. Arbitrary of the test set-up, in most cases a detonation could not be observed [18][47]. However, some dependency on the tube material has been identified. If liquid hydrazine is preheated and carried into a yet hotter tube section of >200°C made out of stainless-steel CRES-304L, the set-up does explode [18]. The sole other case identified, at which a detonation can occur potentially, constitutes the presence of gas bubbles inside the liquid phase [18].

Furthermore, from drop weight and bullet impact investigations found in literature, it can be postulated that pure liquid hydrazine is not sensitive to shocks [18][47][48].

6.1.3 Adiabatic compression

Potential sources of gas bubbles in a hydrazine propellant system aboard a spacecraft are manifold. Hydrazine decomposition, propellant supersaturation or the introduction during fueling constitute exemplary sources [7]. Boiling due to hot feed lines has also been identified as a potential source for such bubbles [18], as well as the pressurization with inert gas such as GHe or GN_2[6]. The most critical aspect considering these phenomena, is the high potential of detonations due to rapid gas compression. Experimental investigations have shown that the occurrence of such detonations is highly dependent on the compression rate and the hydrazine's initial temperature. Figure 80 illustrates the explosion thresholds found by two experimental sequences, one conducted by Aerojet, the other one by NASA White Sands Test Facility (WSTF). As the test methods of both institutions did differ, so do the respectively gained results too. WSTF set up experiments which enabled the separated investigation of adiabatic compression. Aerojet contrary, set up U-tube tests at which a coupling of the adiabatic compression with occurring shock wave phenomena was investigated. The occurring detonations follow the above described SWACER mechanism. It can clearly be identified, that the SWACER like detonations provide a far lower threshold for both, compression rate and initial temperature. Due to rapid valve opening and closing, accelerating of fluids and geometric features which trap vapor bubbles, a propulsion system onboard a spacecraft does not provide conditions enabling a singularly adiabatic compression, but rather the combination of shock waves and adiabatic compression following the Aerojet investigations [7]. Based on the test results of figure 80, [7] provides some limitations and recommendations to ensure safety and reliability of hydrazine propulsion systems:

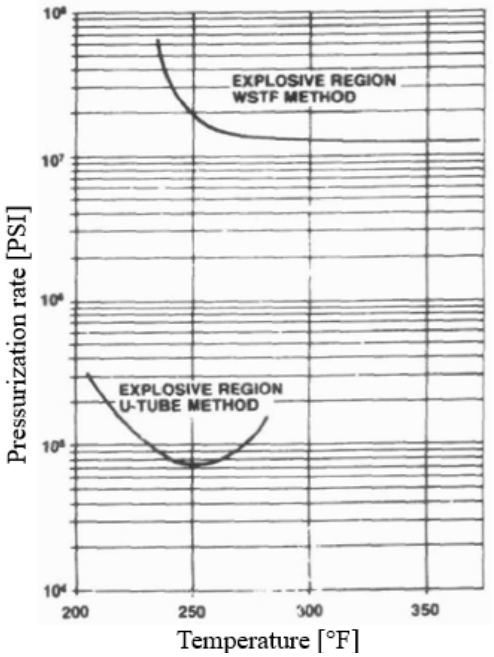

Figure 80: Explosion regimes of liquid hydrazine containing bubbles [7]

- Maximal temperature of 200°F (93.3°C) during periods of rapid pressure oscillations
- Maximal compression rate of 50000 psi/s (3447.4 bar/s)
- Minimize the amount of bubbles within the propellant system

Furthermore, the AIAA (American Institute of Aeronautics and Astronautics) postulates the correlation that an adiabatic detonation of a mixture consisting of hydrazine vapor and helium bubbles only occurs for a ratio by volume of larger than 20 % [6].

6.1.4 Elevated feed line temperatures

Due to various objectives, usually many electrical heaters are integrated into a space vehicle's propulsion system. Common purposes are for example the thermal control of feed lines or respectively the actuation of valves. Electrical heaters provide a failure mode potentially threatening the entire system's integrity. If a heater exhibits a malfunction and is unable to shut off, in the worst case, all electrical power dissipates into the feedline and its conveyed media. This can result in a temperature rise above the nominal operating temperatures (ref. 3.1.2) [49]. The determination of hazardous effects and influences on thrusters operated with hot propellants is the subject of this section.

Explosive hazards

Experimental investigations on elevated feed line temperatures conveying hydrazine pressurized by nitrogen have been conducted by Lockheed. These tests have shown, that no explosive events occur up to feed line temperatures up to 510°F (266°C). However, an explosive risk exists due to contamination and external ignition by sparks or other high energy sources, but the hot feed line itself does not initiate such explosions. While the thermal decomposition rate up to 450°F (232°C) followed the Arrehnius equation as expected (ref. 6.1.1), no exothermal runaway could have encountered. Furthermore, the operation of hydrazine monopropellant thrusters with an elevated feed line temperature did not cause any explosive events too [49].

Performance influence

Although the operation of monopropellant hydrazine thrusters with elevated feed line temperatures have not shown any hazardous explosive events, it did demonstrate effects on the thrusters' performances. As described above, elevated temperatures induce thermal decomposition and vaporization of hydrazine. The result is an accumulation of bubbles of hydrazine vapor and decomposition products inside the feedline. With starting up a thruster, this leads to a momentary reduction of thrust up to 10% [49]. In some tests, the ignition also showed a slight delay [48]. This gains importance especially considering pulsed mode firing to initiate orbital maneuvers of a very specific Δv. Also the calculated propellant budget for a maneuver gets effected by this [49][50]. As long as the power of the malfunctioning heater does not exceed the heat needed to vaporize the entire mass flow, subsequently liquid hydrazine is fed to the thruster again and stabilizes the nominal thrust [49]. All investigated thrusters did not exhibit remaining damages or long term performance declines [50].

6.1.5 SMAV operation risk assessment

From the outlined literature results on the explosive and decomposing behavior of hydrazine some important conclusions for operation of the SMAV can be drawn. As the transformation start temperature of the NiTiNol actuator lies around 94°C it seems most likely, that the media inside the valve reaches a temperature just below this value as well. This holds especially true, if the entire valve is filled with hydrazine at rest prior to actuation. While this does not result in a boiling effect, it indeed does result in a slight decomposition rate of around than 0.5 bar pressure increase over 24 hours (at around 20 bar system pressure) [49]. However, this does not enable a thermal runaway. A feed line pressure as high as possible reduces the decomposition rate further. Additionally, as no boiling occurs during nominal actuation and as thermal decomposition remains negligibly limited, no significant decrease of thruster performances needs to be expected.

The greatest risk on operation of a SMAV constitutes its actuation itself. As identified, the valve's actuation temperature exceeds the recommended temperature considering adiabatic compression. Hence, a detonation induced gas bubbles on rapid closing or opening of the valve brings a potential risk. However, it is not likely, that the required compression rates for this scenario of above 3447 bar/s are induced by a SMAV actuation. Nevertheless, it might be reasonable to determine the compression rates of gas bubbles on SMAV actuation experimentally.

If a heater malfunction of the SMA valve would occur, temperatures far above the nominal actuation temperatures can theoretically be reached. As long as the ignition from an external source can be excluded, feed line temperatures up to 266°C do not pose a potential risk. However, in this case, an ignition delay of the thruster as well as a momentary thrust reduction need to be considered regarding propellant budgets and certain Δv.

Table 26: Risk assessment summary

Potential risk	Evaluation
Thermal runaway	Increased system pressures significantly decrease thermal decomposition rates. Slow heating of hydrazine feed lines up to 300°C (threshold for linearly increase of decomposition rate) does not provide a risk of thermal runaway
Deflagration of hydrazine vapor	Deflagration of hydrazine vapor is potentially possible. However, with higher system pressures the vapor pressure increases exponential. This results in a higher required temperature to vaporize liquid hydrazine
SWACER detonation of hydrazine vapor due to adiabatic compression	Although the recommended maximal heating temperature might be exceeded on actuation, the required high compression rate for detonation is most likely not be reached. Further, a volume ratio of >20% hydrazine vapor to helium does not occur considering operation scenarios for NO and NC valves [6]
Detonation of liquid hydrazine	If not ignited by an external mechanism such as a spark, liquid phase hydrazine does not detonate
Hazards on system integrity due to elevated propellant temperatures	Experimental investigations conducted by Lockheed have demonstrated, that no explosive hazards exist due firing thrusters fed with hydrazine at elevated temperatures
Performance influences due to elevated propellant temperatures	Due to potential decomposition and vaporization of liquid hydrazine, momentary performance declines need to be considered regarding propellant and Δv budgets.

6.2 NC SMAV actuation tests

The experimental investigations presented within this chapter concentrate on the NO SMAV's counterpart, the NC valve. This valve already provides a higher TRL and will soon be integrated into its first satellite. Due to specific customer requests and additionally due to the above outlined concerns on rapid pressure oscillation within hot feed lines, the NC valve is subject of further qualifying experiments herein. To preserve clarity and to limit the extent of this thesis, the following section presents just exemplary and summarized results.

6.2.1 Test plans

The qualification campaign with hydrazine herein comprises the investigations on three SMAV NC models which are already qualified for the use with gases, MMH and MON. All three valves are investigated under realistic environmental conditions and while carrying liquid hydrazine. According to the numbering of previous qualification tests, the investigated test articles are referred to as QM06, QM07 and QM08. To increase the plurality of the insights gained from the investigations, the valves are tested under different conditions. This way various test objectives can be realized. An overview over the test conditions and their respective objectives can be found in table 27. As specimen QM08 was subject of tests post the actual actuation as well, the additions (A) and (PA) indicate the *actuation test* and *post actuation test* respectively.

Table 27: Envisaged tests on NC SMAV actuation

Test article	Initial temperature [-]	Initial inlet pressure [% MEOP]	Initial outlet pressure [% MEOP]	Heater power [W]	Objectives
QM06	Ambient	8.5	Vacuum	12.0 – 12.6	Nominal actuation from ambient
QM07	$T_{Op,l,max}$	8.5	1 bar GN_2	13.4 – 13.6	Fast actuation from highest operating temperature
QM08 (A)	$T_{Op,l,min}$	8.5	8.5	9.9 – 10	Slow actuation from lowest operating temperature
QM08 (PA)	Ambient	8.5	8.5	9.8 – 10	Feed line heating post actuation

QM06:

As indicated in the table, the test of specimen QM06 constitutes the nominal actuation test of the valve. The valve is heated with nominal heater power of 12 W from ambient temperature. As nominal for the NC valve, the hydrazine is only present at the valve's inlet port. Here it is pressurized to 8.5% MEOP by utilizing GN_2. This test shall demonstrate the basic ability of the valve to open under nominal conditions within a hydrazine environment. Furthermore, the required nominal actuation time, as well as the induced shock due to the actuation are desired output parameter. To gain a detailed result on the heat distribution, the valve is equipped with 8 thermocouples at various positions. Furthermore, one Pt100 thermistor is attached to the valve's housing. This installation matches the later flight version and therefore constitutes the reference temperature for this test. The positioning of two redundant thermistors is indicated by figure 81.

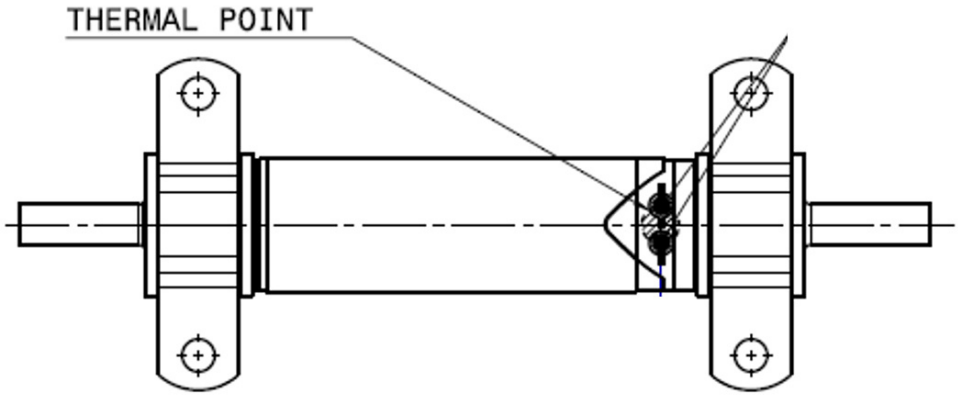

Figure 81: Positioning of thermistors for NC SMAV actuation tests

As discussed earlier, the induced shock at opening of the valve states an important requirement. Therefore, the valve is also equipped with three accelerometers which are able to measure the occurring shock loads. One of these sensors is located at the valve's housing itself, the second one at the valve's mounting bracket and the third one at the plate on which the valve is fixated. This way the propagation of the induced shocks throughout the valve and its mechanical interfaces can be determined. As the opening of the valve requires only several milliseconds, a data acquisition system is utilized which enables a very high sample rate to ensure a correct time resolution.

QM07:

Indicated by table 27, the valve QM07 is subject of a test which is supposed to determine the minimal actuation time. Therefore, the valve is heated from $T_{Op,l,max}$ by applying the maximal heater power. This way the potential threat of an unwanted too fast actuation can be determined. The hydrazine again is present at the valve's inlet port, however this time ambient pressure from around 1 bar GN_2 is applied to the outlet port. The instrumentation for this test equals the test of QM06.

QM08:

As QM07 is supposed to determine the minimal actuation time, QM08 shall similarly demonstrate the maximal actuation time. To implement the worst case scenario, this time the valve is preconditioned to an ambient temperature of $T_{Op,l,min}$ while the heater power is restricted to the minimal available power of 10 W. Due to considerations on system level, customers identified a critical case for the valve actuation, at which the NC valve pre actuation is already filled with hydrazine from both sides, the inlet and the outlet port. According to this scenario, this test is implemented the way, that hydrazine is pressurized to about 8.5% MEOP at both ports while the valve is closed. Hence, on actuation, no significant pressure gradient needs to be overcome and no sudden flow of hydrazine occurs. This might influence both, the maximal occurring shock loads, as well as the temperature dissipation into the feed line.

Regarding the identified concerns due to elevated temperatures of feed lines, QM08 is investigated further after the actual actuation. Therefore, the opened valve is slowly cooled down to room temperature and subsequently heated again for more than one hour. This especially constitutes a simulation of the identified critical heater malfunction and continuously heating. By holding the hydrazine inside the feed line at rest and not enabling a fluid flow, the valve is not cooled by running liquid phase hydrazine. Therefore, it is expected, that the hydrazine might be subject of vaporization and thermal decomposition. This behavior is investigated by measuring the pressure increase over the test period.

6.2.2 Test results

As mentioned earlier, herein only selected test results from QM06, QM08 (AP), as well as plots comparing all three specimens are discussed.

QM06:

Figure 82 presents the test results on the actuation of test article QM06. The time axis starts at the value zero when the heater is switched on. At the legend, all 8 thermocouples can be identified. Furthermore, the reading of the Pt100 thermistor is given by the graph T_{ref}. At the second ordinate, the pressure at the valve's outlet port is visualized. From the diverging readings of all temperature graphs, the dissipation of the induced heat can be identified. As TH1 and TH2 are installed directly onto the heater, the reading from T_{ref} does not constitute the highest value but remain still a representative value for the NiTiNol actuator inside. The opening of the valve can clearly be identified by the sudden drop of temperatures. This temperature drop is caused by enabling a flow of cooler liquid hydrazine through the valve at opening. This hydrazine instantly cools the valve significantly several degrees. The opening of the valve also can be seen by considering the presented outlet pressure. Its sudden and shock-like increase at the valve's opening is clearly visible. As the heater is powered for 30 min in total, an increase of the temperatures post actuation is shown as well.

Further, by analyzing the readings from accelerometers, the occurring shock loads can be evaluated. The results on the self-induced shock loads are presented in figure 83. Generally, the occurring shock phenomena proceeds within only a few milliseconds. However, two peak shocks are identifiable. It is assumed, that the first main ((-)19.2% $S_{req,valve}$) results due to the actuator's expansion and subsequent rupture of the notch. The second peak and global maximum ((+)19.8% $S_{req,valve}$) might be caused by the impact of the ruptured notched tube onto the valve's rear housing. This is caused by the applied pressure difference of 8.5% MEOP. The maximal shock load which is transduced towards the valve's brackets already yields less than at the valve itself: 23.7% $S_{req,I/F}$. The eventually load onto a spacecraft's subsystem is represented by the accelerometer at the valve's mounting plate and results to a maximum value of 8.3% $S_{req,I/F}$..

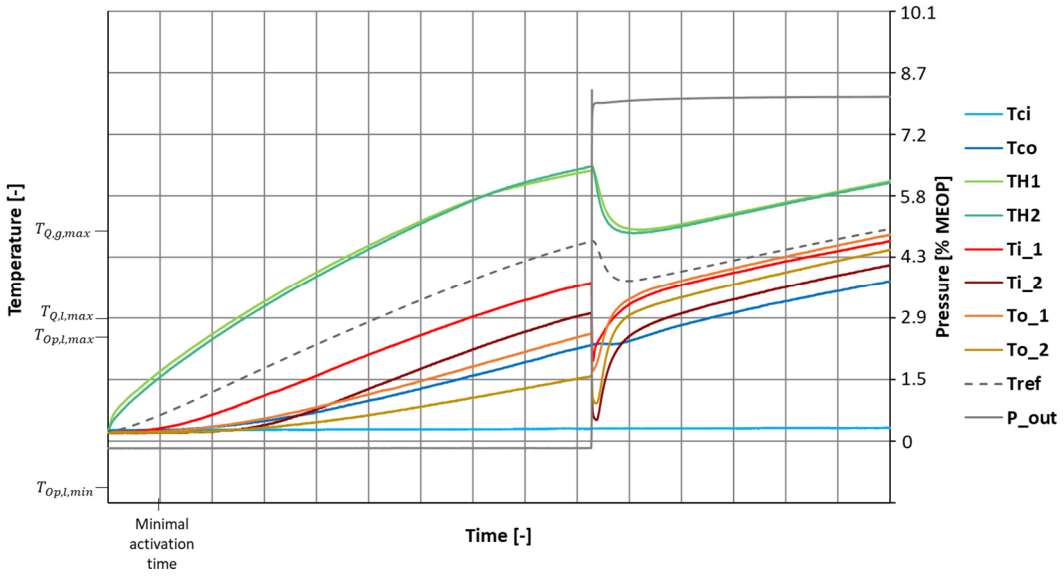

Figure 82: SMAV NC QM06 actuation test - temperatures

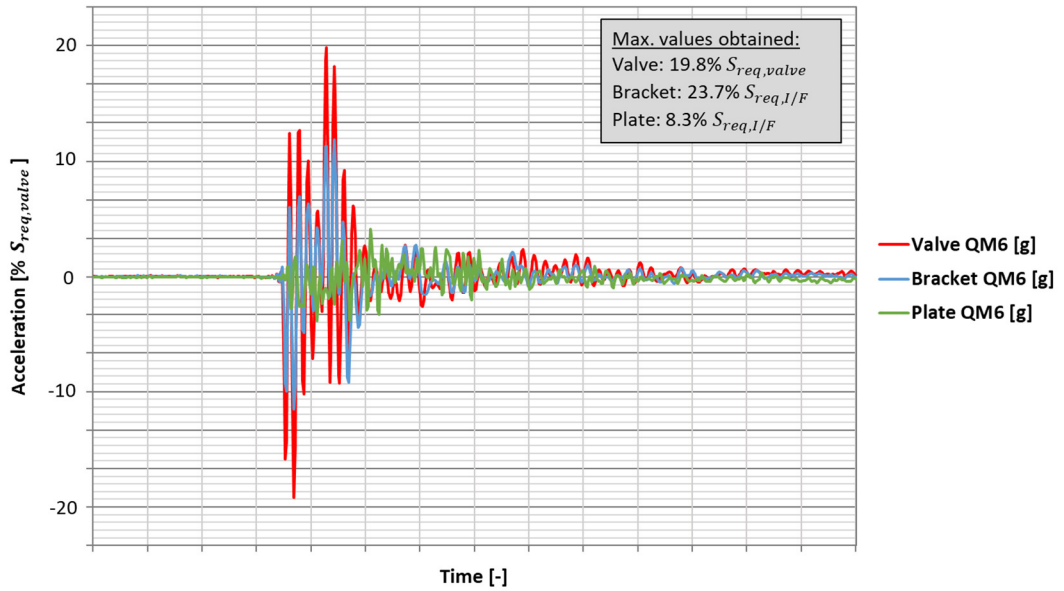

Figure 83: SMAV NC QM06 actuation test – self-induced shock

Comparison of valve actuation tests:

Similar plots as for QM06 can be obtained for QM07 and QM08. However, figure 84 presents a comparison of all three actuation tests. Therefore, the readings of T_{ref} for each test are visualized. Regarding the initial temperatures and provided heater power, the actuation times differ as expected. It can be seen that the minimal actuation time from $T_{Op,l,max}$ and the maximal actuation time from $T_{Op,l,min}$ lie well within the indicated limits. From the temperature readings, it is identifiable that the actuation temperature of QM08 yields slightly higher than of the specimens QM06 and QM07. This is assumed to be caused by the valve filled with liquid hydrazine from both ports for this test. This way, the heat dissipates into the hydrazine within the valve which results in a slower heating rate on the one hand, and a greater temperature gradient from the valve's outside surface to the valve's inner components. This causes a higher measured temperature at the valve's outside reference point until the actuator at the inside entirely reaches its transformation temperature. Another difference between QM06 and QM07 to QM08, is indicated by the sudden drop if temperature subsequently to the valve's opening. When QM06 and QM07 open, instantly a flow of liquid and cold hydrazine through the valve is enabled, which decreases the measured reference temperatures. At QM08 no flow is initialized on opening of the valve. This constitutes the reason that no cooling effect is measured in this case.

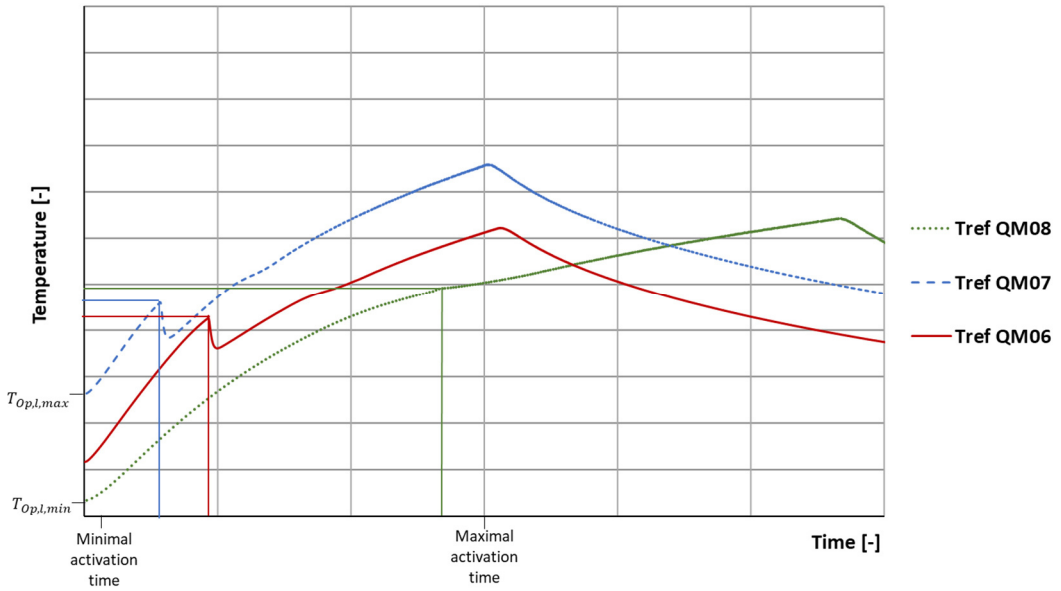

Figure 84: SMAV NC actuation tests - comparison of reference temperatures

By comparing the occurring shock loads of the three tests, a diagram can be yield, which illustrates the maximal occurring shocks for all tests. This diagram is given by figure 85 and presents the totaled peak to peak amplitudes. Considering the self-induced shock at the valve's housing itself, it can be stated, that an applied pressure gradient of around 8.5% MEOP causes a greater shock than without the presence of this pressure gradient – the difference yields more than 15% $S_{req,valve}$. Generally, the maximal shock occurs at QM07 and yields 38% $S_{req,valve}$. The maximal shock occurring without a pressure gradient results to 23% $S_{req,valve}$ for QM08. Further it can be seen, that the shock propagation towards the valve's brackets and its mounting plate is largely damped. The shock at the mounting plate for QM07 and QM08 is almost negligible.

QM8 (PA):

As outlined within chapter 6.1, the continuous heating of a hydrazine conveying feed line provides an inherent risk due to thermal decomposition. To sustain the found results, subsequently to the actuation of QM08, the post actuation heating (PA) of this specimen is conducted. From figure 86, it can be seen, that the heater is powered for more than one hour. The valve's reference temperature hereby reaches a value of $2.5 \cdot T_{Q,l,max}$. During the test the measured outlet pressure also increases slightly. As the boiling temperature at a pressure of around 8.5% MEOP has not been reached according to figure 79, this pressure increase is most likely caused by two other reasons. As also indicated by the figure, the liquid hydrazine's density decreases with an increasing temperature. Additionally, portions of the liquid hydrazine probably have decomposed due to the elevated feedline temperature. Although this slight pressure increase is determined, no hazardous thermal run away is observed. Considering long term heating at this temperature however, this might result in a notable pressure increase due to thermal decomposition of around 2% MEOP within 24 hours [49].

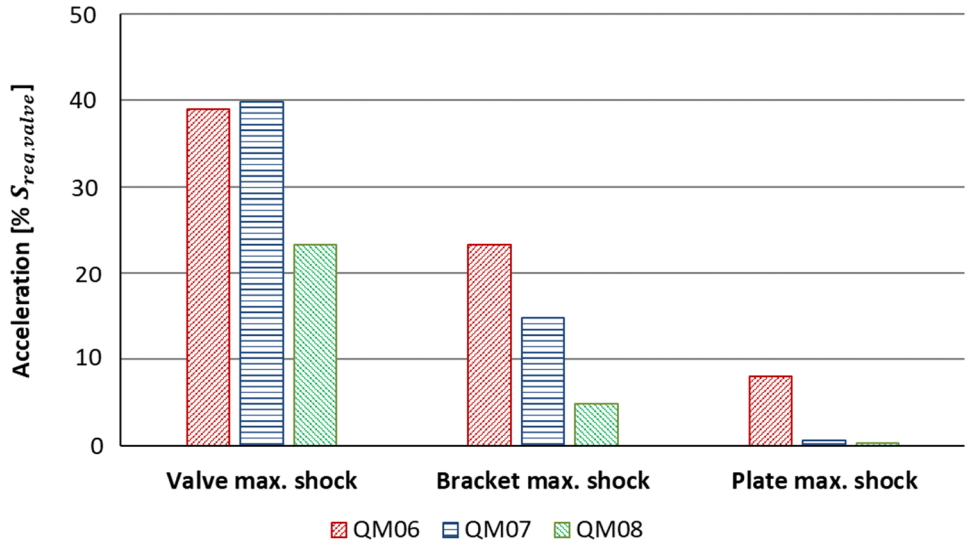

Figure 85: SMAV NC actuation tests - comparison of maximal occurring self-induced shocks

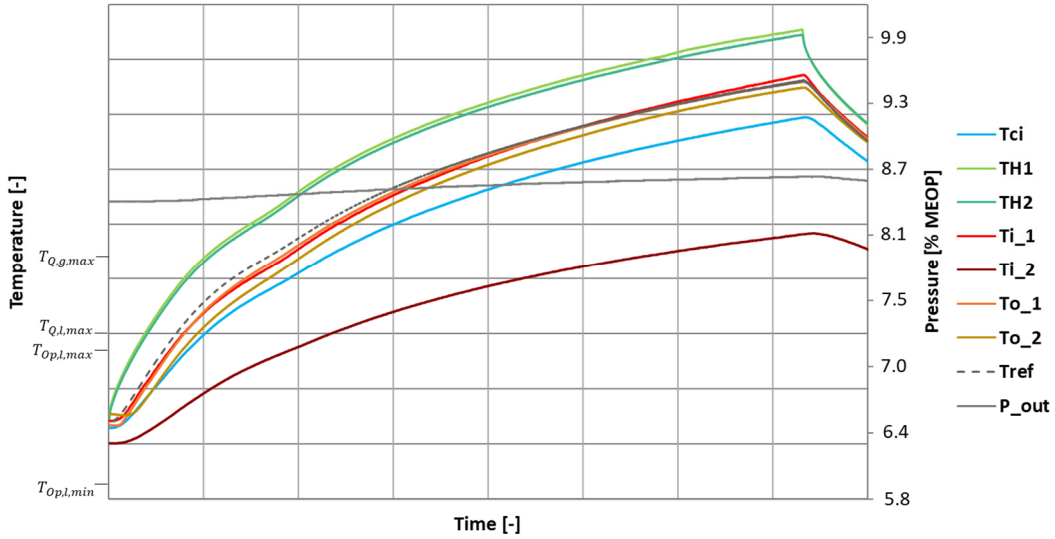

Figure 86: SMAV NC QM08 post actuation test - temperatures

6.2.3 Evaluation

Correlating the results from the conducted NC SMAV actuation tests with the found results from the literature research on hydrazine compatibility, some important conclusions can be drawn. First, it can be postulated, that the actuation of the SMAV at pressures above 20 bar does not induce a boiling process of liquid hydrazine. However, the actuation temperature does slightly exceed the recommended threshold value of a maximal feed line temperature during periods of high pressure oscillations. Nevertheless, no adiabatic compression was detected. This is due to two reasons. Firstly, the occurring shocks are too light to initiate such an explosive event. Secondly, the ratio of gas bubbles within the liquid hydrazine does not nearly reach the detonable region above 20% in volume [6]. Due to a heating period of less than 30 min and a transformation temperature of less than 100°C, no significant decomposition during actuation occurs which might decline a thruster's performance momentarily. Even during long term heating, no thermal runaway could have been detected. However, with an increasing feed line temperature and heating period likewise, the proportion of decomposed products also increases. Hence, for such cases as e.g., due to a faulty heater, a performance influence needs to be considered, yet a hazardous explosive event can be excluded.

6.2.4 Conclusion on the NO SMAV's hydrazine compatibility

The statements made above hold true for the NC SMAV. Whether the found results on the NC valve's compatibility to a hydrazine environment holds true for the NO SMAV as well, requires a closer analysis. First of all, it can be stated, that all materials adopted from the NC valve are already qualified as compatible within a hydrazine environment. Hence only the coating of the NO valve's seat and the spring's material need to be investigated experimentally in greater detail, though a literature research indicates its compatibility as well [11]. As the NO valve provides a great geometric similarity to its counterpart, a similar heat distribution throughout the valve is expected. This especially applies for the transformation temperature of the NiTiNol actuator. Hence, no boiling is expected on actuation of the NO SMAV. Also, the thermal decomposition rate on actuation lies within the same negligible range as for the NC valve. The similarity further applies for the potential risk of a permanently working heater and the resulting enhanced decomposition rate as well. Hence, the risk of a thermal runaway caused by the NO SMAV is assessed as not likely. Besides these similarities, there exist two major differences between the valves. The nominal application case of the NO valve constitutes a valve which is filled with propellants prior to actuation. Hence, this case can be compared to the test of specimen number QM08 of the NC valves. Due to a different heat distribution, this test demonstrated a slightly higher actuation temperature at T_{ref} compared to QM06 and QM07 and furthermore no significant cooling effect by running liquid hydrazine. The second major difference between the valves is given by the preloaded spring inside the NO valve. As discussed earlier within this thesis, this spring generates a mechanical shock additional to the shock on the actuator's phase transformation and subsequent notch rupture. However, the NO valve does not enable any pressure gradient between its inlet and outlet port prior to actuation. Hence and once again, this case can be compared to the test of QM08. The highest occurring shock of QM08 was measured to be around 23% $S_{req,valve}$ at the valve itself. Accordingly, the total shock caused by the actuation of the NO SMAV can be calculated by adding this value to the shock caused by spring snapping. Thus, the overall expectable shock of the SMAV NO within a hydrazine environment yields 47% $S_{req,valve}$. As this value lies within the region of the detected shocks of QM06 and QM07, no adiabatic compression event is expected at the actuation of the NO SMAV.

7. Summary and conclusion

This last chapter of this thesis gives a brief overview about all previous chapters and their most important results. In addition, all separate results are connected which enables a detailed evaluation in a broader context. Based on these conclusions, an outlook on future development actions which are recommended to be taken is given.

At the beginning of this project, the requirement and specifications of the NO SMAV are fully revised and novel defined. The specified criteria are derived and adapted from the NC SMAV, as well as from the NO PV. A major requirement constitutes the similarity of the NO SMAV to its counterpart, the NC SMAV. To evaluate and quantify the acceptable leakages through the valve's internal seal in a closed state after actuation, corresponding leakage rate requirements for different applications cases are defined. These cases distinguish whether the valve conveys liquid or gaseous phase media and are functions of temperature. $\Phi_{req,Op}$ and $\Phi_{req,Q}$ are the threshold values within the operational temperature-, respectively the qualification temperature domain. The qualification temperature range for a gaseous application constitute the most critical case. The respective leakage rate requirements must be met throughout the entire specified pressure domain from 0 bar relative pressure up to MEOP. A further critical application case on system level constitutes the case of a pressurization of the valve from the direction against flow direction. This case potentially can occur during passivation and venting of a spacecraft's pressure tanks in advance of its propellant tanks. The actuated NO SMAV must provide a liquid leak tightness of less than $\Phi_{req,rev}$ within a range of 0 bar up to the maximal reverse pressure. Considering the application case of a NO valve aboard a satellite as part of the direct feed line towards the apogee motor, its pressure drop constitutes an essential performance requirement. With regards to NO PVs, a pressure drop $\Delta p_{water,req}$ per 150 g/s of water is acceptable. A further most important requirement of a valve aboard a spacecraft is its shock generation upon actuation. The requirement for the NO SMAV is defined as less than half of the shock load generated by a PV: $S_{req,valve}$.

Regarding these revised criteria, a previously proposed valve concept is investigated, optimized and elaborated on greater detail to eventually fulfill all defined requirements. Therefore, a FVM-based CFD parameter study on the valve's hydraulic resistance is implemented. 8 design variants are simulated under equal conditions with a mass flow rate of 150 g/s of water. While the initial design I. provides a pressure drop of $3.4 \cdot \Delta p_{water,req}$, the finally optimized design IV. achieves a 17.4 % lower pressure drop of $2.8 \cdot \Delta p_{water,req}$. The valve's inner hydraulic diameter as well as the seal seat's sharp inner edge are identified as the most influencing geometric features. That is why, design variant IV with an enlarged seat diameter achieves the lowest pressure drop. Further calculations demonstrate that even a straight tube of the same length as the SMAV exceeds the requirement by 78 % and provides a minimal pressure drop of $1.8 \cdot \Delta p_{water,req}$. This is caused by the greater length of a SMAV compared to a PV. Therefore, a parallel valve solution is proposed to half the mass flow rate through one valve. As the pressure drop is proportional to the mass flow rate by the power of 2, this results in a quartered pressure drop for each valve – hence in a halved pressure drop for the entire parallel valve solution to $1.5 \cdot \Delta p_{water,req}$. Afterwards, further CFD studies on the most suitable valve design IV. are implemented determining the valve's pressure drop for Helium and Xenon. The results yield $0.4 \cdot \Delta p_{GHe,req}$ for $0.6\ g/s$ GHe and $8 \cdot 10^{-6} \cdot \Delta p_{water,req}$ for $1.2 \cdot 10^{-3}\ g/s$ gaseous Xenon which lies well within the requirement.

Determining the shock loads induced by the rapidly expanding spring upon the valve's actuation an an analytic investigation is conducted. Therefore, an oscillating model is introduced modifying the oscillation frequency by considering all relevant masses such as each spring element at a different velocity, the broken notched tube and the poppet. It is determined that the small available space for a spring's installation constitutes more restrictive than the induced shock. In detail, the shock of the strongest off-the-shelf available spring made out of an aerospace qualified stainless-steel yields

24% $S_{req,valve}$. As no pre-actuation pressure gradient can occur at a NO valve, only the rupture of the notched tube needs to be considered additionally. Considering the experimental results on QM08 of the NC SMAV actuation tests (chapter 6) additional 23% $S_{req,valve}$ should be accounted for the actuator's expansion and the notched tube's rupture. Thus, the self-induced shock of the NO SMAV results to 47% $S_{req,valve}$ which lies far below the corresponding shock load requirement by a safety factor of 2.1.

To ensure the correct working point of the NC's actuator, the NO notched tube is investigated closer. Particularly, its elongation at break is determined by a FEM study. This is especially important due to geometric adaptions made to the tube's wall thickness to implement the most suitable spring. The NO notched tube's stiffness yields only 10.3 % less than the NC notched tube's stiffness. A comparison of numerical and experimental results shows the NO notched tube's elongation at break to be between 19% - 23% of the actuators expansion. As the maximal allowable elongation, already considering a safety margin of 10%, is determined to be 29% Δl_{Act} , the correct rupture of the NO notched tube is ensured.

Eventually a valve's prototype design is presented and implemented within CATIA. Based on the prepared engineering drawings which include a full tolerance and fit analysis, a cost and mass estimation is conducted. The weight of the NO SMAV's CAD prototype yields only 5% higher than the NC variant's weight. The NO valve's center of gravity only derivates marginally in X-direction compared to the NC variant. The largest cost driver is identified to be the external coating of the valve seat. Mentioning this coating, the experimental investigations presented in chapter 5 have revealed a very insufficient and non-reproducible layer quality. Droplets, scratches and layer detachments were identified. The risks of such imperfections are outlined and the future elaboration of a quality insurance process is strongly recommended.

In advance of experimental investigations on the valve's internal seal's leak tightness, a novel leak testing device is developed, designed and manufactured. The new device enables both a forward pressurization up to MEOP as well as a reverse pressurization up to MEROP. This reverse pressurization particularly includes the generation of a high vacuum inside the jig's entire upper part. During both application cases, an external force adjustment is provided by a replaceable mechanical pressure respectively vacuum feedthrough. At the previous test device, the long-term background leakage rate towards the measurement line has demonstrated critical and has potentially falsified previous measurement results. This is due to permeation processes of Helium atoms as a function of time and pressure. Therefore, two optimized sealing options are developed and investigated experimentally. One consists of two concentrical elastomeric O-rings with venting holes in between, the other one consists of customized tin- and silver-plated C-rings. Both variants enable a reduction of the long-term background leakage rate by two orders of magnitude to less than $10^{-3} \cdot \Phi_{req,Op}$. While the O-ring solution demonstrates advantageous during pressure cycling tests, the metal C- rings provide a negligible leakage rate at constant pressures by eliminating permeation processes inherently.

Based on previous experimental results, two seal concepts are optimized to improve its reliability and suitability for the NO SMAV. In total, 4 different seal variants are investigated experimentally. While these variants differ in terms of used materials and geometric conditions, all base on the concept of a soft and hard sealing partner. The results are presented on more detail within section 5.5 and evaluated in 5.5.6., but the main findings can be summarized as follows:

- Variant I.I – material I.A poppet with r' and material I.B seat with d_H – requires high sealing forces not feasible with the NO SMAV due to its decisively restricted space for a spring installation. The reduction of the poppet's diameter results in a slower exponential decrease of leakage rate over preload force instead of a linear decrease as determined at variant I and II.
- Variant II – material II.A poppet with r and material II.B coated seat with d_H – reaches leakage rates of less than $\Phi_{req,Op}$ at ambient temperature over the entire pressure domain at about half of the installable preload $F_{s,max,1}$. While providing lower leakages at a minimal temperature $T_{Q,g,min}$, the leakage increases to about $10 \cdot \Phi_{req,Op}$ at a maximal temperature $T_{Q,g,max}$.

- Variant II.I – material II.A poppet with r' and material II.B coated seat with d_H – demonstrates a similar leakage-force correlation as variant I.I. The decrease of the leakage rate follows an exponential decrease instead of linear decrease. The increase of normal forces results in a larger deformation of the II.B layer. This improves the sealing capability ($< 10^{-3} \cdot \Phi_{req,Op}$) but also requires a higher axial force to enable a settlement and tight fit of the poppet into the seat.
- Variant II.II – material II.A poppet with r and material II.B coated seat with d_H' – achieves the best leakage rates throughout all application cases. All requirements at ambient and extremal temperatures as well as during a reverse pressurization are met eventually. However, this variant demonstrates the same settlement behavior as variant II.I. Once the poppet is fitted into the seat, it is shown that even a lower force between $0.5 \cdot F_{s,max,1}$ is enough to reach the requirements. Worth mentioning, variant II.II provides the optimized geometry regarding the hydraulic resistance and hence would reduce the valve's pressure drop by 17.4 % compared to variant II.

Variant II.II is identified as the most promising seal variant for the implementation into the NO SMAV. However, its good performance is attached to the prerequisite of a full settlement of the poppet into the seal seat. This constitutes a harsh restriction of its applicability and further development actions should investigate how this prerequisite of can be ensured. One potential solution could be the valve's actuation and the dynamic poppet impact itself. It needs to be determined, whether this impact supports the settlement behavior of the poppet. Another way to realize the settlement is to reinforce the available preload. Due to cost and qualification aspects, within the context of this project only standardized springs out of aerospace qualified materials have been investigated. Within 4.2.3 it is shown that a non-standardized spring out of material B can reach a sealing force of $1.38 \cdot F_{s,max,1}$. Particularly, this force would result in a spring induced shock of 43% $S_{req,valve}$ and hence would neither exceed the shock load requirement. Another way worth considering is the implementation of a spring with no circular wire cross-section but with a non-standard rectangular cross section. As the polar section modulus of a rectangular cross section yields higher than a circular modulus (ref. equation (4.26)) and follows $W_{polar,rect} = 0.208 \cdot d_w^3$ [51], theoretically a preload increased by 6% can be installed under the same geometric conditions. A further increase of this sealing force can be achieved by selecting a different material with higher allowable shear stresses and/or by an additional heat treatment of the spring.

If the feasibility of variant II.II remains difficult after considering the proposals outlined, variant II still represents a suitable solution for NO SMAV. With slightly higher leakage rates - but always within requirements - and an increased pressure drop, this variant does not exhibit the difficult settlement issues noted for variant II.II. Whether Variant II meets the reverse leakage rate requirement should be investigated in upcoming studies.

The tests carried out have shown the importance to ensure the exact same spatial alignment during pre-coining and a subsequent assembly of poppet and seat. Considering the assembly of a notched tube and a rear housing into a valve, an anti-twist mechanism on both components is highly recommended. To minimize friction and the risk of wedging during closing between the notched tube and the housing, the option of a small groove on the non-moving part of the notched tube - the part in front of the notch – is evaluated to be most suitable.

At the end of this work, the risks of operating a heated NO SMAV conveying liquid and/or gaseous hydrazine are investigated. By an extensive literature research, potential threats such as a thermal runaway due to decomposition or deflagration and detonation of hydrazine vapor due to adiabatic compression are examined closer. All identified phenomena are evaluated as not likely to occur during operation of the NO SMAV. These conclusions are validated by actuation tests of the NC SMAV in hydrazine. These tests quantify the shock loads, pressures and temperatures occurring during the actuation process and in the event of a heater malfunction. All measured parameters are well outside the identified hazardous regions for a valve operation with hydrazine. Thus, any kind of events endangering the system integrity can be excluded and the NO SMAV's compatibility with hydrazine is verified.

X. Bibliography

[1] Ariane Group GmbH: *Space-Propulsion* [online]. Available: http://www.space-propulsion.com [Cited 7th of August, 2020].

[2] Murray, J., Mignon, A., Promper, C., Stalmans, R. and Lafranconi, R.: *A Shape Memory Alloy actuated Satellite Isolation Valve*. 4th Int. Spacecraft Propulsion Conference, Cagliari, Sardinia, Italy, 2004.

[3] Wolf, M., Maier, T., Wacker, U., Schulte, G.: *Status of a Pyrovalve Manufacturing at EADS ASTRIUM and Assessment of Design Evolutions for Future Spacecraft Needs*. Space Propulsion Conference 2012, Bordeaux, France.

[4] The European Space Agency: *Clean Space Initiative* [online]. Available: https://www.esa.int/Safety_Security/Clean_Space/cleansat [Cited 25th of September, 2020].

[5] Kraus, S., Maier, T., Häcker F., Bühner, M. and Wolf, M.: *Development of orbital propulsion system valves with advanced actuators*. Space Propulsion 2014, Cologne, Germany, 2014.

[6] Fernando, P., Gale, D., Goody, N., Kraus, S.: *Airbus DS NO Pyrotechnic Valves Operation in Hydrazine Environment Risk Study.*

[7] Brilles, O.,Hagemann, D., Benz, F., Farkas, T.: *Explosive Decomposition of Hydrazine due to Rapid Gas Compression*. NASA, 1985.

[8] Ma, J., Karaman, I., Noebe, R. D.: *High temperature shape memory alloys*. International Materials Reviews, vol. 55 no. 5, pp. 257-315, 2010. DOI: 10.1179/095066010X12646898728363.

[9] Lux, N.: *Development of a Normally Open, Single Use Shape Memory Alloy Spacecraft Valve*. FH Aachen, 2019.

[10] Radermacher, N.: *Development of a zero-leakage valve seat for a single-activation space craft valve*. Technische Universität Dresden, 2020.

[11] Wollner, J.: *Investigations for the Development of a Single-Use Shape Memory Alloy Spacecraft Valve*. FH Wiener Neustadt, 2015.

[12] May, K. D.: *Advanced valve technology*. NASA & Midwest Research Institute, Kansas City, Missouri, USA, 1965. DOI: 19680000934.

[13] Bal-Tec™: *Ball Check Valves* [online]. Available: https://www.precisionballs.com/ball_valve.php [Cited 23rd of September, 2020].

[14] Kraus, S.: *SMA-ASLLAM-SPE-005 – SMA NO Valve component specification*. Ariane Group GmbH, Hardthausen a.K., 2020.

[15] ECSS European Cooperation for Space Standardization: *Space Engineering - Compatibility testing for liquid propulsion components, subsystems and systems*. Clause: 3.2.3. ESA Requirements and Standards Division, Noordwijk, Netherlands, 2009. DOI: ECSS-E-ST-35-10C.

[16] Gulgonul, S., Sözbir, S.: *Propellant Budget Calculation of Geostationary Satellites*. 6th International Symposium on Innovative Technologies in Engineering and Science, Antalya, Turkey, 2018.

[17] Chemie Lexikon: *Wasser Stoffdaten* [online]. Available: https://www.chemie.de/lexikon/Wasser_%28Stoffdaten%29.html [Cited 8th of September, 2020].

[18] Schmidt, E.: *Hydrazine and its derivatives – Preparation, Properties, Applications.* Published by John Wiley & Sons, Washington, USA, 1983.

[19] ECSS European Cooperation for Space Standardization: *Space Engineering – Testing*. Clause: 5.2. ESA Requirements and Standards Division, Noordwjik, Netherlands, 2012. DOI: ECSS-E-ST-10-03C.

[20] Weigand, B., Munz, C.-D.: *Analytische und numerische Methoden in der Luft- und Raumfahrt*. Lecture notes, University of Stuttgart, 2017.

[21] Munz, C. D., Müller, C., Dürrwächter, J., Schwarz A.: *CFD Programmierseminar – Programmierung eines 2D unstrukturierten Finite-Volumen Verfahrens.* Lecture notes, University of Stuttgart, 2019.

[22] Dassault Systems: *Numerical Basis of CAD-Embedded CFD – Solid Works*. NAFEMS World Congress 2013.

[23] Schichtling. H., Gersten, K.: *Grenzschichttheorie – 10te Auflage*. Published by Springer-Verlag Berlin Heidelberg, 2006. ISBN: 978-3-540-23004-5.

[24] Wiegleb, G.: *Gasmesstechnik in Theorie und Praxis – Messgeräte, Sensoren, Anwendungen*. Published by Springer Fachmedien, Wiesbaden, 2016. DOI: 10.1007/978-3-658-10687-4.

[25] Gross, D., Hauger, W., Schröder, J., Wall, W.: *Technische Mechanik 3: Kinetik – 12. Auflage.* Published by Springer Vieweg, Berlin Heidelberg. DOI: 10.1007/978-3-642-29529-4.

[26] Samm, D.: *Bestimmung von Federkonstanten.* FH Aachen, 2014.

[27] Schweizer Federntechnik GmbH: *Druckfedern EN 10270-3 1.4310* [online]. Available: https://www.schweizer-federshop.de/bsf01gri.aspx [Cited 16th of October, 2020].

[28] Federtechnik Knörzer GmbH: *Druckfedern aus Edel- und Federstahl* [online]. Available: https://www.knoerzer.eu/druckfedern.html [Cited: 16th of October 2020].

[29] Febrotech GmbH: *Schraubendruckfedern* [online]. Available: https://www.febrotec.de/de/schraubendruckfedern/ [Cited 16th of October, 2020].

[30] Kurowski, P. M.: *Engineering Analysis with SolidWorks Simulation 2013*. Published by Schroff Development Corporation, 2013. ISBN: 978-1-58503-784-1.

[31] Gomeringer, R., Heinzler, M., Kilgus, R., Menges, V., Oesterle, S., Rapp, T., Scholer, C., Stenzel, A., Stephan, A., Wieneke, F.: *Tabellenbuch Metall*. Published by Verlag Europa-Lehrmittel, Haan-Gruiten, 2017.

[32] TE Connectivity Ltd: *XFTC300 Miniature Load Cell – Data Sheet*. 2018.

[33] Kraus, S., Radermacher, N.: *Normally open SMA Valve Seat Seal Leakage Test Plan*. Ariane Group GmbH, Hardthausen a. K., 2020.

[34] Ho, E., Nau, B. S.: *Gas Emission by Permeation through Elastomeric Seals*. Tribology Transactions, vol. 39 no. 1, pp. 180-186, 1996. DOI: 10.1080/10402009608983518.

[35] Trelleborg Sealing Solutions Germany GmbH: *Turcon Variseal - PDF Catalog.* 2014

[36] Meschede, D.: *Gerthsen Physik – 25. Auflage.* Published by Springer Spektrum, Bonn, 2015. DOI: 10.1007/978-3-662-45977-5.

[37] ISO copyright office: *Vacuum technology – Dimensions of knife-edge flanges*. 3rd edition, Switzerland, 2020. DOI: ISO 3669:2020(E).

[38] Pfeiffer Vacuum GmbH: *ULD 135S, Lineardurchführung, Handbetrieb, DN 40 CF-R – Datasheet.* 2020.

[39] TC Mess- & Regeltechnik GmbH: *Hochdruck-/ Vakuum Prozessverschraubung – WF-Serie* [online]. Available: https://www.tcgmbh.de/verschraubungen/WF_serie.html [Cited 12th of September, 2020].

[40] High Tech Metal Seals GmbH: *Resilient Metal Seals – Product Guide.* Belgium, 2019.

[41] Grote, K. H., Antonsson, E. K.: *Springer Handbook of Mechanical Engineering*. Published by Springer-Verlag Berlin Heidelberg, 2009. ISBN: 978-3-540-49131-6.

[42] Sturm, A.: *Konstruktion und Charakterisierung eines piezokeramisch angetriebenen Hartsitzventils zur Anwendung bei elektrischen Gasdruckreglern für Raumfahrtanwendungen*. University of Stuttgart, 2012.

[43] Sensors ONE Ltd: *Highly Precise (0.01%) Pressure Transmittance – Data Sheet*. England, 2009.

[44] Leybold Inficon: *UL 200 Helium Leak Detector – Technical Handbook*. Cologne.

[45] Burster Präzisionsmesstechnik GmbH & Co KG: *Verstärkermodul Typ 9243 – Data Sheet*. Gemsbach.

[46] DataQ Instruments Inc: *DI-1120 Low-cost USB Data Acquisition (DAQ) System – Data Sheet*. Ohio, 2017.

[47] Sturzenegger, C.: *Studie zur Synthese von Hydrazin*. ETH Zurich, 1958.

[48] Dadieu. A., Damm, R., Schmidt, E. W.: *Raketentreibstoffe mit 247 Tabellen*. Published by Springer, Wien, 1968. ISBN: 978-3-211-80856-6.

[49] Benard, I. J., Streit, A. F.: *High temperature operation of hydrazine feed systems*. AIAA 21st joint propulsion conference, California, 1985.

[50] Reitan, T., Durbin, M.: *Extreme temperature operation of a hydrazine rocket engine*. American Institute of Aeronautics and Astronautics Inc., 1997.

[51] Wittel, H., Jannasch, D., Voßiek, J., Spura, C.: *Roloff/Matek Maschinenelemente – Normung, Berechnung, Gestaltung – 24. Auflage.* Published by Springer-Verlag GmbH Deutschland, 2019. DOI 10.1007/978-3-658-26280-8

XI. Appendix

XI.I. Exemplary engineering drawings of test jig components

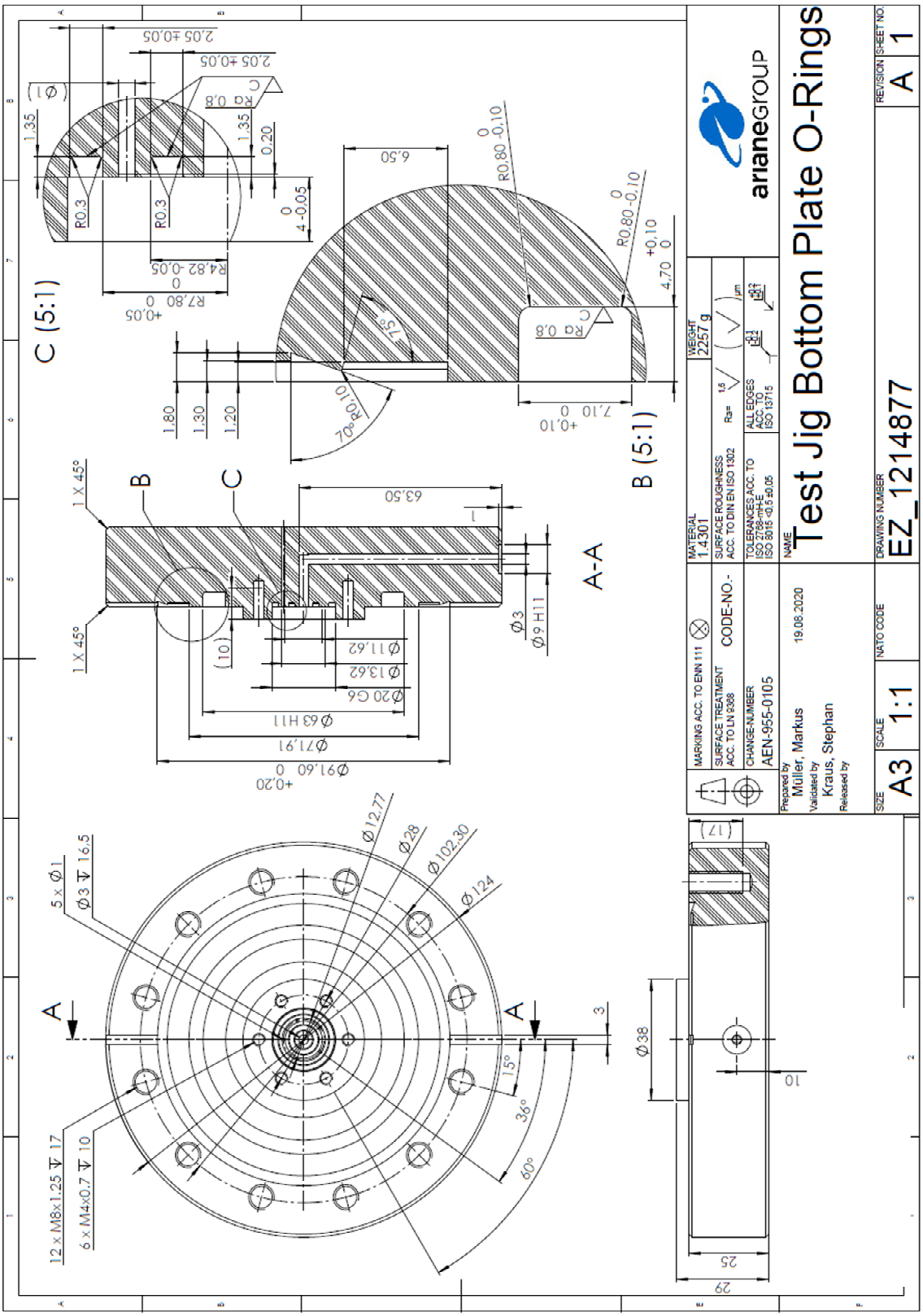

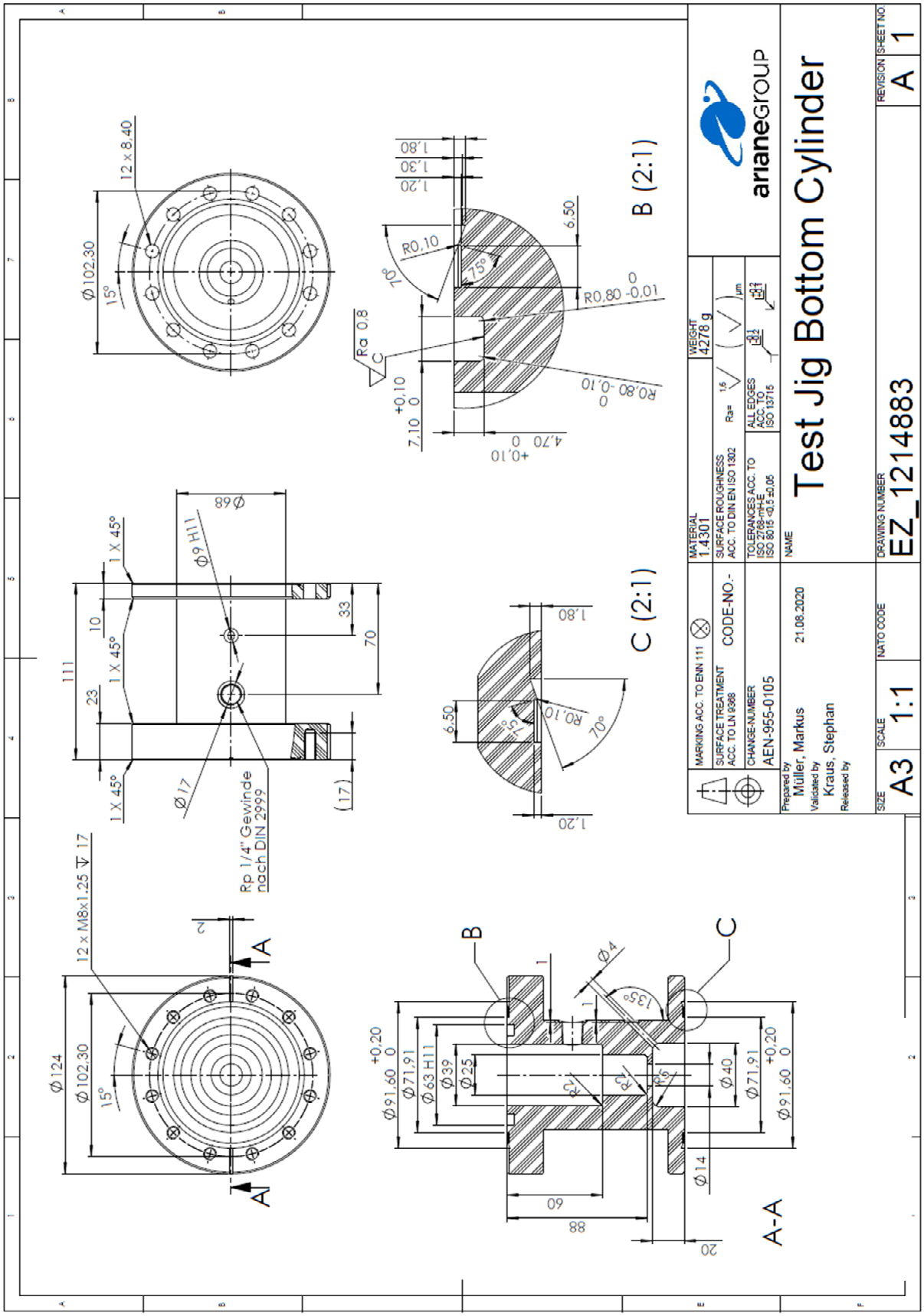
Test Jig Bottom Cylinder
arianeGROUP
EZ_1214883
A3
1:1
A
1
MATERIAL
1.4301
WEIGHT
4278 g
SURFACE ROUGHNESS
ACC. TO DIN EN ISO 1302
TOLERANCES ACC. TO
ISO 2768-mH-E
ISO 8015 <0.5 ±0.06
ALL EDGES
ACC. TO
ISO 13715
MARKING ACC. TO ENN 111
SURFACE TREATMENT
ACC. TO LN 9368
CODE-NO.-
CHANGE-NUMBER
AEN-955-0105
NAME
Prepared by
Müller, Markus
21.08.2020
Validated by
Kraus, Stephan
Released by
SIZE
SCALE
NATO CODE
DRAWING NUMBER
REVISION
SHEET NO
B (2:1)
C (2:1)
A-A
12 x 8,40
Ø102,30
15°
12 x M8x1,25 ↧ 17
Ø124
Ø102,30
15°
Ø68
Ø9 H11
1 X 45°
1 X 45°
1 X 45°
111
10
23
33
70
Ø17
(17)
Rp 1/4" Gewinde
nach DIN 2999
R0,10
10°
75°
6,50
R0,80 -0,01
0
Ra 0,8
7,10 +0,10 0
4,70 +0,10 0
R0,80 -0,10 0
1,80
1,30
1,20
6,50
R0,10
75°
70°
1,80
1,20
Ø4
135°
Ø91,60 +0,20 0
Ø71,91
Ø63 H11
Ø39
Ø25
R2
R3
R5
Ø40
Ø71,91
Ø91,60 +0,20 0
Ø14
60
88
20